Delft University of Technology
Faculty of Electrical Engineering, Mathematics and Computer Science
Delft Institute of Applied Mathematics

Particle nucleation and coarsening in aluminum alloys

A literature study submitted to the
Delft Institute of Applied Mathematics
in partial fulfillment of the requirements

for the degree

MASTER OF SCIENCE
in
APPLIED MATHEMATICS

by

D. den Ouden

Delft, the Netherlands
May 2009

TU Delft

MSc LITERATURE STUDY APPLIED MATHEMATICS

"Particle nucleation and coarsening in aluminum alloys"

D. den Ouden

Delft University of Technology

Daily supervisor	**Responsible professor**
Dr.ir. F.J. Vermolen	Prof.dr.ir. C. Vuik

May 2009 Delft, the Netherlands

Preface

This document is the result of the literature study of my Master of Science research project at the University of Technology at Delft, The Netherlands. This project has been carried out at the faculty of Electrical Engineering, Mathematics and Computer Science at the chair of Numerical Analysis.

I wish to thank Fred Vermolen for proposing and supervising this project.

Contents

List of Figures

List of Tables

Chapter 1

Introduction

Heat treatment and manufacturing of aluminum alloys is a complex operation that has several factors that influence the usability of the object after metalworking. The influence of most of these factors have been studied and achieved by a process of trial and error. Examples of such factors are the temperature, deformations and radiation. Although the experimentally achieved results are useful, they are only performed on a particular ally or in a particular setting, which as a results implies that the results can be false for other alloys and settings. To resolve this problem a mathematical model for the influence of these factors could be proposed. Until recently only statistical models have been proposed, tested and verified, but these models only investigate the influences of the temperature on the alloy. Therefore a model based on possible exact solutions of a problem can me more useful and and possibly can be combined with other models, such as the those for the deformation within an alloy due to exterior or interior forces. It seems likely that these models will consist of several partial differential equations, which can be solved exact or with numerical methods.

This document will focus on the factor regarding nucleation and growth of particles in aluminum alloys during rolling or extrusion, since the presence and size of particles can influences the characteristics of the aluminum alloy object. Nucleation and growth of the particles will be modeled by following the same reasoning as Myhr and Grong [7]. Metalworking of an object will be done by means of stress-strain relations which will result in (in)elastic deformation models.

In this paper we show that the model proposed by Myhr and Grong [7] is correct, but also can be improved by use of other time integration methods. We will also derive a elastic deformation model, for which will be shown that numerically obtained results are congruent with physics.

The remainder of this document is structured as follows. First an introduction to the field of metallurgy is given. Chapter 3 will derive and state the models for particle nucleation and growth and for elastic deformations. The next chapter will reproduce part of the results from [7], compare different time integration methods and discuss results from numerical simulation of the elastic deformation model. Finally some conclusions will be drawn and follow-up work will be stated.

Chapter 2

Preliminaries in metallurgy

This chapter deals with the basic metallurgy concepts that are required to understand the behavior of alloys during equilibrium and when changing to equilibrium. We begin with a short introduction about the ordering of alloys. Then a discussion is presented about the thermodynamical behavior of alloys and the related phase diagrams. Next the diffusional concepts related to alloys are stated. Thereafter transformations due to diffusion are discussed. Finally some information is presented about metalworking techniques. The information presented in this chapter mostly originates from [9], especially Chapters 1, 2 and 5.

2.1 Metal alloys

Although the term alloy or metal alloy is unambiguous, one can still order these alloys by their properties. Such an ordering can be made on the solvent metal, but also on the number of components of the alloy. If using the solvent metal for ordering one can distinct the following twenty groups:

Aluminum	Gold	Mercury	Tin
Bismuth	Indium	Nickel	Uranium
Cobalt	Iron	Potassium	Zinc
Copper	Lead	Silver	Zirconium
Gallium	Magnesium	Titanium	Rare earth metals

Another common ordering uses the number of components in the alloy. Although any alloy unintentionally contains all the elements from the periodic table, only traces of most elements are found. If we neglect those elements of which only traces are present, we can number the components of the alloy by decreasing weight percentage or another factor. If only one alloy element is present besides the solvent metal, we speak of binary alloys. Likewise a ternary alloy consist of two alloy elements besides the solvent metal. Quaternary alloys consist of three alloy elements and the solvent metal. Alloys with more then three alloy elements do not have a specific name, which is why we call it complex alloys.

Besides the ordering on the number of components of an alloy there exist a subordering for the ternary, quaternary and more complex alloys. This ordering is based on the interaction of the alloy elements with each other. Assume we have a ternary alloy with alloy elements that have the intension to bond with each other. As a result we can view this alloy as a binary alloy, since each nuclei that will form, consists of one element, namely the combination of the two original elements. A ternary alloy with this property will be called a quasi-binary alloy. Likewise a distinction can be made in quaternary and complexer alloys.

Using the last ordering by number of components and the subordering by behavior of the alloy elements the overview in Table 2.1 is gained.

Binary	Ternary	Quaternary	Complex
	Quasi-Binary	Quasi-Binary	Quasi-Binary
		Quasi-Ternary	Quasi-Ternary
			Quasi-Quaternary

Table 2.1: Ordering of alloys by behavior of alloy elements.

2.2 Thermodynamics and Phase diagrams

Before starting with the discussion about thermodynamics and phase diagrams, the definition of three terms need to be given, so that the meaning of these words are clear. These terms are *system*, *phase* and *component* with definitions as below. As a result of these definitions, we can describe the composition of a system or phase by giving the (relative) amounts of the components.

Definition. *A **system** is an alloy that can exist as a mixture of one or more phases.*

Definition. *A **phase** is a portion of a system with homogeneous properties and a homogeneous composition, which is physically distinct from other phases, e.g. parts of the system.*

Definition. *A **component** is one of the elements or chemical compounds that make up the system.*

The transformations of the phases of a system into other phases can be described by the use of thermodynamics. A phase will transform into another phase or several other phases, depending on the stability of the phase. Eventually the system will be in it's most stable state. Stability in thermodynamics is described by the Gibbs free energy G, measured in joules (J), of the system, defined by

$$G = H - TS,$$

where H is the enthalpy in Joules, T the temperature in Kelvin (K) and S the entropy of the system in Joules per Kelvin (J/K).The enthalpy H measures the heat content of the system and is given by

$$H = E + PV,$$

where E is the internal energy in Joules, P the pressure in Joules per cubic Meter (J/m^3) and V the volume in cubic Meters (m^3) of the system.

If the temperature and pressure are assumed to be constant, a system will eventually transform to the most stable state characterized by the lowest Gibbs free energy. Potential candidates for this stable state are determined by calculating the conditions such that

$$dG = 0.$$

From these candidates we denote the state with lowest Gibbs free energy as the stable equilibrium state, and the other candidates will be denoted by metastable states. If a system is in a metastable state, it will, given time, transform to the stable equilibrium state.

The above defined Gibbs free energy can be used to derive phase diagrams for alloys. This derivation will not be given, but can be found in [9]. An example of a phase diagram for a binary alloy can be found in Figure 2.1. Here α, β and L are the possible phases the system can be in. The phase diagram has as

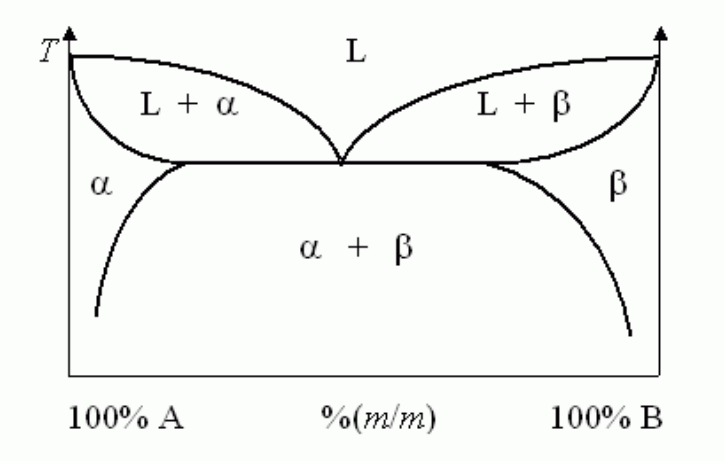

Figure 2.1: An example of a phase diagram. Image from [12].

horizontal axis the composition of the system, measured in the amount or concentration of one of the components. The vertical axis gives the temperature. Inside the diagram lines are drawn that separate the phases that the alloy can be in or can consist of.

Although the Gibbs free energy and phase diagrams can be used to derive information about a system that is in its stable equilibrium state, the probability that one has a system that is in such a state is small. Therefore the concept of diffusion in a system is needed.

2.3 Diffusion

If a system is not in a stable equilibrium state, an important process that influences the time and manner in which the equilibrium state is reached, is the diffusion of atoms in the system. There are two types of diffusion that occur in systems. The first type is interstitial diffusion, the second type substitutional diffusion. Interstitial diffusion occurs when the solute atoms are significantly smaller than the atoms of the solvent. The difference in size of the atoms allows the solute atoms to force their way between the atoms of the solvent atoms. If the solute atoms are as large or larger then the atoms of the solvent, substitutional diffusion occurs. Substitutional diffusion is characterized by a vacancy mechanism. Here a solute atom will move to a vacant place in the solvent matrix. A schematic interpretation of the two diffusion types can be found in Figure 2.2.

It is clear that interstitial diffusion can take place without influencing the ordering of the solvent atoms and thus the concentration of the solvent. This type of diffusion can therefore be modeled by Fick's second law. During substitutional diffusion it is likely that solvent atoms will also move to other locations in the matrix, thereby altering the concentration of the solvent. This means that the diffusion of solute atoms cannot be described by Fick's second law. If we assume on the other hand that we have a dilute solution, we may assume according to [9] that the solvent concentration is constant. As a result, also substitutional diffusion can be modeled by Fick's second law. Since substitutional diffusion requires the presence of vacancies, that are available in small numbers only, substitutional diffusion rates are much lower than interstitial diffusion rates in general.

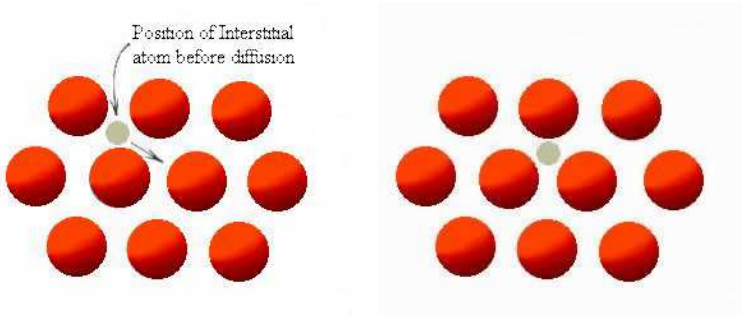

(a) Atom arrangement before interstitial diffusion.

(b) Atom arrangement after interstitial diffusion.

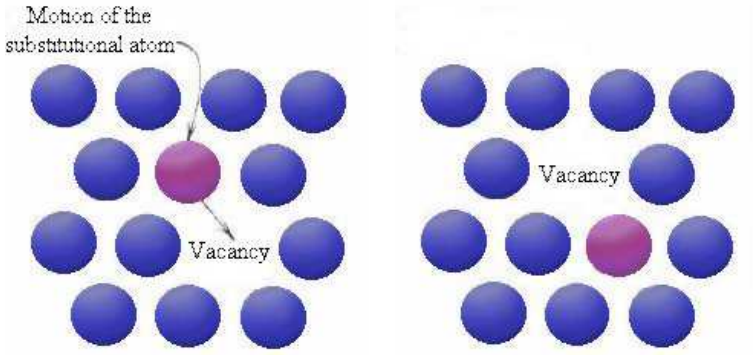

(c) Atom arrangement before substitutional diffusion.

(d) Atom arrangement after substitutional diffusion.

Figure 2.2: Interstitial and substitutional diffusion. Image from [10].

2.4 Diffusional transformations in solids

Due to diffusion, interstitial or substitutional, caused by a change in temperature the phases of a system can transform. There are five types of phase transformations possible, namely precipitation reactions, eutectoid transformations, ordering reactions, massive transformations and polymorphic changes. Precipitation reactions are those reactions that describe the transformation of a single solid phase into a mixture of two solid phases. If α is the phase before transformation and α' and β the phases after transformation, precipitation reaction can be expressed as

$$\alpha \rightarrow \alpha' + \beta.$$

If we have a system in a supersaturated metastable solid phase α and a precipitation reaction has occured, the resulting system will consist of two phases, α' and β. Here α' is a solid phase with lower Gibbs free energy than α but with the same crystal structure as α. β is a (meta)stable precipitate phase.

Eutectoid transformation describe the change of a phase consisting of two components into a mixture of two solid phases. If γ is the phase before transformation and α and β the phases after transformation, eutectoid transformation can be expressed as

$$\gamma \rightarrow \alpha + \beta.$$

In this case the mixture of phases α and β is more stable then the single phase γ. Both eutectoid transformations and precipitation reactions influence the matrix of the system. As a result these transformations can only occur if long-range diffusion is present in the system. Phase transformations that do not require long-range diffusion are the three remaining transformations.

Ordering reactions describe the transformation of a single phase α to the single phase α' and where the phase α has an disordered matrix structure and α' a ordered matrix structure. Reactions of these types can be expressed as

$$\alpha(\text{disordered}) \rightarrow \alpha'(\text{ordered}).$$

If a phase transforms into several other phases that have different crystal structures than the original phase, but with the same overall composition, a massive transformation has occurred. A simple example of this type of transformation can be described by the transformation

$$\beta \rightarrow \alpha.$$

In single component systems there can exist crystal structures that are stable in some temperature ranges. If the temperature changes in such a way that the present phase becomes unstable, a polymorphic transformation will occur. After this transformation the system will be in a stable phase with different crystal structure then the starting phase. Such a reaction can be described by

$$\gamma \rightarrow \alpha.$$

A schematic representation of the above discussed phase transformations can be found in Figure 2.3.

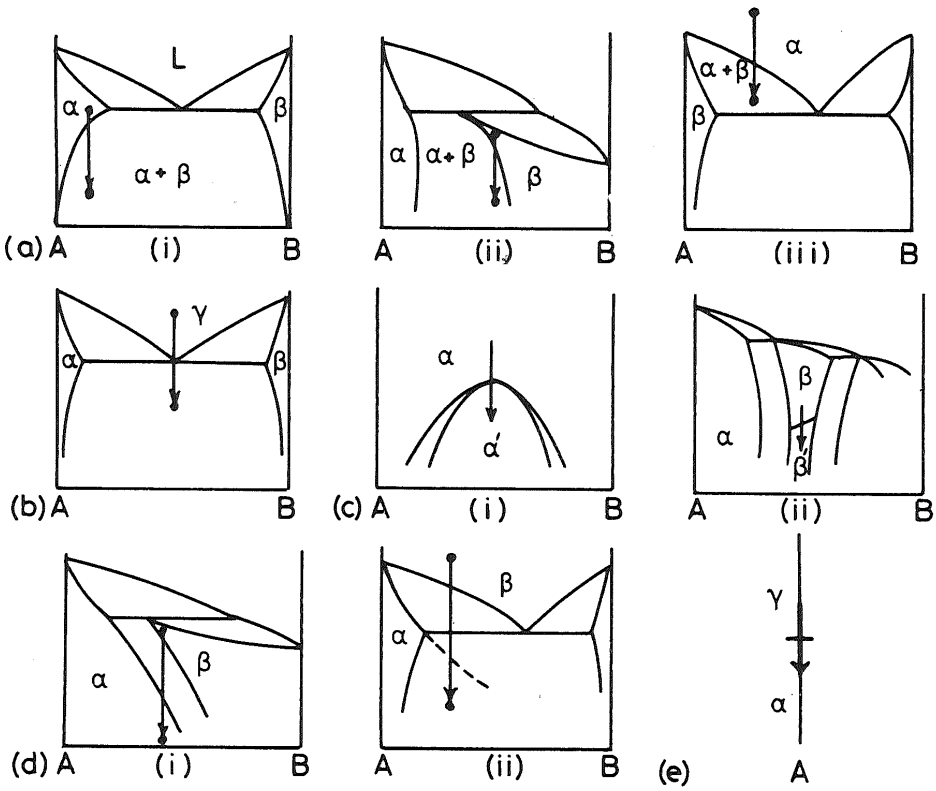

Figure 2.3: Examples of diffusional phase transformations. Image from [9].

In this thesis only phase transformations caused by precipitation reactions are modeled. These transformations are characterized by diffusional nucleation and growth. There are two types of nucleation, namely homogeneous and heterogeneous. The latter is the most occurring type and therefore will be used to model the nucleation in a system. After nuclei are formed, the nuclei will grow or shrink. This growth will also be modeled to describe the behavior of the system under time. The models for nucleation and growth will not be derived here, but can for example be found in [9].

2.5 Metalworking techniques

There exist several metalworking techniques, such as (flat) rolling, extrusion, pressing and casting. In this paper only flat rolling and extrusion will be of importance. Both of these methods involve reforming the metal object by pressure.

Flat rolling is used to lower the thickness of a metal plate as in Figure 2.4. If the temperature of the plate is below the temperature at which nucleation stops, this method is referred to as cold rolling. If the temperature is higher, we speak of hot rolling. Extrusion is a method that reforms a block of metal into another shape by pressing it through a die. An example can be found in Figure 2.5. This methods can be also be distinguished by the temperature at which the metal is reformed.

Both methods can influence the nucleation and growth of particles as it changes the location of these particles, but also the volume of the metal object and as a result the concentrations influence nucleation and growth. The reforming of the metal is an application of an (in)elastic deformation, which means that it can be modeled by stress and strain. The relation between stress and strain cannot be described by Hook's Law, as this law only is applicable to elastic deformations.

The stress-strain relation for aluminum can be described by Figure 2.6. In this figure point 2 indicates the yield strength for aluminum. If a force is applied with resulting stress above this yield strength, inelastic deformations will occur. Forces with resulting stress below the yield strength result in elastic deformations. The yield strength for aluminum lies between 15×10^9 and 2015×10^9 N/m^2.

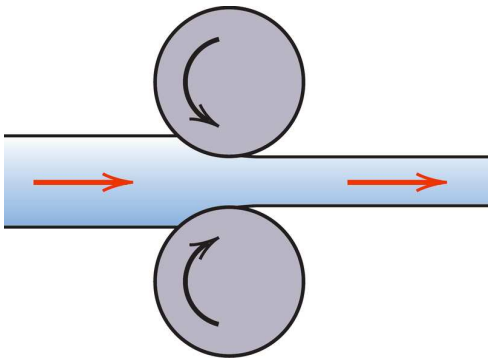

Figure 2.4: Flat rolling. Image from [13].

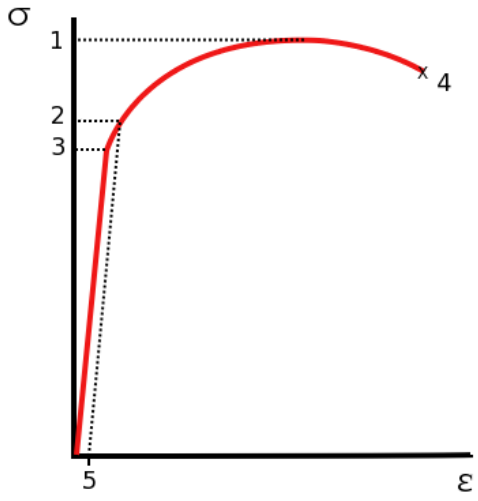

Figure 2.6: Stress-strain relation for aluminum. Image from [15].

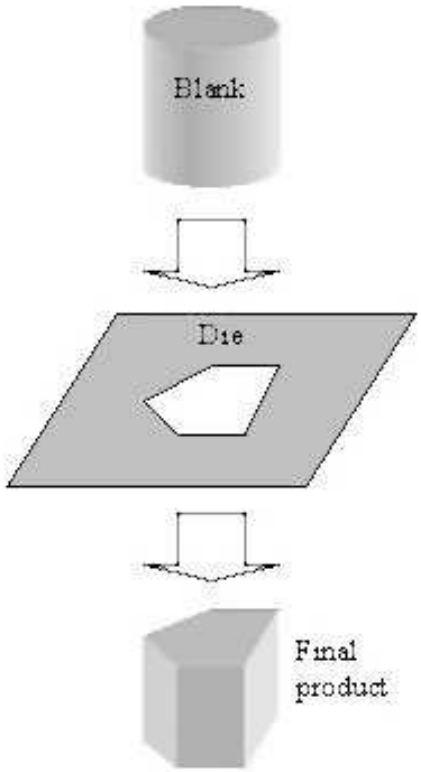

Figure 2.5: Extrusion. Image from [14].

Chapter 3

Mathematical model

This chapter will discuss the derivation and formulation of two different models. The first model concerns the precipitation and growth of particles in binary and quasi-binary alloys, the second model will model elastic deformations.

3.1 Nucleation and growth of particles

In this section the theory discussed in Sections 2.2 to 2.4 will be used to model the precipitation and growth of particles in binary and quasi-binary alloys. This model was first proposed by Kampmann et al. in [5, 11] and Langer and Schwartz in [6] and numerically solved by Myhr and Grong in [7]. The model consists of three parts, each of them related to each other. We will state these parts individually in the next sections.

3.1.1 The nucleation model

In Section 2.4 the phase transformation precipitation reaction was discussed. This transformation is characterized by nucleation and growth of particles. From [7] and [9] we can assume that the number of particles that are created, the nucleation rate, can be described by:

$$j = j_0 \exp\left(-\left(\frac{A_0}{RT}\right)^3 \left(\frac{1}{\ln(\bar{C}/C_e)}\right)^2\right) \exp\left(-\frac{Q_d}{RT}\right), \tag{3.1}$$

where j is measured in the number of particles per cubic meter per second ($\#/m^3 s$). In this formula $\bar{C}$ is the mean solute concentration in the system and C_e the equilibrium solute concentration at the particle/matrix interface, which can vary with time. The factors j_0 and A_0 are parameters that are related to the energy barrier for nucleation and scale the nucleation to the correct proportions. Further R, T and Q_d are respectively the universal gas constant (8.314 $J/K\text{mol}$), the temperature (K) and the activation energy for diffusion (J/mol). The meaning of these quantities and any other terms can be found in the nomenclature at the end of this document.

The term C_e can be calculated using the phase diagrams as discussed in Section 2.2. In this report the Arrhenius rate relation, which describes the rate at which the concentration changes with temperature, is used. This relation gives as result the formula

$$C_e = C_s \exp\left(-\frac{Q_s}{RT}\right),$$

where C_s can be derived from either the phase diagram or guessed from experimental results [9].

3.1.2 The rate law

Besides a nucleation rate that predicts the number of new particles that will be created per second, the growth of the present particles will influence the precipitation reaction. For the sake of simplicity, we assume that a particle has a spherical shape, with radius r. For this particle its radius will change in time at the rate

$$v = \frac{dr}{dt} = \frac{\bar{C} - C_i}{C_p - C_i}\frac{D}{r}, \tag{3.2}$$

where C_i is the particle/matrix interface concentration and C_p the concentration of the solute of interest inside the particle. It can be shown that C_i can be related to the equilibrium concentration C_e, which results in

$$C_i = C_e \exp\left(\frac{2\sigma V_m}{rRT}\right). \tag{3.3}$$

For each combination of possible concentrations $C_e, \bar{C}$, there is a particle that will neither grow or dissolve. From (3.2) and (3.3) we can derive that this particle has radius

$$r^* = \frac{2\sigma V_m}{RT}\left(\ln\left(\frac{\bar{C}}{C_e}\right)\right)^{-1} \tag{3.4}$$

which we will call the critical particle radius of the system. From this result we can also conclude that v is negative for radii smaller than r^* and that v is positive for radii larger than r^*. This means that the smaller particles will dissolve and the larger will grow.

The diffusion coefficient D can be calculated by means of an exponential formula depending on Q_d, R and T and is given by

$$D = D_0 \exp\left(-\frac{Q_d}{RT}\right),$$

where D_0 is derived from experimental results. For the derivation of this formula one is invited to read Chapter 2 of [9].

3.1.3 The particle size distribution

During this study, we are interested in the number of particles in a certain system as a function of time. One tool to describe this is the use of a particle concentration function. If we denote this concentration by N with the definition that $N(r,t)$ indicates the number op particles per cubic meter with particle radius between $r - \Delta r/2$ and $r + \Delta r/2$ at time t, we may derive a model for N. Δr is a numerical value, which can be interpreted as the size of a numerical control interval.

Let $\Omega = (r, r + \Delta r) \subseteq [0, \infty)$ be an arbitrary domain. Let F be the flux of transport of particles over radii from this domain. If we assume that F has positive orientation, the flow of particles into Ω is defined by $F(r)$. Similar the flow out of Ω equals $F(r + \Delta r)$. The change of particles with radii from Ω can also be due to a source term S. As a result, the change in time of the number of particles with radius from Ω can be expressed as

$$\Delta r \frac{\partial N}{\partial t} = F(r) - F(r + \Delta r) + \Delta r S.$$

Dividing by Δr and letting Δr tend to zero, we arrive with the use of the definition of the partial derivative at

$$\frac{\partial N}{\partial t} = -\frac{\partial F}{\partial r} + S.$$

By definition, the flux F is defined as the number of particles that cross a certain boundary, normalized by the area of that boundary. Since we are working in one dimension, we can say that this area equals 1. We also formally know the rate at which the particles 'move', i.e. grow, namely v. This means that the flux F is given by $F = Nv$. Substituting this relation into the derived partial differential equation, results in

$$\frac{\partial N}{\partial t} = -\frac{\partial (Nv)}{\partial r} + S. \tag{3.5}$$

In the field of metallurgy one is often not interested in the number of particles per cubic meter (N), but in the particle size distribution function ϕ. To simplify things N is calculated numerically, after which ϕ can be determined by the relation $\Delta r_i \phi(r_i, t) = N(r_i, t)$ where r_i is the center of a numerical control volume and Δr_i the size of this control interval.

3.1.4 The complete model for the particle distribution

Although we have formulated three formal expressions about the nucleation and growth of particles, we do not have a closed system yet. Closing this system requires the definition of the source term S in (3.5) and the definition of boundary and initial conditions for N.

We will start with defining the source term S. This term represents the number of particles that nucleate per second per cubic meter. In Section 3.1.1 we have formulated the function j, that has this same meaning. So a logical step is to relate S to j, but $S = j$ is not useful, since then the overall production over the real axis can become infinitely large. Research by Kampmann et al. [5] has indicated that the particles that are being formed have a radius that is slightly larger then the critical radius r^*. Let Δr^* be a small positive number and denote by $r^* + \Delta r^*$ the radius of particles that are being formed. Now we can formally say that S is given by

$$S(r,t) = \begin{cases} j(t) & \text{if } r = r^* + \Delta r^*, \\ 0 & \text{otherwise.} \end{cases} \tag{3.6}$$

Although we now have defined the source term S, yet no relation between j and N has been given. This relation can be made easily if we define the mean concentration $\bar{C}$ as a function of N. In the above section we have formally defined the function ϕ as the size distribution function, which is related to N and will be used in the needed relation.

First define the particle volume fraction f as

$$f(t) = \int_0^\infty \frac{4}{3}\pi r^3 \phi dr. \tag{3.7}$$

Note that f is dimensionless. If no particles are present, we can easily see that $f = 0$ and that $\bar{C} = C_0$, where C_0 is the concentration of the solute in the overall system. This concentration is assumed to be known for each system. If on the other hand particles are present, the weight percentage of the solute in the particles is given by $C_p f$. As a result the concentration of solute not in the particles, $\bar{C}$, can be expressed by

$$\bar{C} = \frac{C_0 - C_p f}{1 - f}. \tag{3.8}$$

Using equations (3.7) and (3.8) to obtain j and S we have related S to our function N, which was needed to close the system. A fortunate result of the derived relation, is that we also have found a relation between v and N, by means of $\bar{C}$.

On inspecting the partial differential equation (3.5), we see that at most one initial condition and at most one boundary condition is needed. The initial condition is of the form

$$N(r, 0) = N_0(r),$$

where N_0 is a known positive function or identically zero. If we investigate the characteristics of the system, we see that these can be divided into to regions, to the left of r^* and to the right of r^*. The characteristics plane with the division line r^* can be seen in Figure 3.1. The region left of r^* has a negative growth rate v, to the right a positive growth rate v. Due to these characteristics, no boundary condition need to be specified.

We now formulated a closed system that can predict the number of particles per cubic meter in an alloy. This system is given by

$$\begin{cases} \dfrac{\partial N}{\partial t} = -\dfrac{\partial (Nv)}{\partial r} + S & \text{for } r \in [0, \infty), t \in (0, \infty), \\ N(r, 0) = N_0(r) & \text{for } r \in [0, \infty). \end{cases}$$

Note that this is a non-linear partial differential equation due to the relations between N, v and S.

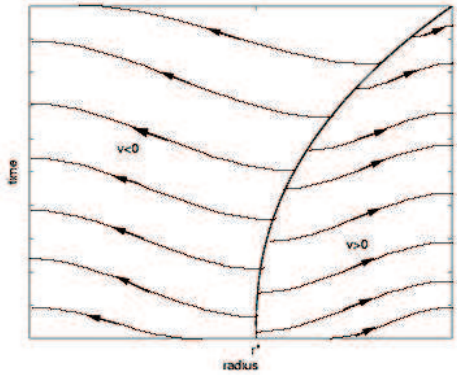

Figure 3.1: Characteristics of system (3.5).

3.1.5 Several derived quantities

Although a complete model has been formulated from which multiple quantities can be derived, other quantities are also of interest. These quantities are the total number of particles present in the system, the mean particle radius of the system and the standard deviation of the radii of the system. Both the total number of particles as the mean particle radius can be expressed as the moments of the size distribution function ϕ.

Let $n = n(t)$ be the total number of particles per cubic meter present in the system. This quantity can be calculated by the first moment of ϕ:

$$n(t) = \int_0^\infty \phi(r,t)dr.$$

Let $\bar{r} = \bar{r}(t)$ be the mean particle radius of the system. This quantity can be calculated by dividing the second moment of ϕ by the first moment of ϕ:

$$\bar{r}(t) = \frac{1}{n(t)} \int_0^\infty r\phi(r,t)dr.$$

Let $\rho(t) = \rho$ be the standard deviation of radii of the system. This quantity can be calculated by the next formula:

$$\rho(t) = \sqrt{\frac{1}{n(t)} \int_0^\infty (r - \bar{r}(t))^2 \phi(r,t)dr}.$$

3.2 Elastic deformations

In elastic deformations the terms stress and strain are of importance. Strain represents the relative displacement between points in a system under deformation. This means that we can define the strain in a system by

$$\varepsilon_{ij} = \frac{1}{2}\left(\frac{\partial u_i}{\partial x_j} + \frac{\partial u_j}{\partial x_i}\right) \qquad \text{for } i,j = 1,2,3,$$

where x_i is the i-th coordinate variable and u_i the displacement in the i-th coordinate in a domain Ω. The domain of interest Ω will not be mentioned again, but will be assumed to be the same throughout this entire section.

Stress measures the amount of force exerted per unit area on a body due to displacements. The stress within a body can be related to the strain of that body by Hooke's Law, assuming small displacements u_i and no external forces above the yield stress, given by

$$\sigma_{ij} = \lambda\delta_{ij} \sum_{k=1}^{3} \varepsilon_{kk} + 2\mu\varepsilon_{ij} \qquad \text{for } i,j = 1,2,3, \tag{3.9}$$

where δ_{ij} is the Kronecker delta, λ the bulk modulus of the system and μ the shear modulus. The latter two moduli are also known as the Lameé constants.

Both λ and μ are related to the Young's modulus E and the Possion's ratio ν by the formulas

$$\lambda = \frac{E\nu}{(1-2\nu)(\nu+1)}$$
$$\mu = \frac{E}{2(\nu+1)}.$$

Any body under elastic deformation obeys Newton's Second Law, which states that the sum of all forces acting an a body equals the mass of that body multiplied with the acceleration. If $\boldsymbol{b}$ is a vector containing all internal body forces per unit volume, the sum of the forces is given by

$$\nabla \cdot \boldsymbol{\sigma} + \boldsymbol{b},$$

per unit volume, with

$$\boldsymbol{\sigma} = \begin{bmatrix} \sigma_{11} & \sigma_{12} & \sigma_{13} \\ \sigma_{21} & \sigma_{22} & \sigma_{23} \\ \sigma_{31} & \sigma_{32} & \sigma_{33} \end{bmatrix}.$$

The acceleration within the system is defined as

$$\frac{\partial^2 \boldsymbol{u}}{\partial t^2}$$

where $\boldsymbol{u} = (u_1, u_2, u_3)^T$. As a result the force balance yields per unit volume

$$\rho_m \frac{\partial^2 \boldsymbol{u}}{\partial t^2} = \nabla \cdot \boldsymbol{\sigma} + \boldsymbol{b}, \tag{3.10}$$

with ρ_m the density of the material.

Using the definitions and relations above, the last equation gives a system for the displacements $u_i, i = 1, 2, 3$ and is given by[1]:

$$\begin{cases} \rho_m \dfrac{\partial^2 u_1}{\partial t^2} &= \lambda \dfrac{\partial}{\partial x_1} (\nabla \cdot \boldsymbol{u}) + \mu \left(\nabla \cdot \left(\nabla u_1 + \dfrac{\partial \boldsymbol{u}}{\partial x_1} \right) \right) + b_1 \\ \rho_m \dfrac{\partial^2 u_2}{\partial t^2} &= \lambda \dfrac{\partial}{\partial x_2} (\nabla \cdot \boldsymbol{u}) + \mu \left(\nabla \cdot \left(\nabla u_2 + \dfrac{\partial \boldsymbol{u}}{\partial x_2} \right) \right) + b_2 \\ \rho_m \dfrac{\partial^2 u_3}{\partial t^2} &= \lambda \dfrac{\partial}{\partial x_3} (\nabla \cdot \boldsymbol{u}) + \mu \left(\nabla \cdot \left(\nabla u_3 + \dfrac{\partial \boldsymbol{u}}{\partial x_3} \right) \right) + b_3. \end{cases} \tag{3.11}$$

On the boundary of the system still conditions need to be imposed. From a physical point of view there are three things that can happen at a boundary Γ during rolling or extrusion:

- The boundary is fixed, so no displacements can occur.
- A force is exerted on the boundary.
- A free boundary on which no forces act, besides internal forces.

The first physical situation can be represented by mathematics by demanding

$$\boldsymbol{u} = \boldsymbol{0} \qquad \text{on the boundary.}$$

If a force is exerted, this can be described by

$$\boldsymbol{\sigma} \cdot \boldsymbol{n} = \boldsymbol{f} \qquad \text{on the boundary,}$$

with $\boldsymbol{f} = \boldsymbol{f}(x, t)$ the force exerted and $\boldsymbol{n}$ the outward normal on the boundary. This boundary condition gives boundary conditions for the spatial derivatives of $u_i, i = 1, 2, 3$. If we take $\boldsymbol{f} \equiv 0$, we arrive at the

[1] Assuming constant values for ρ_m, λ, μ.

free boundary with no external forces. On a single region of the boundary the boundary condition can be generalized. A formal representation of a possible boundary condition is thus of the form:

$$\boldsymbol{\sigma} \cdot \boldsymbol{n} = \boldsymbol{f} + [\alpha_1(u_{b1} - u_1), \alpha_2(u_{b2} - u_2), \alpha_3(u_{b3} - u_3)]^T. \tag{3.12}$$

The initial conditions for (3.11) are determined by the initial state of the system. In most cases this state is the undeformed state of the system. This means that no displacements have occurred, but not that the system is in rest. This means that we can impose the initial conditions

$$\begin{cases} u(\boldsymbol{x}, 0) &= 0 \\ \dfrac{\partial u}{\partial t}(\boldsymbol{x}, 0) &= g(\boldsymbol{x}), \end{cases} \tag{3.13}$$

on our system, where $g(\boldsymbol{x})$ is any appropriate function, which can be integrated over the real numbers.

In the special case of one dimension, we can rewrite (3.11) to

$$\rho_m \frac{\partial^2 u}{\partial t^2} = (\lambda + 2\mu)\frac{\partial^2 u}{\partial x^2}.$$

If we set

$$c^2 = \frac{\rho_m}{\lambda + 2\mu},$$

we have the basic one dimensional wave equation

$$c^2 \frac{\partial^2 u}{\partial t^2} = \frac{\partial^2 u}{\partial x^2}.$$

Assume for simplicity that $u(x,t)$ satisfies inhomogeneous Dirichlet boundary conditions and the initial conditions (3.13) and the one dimensional wave equation on $(0,1)$:

$$\begin{cases} c^2 \dfrac{\partial^2 u}{\partial t^2} &= \frac{\partial^2 u}{\partial x^2} & \text{on } x \in (0,1) \text{ and for } t > 0, \\ u(0,t) &= f_1(t) & \text{for } t > 0, \\ u(1,t) &= f_2(t) & \text{for } t > 0, \\ u(x,0) &= 0 & \text{on } x \in [0,1], \\ \dfrac{\partial u}{\partial t}(x,0) &= g(x) & \text{on } x \in [0,1]. \end{cases}$$

If we set

$$u(x,t) = v(x,t) + w(x),$$

and demand that $v(x,t)$ satisfies the same initial conditions as u but with homogeneous boundary conditions and $w(x,t)$ satisfies $\partial^2 w/\partial x^2 = 0$, we have the following to systems:

$$\begin{cases} c^2 \dfrac{\partial^2 v}{\partial t^2} &= \dfrac{\partial^2 v}{\partial x^2} & \text{on } x \in (0,1) \text{ and for } t > 0, \\ v(0,t) &= 0 & \text{for } t > 0, \\ v(1,t) &= 0 & \text{for } t > 0, \\ v(x,0) &= 0 & \text{on } x \in [0,1], \\ \dfrac{\partial v}{\partial t}(x,0) &= g(x) & \text{on } x \in [0,1], \end{cases} \quad \text{and} \quad \begin{cases} \frac{\partial^2 w}{\partial x^2} &= 0 & \text{on } x \in (0,1) \text{ and for } t > 0, \\ w(0) &= f_1(t) & \text{for } t > 0, \\ w(1) &= f_2(t) & \text{for } t > 0. \end{cases}$$

The solution of the second system is easily determined and has time dependent constants:

$$w(x,t) = (f_2(t) - f_1(t))x + f_1(t)x.$$

The first system has as solution

$$v(x,t) = \sum_{k=1}^{\infty} B_k \sin(k\pi x) \sin\left(\frac{k\pi t}{c}\right),$$

where

$$B_k = \frac{c}{2k\pi} \int_0^1 g(x) \sin(k\pi x)\, \mathrm{d}x.$$

If we investigate the behavior of B_k, we see that we have the property:

$$\lim_{c \to 0} B_k = 0,$$

which immediately results in

$$\lim_{c \to 0} v(x,t) = 0.$$

This means that if c is small, the only time dependence of the solution $u(x,t)$ comes from the boundary conditions. This means we can easily neglect the time dependence in the wave equation and say that $u(x,t)$ satisfies the system

$$\begin{cases} \dfrac{d^2u}{dx^2} &= 0 & \text{on } x \in (0,1) \\ u(0) &= f_1(t) & \text{for } t > 0, \\ u(1) &= f_2(t) & \text{for } t > 0. \end{cases}$$

The result in the one dimensional case suggests that also in three dimensions the time dependency can be neglected, which results in the differential equation

$$\begin{cases} -\lambda \dfrac{\partial}{\partial x_1} (\nabla \cdot \boldsymbol{u}) - \mu \left(\nabla \cdot \left(\nabla u_1 + \dfrac{\partial \boldsymbol{u}}{\partial x_1} \right) \right) &= b_1 \\ -\lambda \dfrac{\partial}{\partial x_2} (\nabla \cdot \boldsymbol{u}) - \mu \left(\nabla \cdot \left(\nabla u_2 + \dfrac{\partial \boldsymbol{u}}{\partial x_2} \right) \right) &= b_2 \\ -\lambda \dfrac{\partial}{\partial x_3} (\nabla \cdot \boldsymbol{u}) - \mu \left(\nabla \cdot \left(\nabla u_3 + \dfrac{\partial \boldsymbol{u}}{\partial x_3} \right) \right) &= b_3, \end{cases} \tag{3.14}$$

with boundary condition (3.12). Note that the boundary condition still has a possible time dependency, so that we can solve (3.14) at several time instances to simulate time behavior.

Chapter 4

Numerical methods

This chapter will deal with the discretization of all models that have been formulated in the previous chapter. The model for nucleation and growth of particles will be discretized by the means of finite volume methods, all other models by means of finite element methods.

4.1 Nucleation and growth of particles

This section will continue on the previous chapter by discretizing the partial differential equation (3.5) in time and place. We will start with the spatial discretization, after which a time integration and linearization will take place. Then the discretization of the formulas needed will be given. Finally an algorithm will be given for solving our numerical scheme.

4.1.1 Spatial discretization

Integration over control interval

The spatial discretization of (3.5) will make use of the finite volume method, combined with an upwind scheme. To this end, we only calculate N on the region $[r_{\min}, r_{\max}]$. Now divide this region in M control intervals Ω_i with length Δr and boundary Γ_i. Denote by r_i the midpoint of interval Ω_i and N_i as the value of N on $r = r_i$.

Integration of the left-hand side of (3.5) over control interval Ω_i gives

$$\int_{\Omega_i} \frac{\partial N}{\partial t} dr \;=\; \frac{d}{dt} \int_{\Omega_i} N dr \;\approx\; \Delta r \frac{dN_i}{dt}$$

Integration of the first term in the right-hand side of (3.5) gives

$$\begin{aligned} -\int_{\Omega_i} \frac{\partial (Nv)}{\partial r} dr &= -\,(Nv)|_{\Gamma_i} \\ &= -\left((Nv)_{i+1/2} - (Nv)_{i-1/2}\right) \\ &\approx v^+_{i-1/2} N_{i-1} - (v^-_{i-1/2} + v^+_{i+1/2}) N_i + v^-_{i+1/2} N_{i+1} \end{aligned}$$

with the uses of an upwind discretization, v_i is short for $v(r_i, t)$ and the superscripts $+, -$ stand for the positive and negative parts respectively, which as been introduced to correctly use the upwind scheme.

Integration of the source term over Ω_i, gives

$$\int_{\Omega_i} S dr \approx \Delta r S_i$$

where S_i is short for $S(r_i, t)$.

Combining the discretizations we arrive at a matrix differential equation

$$\frac{d\vec{N}(t)}{dt} = A(t)\vec{N}(t) + \vec{S}(t), \tag{4.1}$$

where

$$\begin{array}{rcll} (\vec{N}(t))_i & = & N_i & \text{for } i = 1, \ldots, G-1 \\ (A(t))_{ii} & = & -\frac{1}{\Delta r}(v^-_{i-1/2} + v^+_{i+1/2}) & \text{for } i = 1, \ldots, G-1 \\ (A(t))_{i,i-1} & = & \frac{1}{\Delta r} v^+_{i-1/2} & \text{for } i = 2, \ldots, G-1 \\ (A(t))_{i,i+1} & = & \frac{1}{\Delta r} v^-_{i+1/2} & \text{for } i = 1, \ldots, G-1 \\ (\vec{S}(t))_i & = & S_i & \text{for } i = 1, \ldots, G-1, \end{array}$$

and $(A(t))_{ij} = 0$ if not defined above.

Properties of the discretized system

If we investigate the growth rate v and critical radius r^* at a certain time, we can see the following properties:

1. For each Ω_i with $r < r^*, r \in \Omega_i$ we have $v_{i-1/2}, v_{i+1/2} < 0$.
2. For each Ω_i with $r^* \in \Omega_i$ we have $v_{i-1/2} < 0, v_{i+1/2} > 0$.
3. For each Ω_i with $r > r^*, r \in \Omega_i$ we have $v_{i-1/2}, v_{i+1/2} > 0$.

Let i be such that we have the first case. Then we see that we must have:

$$(A(t))_{i,i+1} = v^-_{i+1/2} = -v_{i+1/2},$$

but also

$$(A(t))_{i+1,i} = (A(t))_{i+1,i+1-1} = v^+_{i+1-1/2} = v^+_{i+1/2} = 0.$$

But this means we have that only the upper and main diagonals are present in $A(t)$ in the first case. Now let i be such that we have the second case. Then we must have:

$$(A(t))_{i,i+1} = v^-_{i+1/2} = 0,$$

but also

$$(A(t))_{i,i-1} = v^+_{i-1/2} = 0.$$

This means that in the second case only the main diagonal is present in $A(t)$. If i is such that we have the thirth case, we have:

$$(A(t))_{i,i+1} = v^-_{i+1/2} = 0,$$

but also

$$(A(t))_{i+1,i} = (A(t))_{i+1,i+1-1} = v^+_{i+1-1/2} = v^+_{i+1/2} = v_{i+1/2}.$$

As a result only the main and lower diagonal in $A(t)$ have a non-zero value. The above defines the structure of $A(t)$ which can be depicted as

$$\begin{bmatrix} \times & \times & & & & & \\ & \times & \times & & & & \\ & & \times & \times & & & \\ & & & \times & & & \\ & & & \times & \times & & \\ & & & & \times & \times & \\ & & & & & \times & \times \end{bmatrix},$$

where $\times$ means that a non-zero value is present.

The time-dependent eigenvalues of $A(t)$ can now easily be determined, since those are simply the main diagonal entries. To see this, assume we have a matrix as above, with elements a_{ij}. For simplicity assume we have a 5-matrix with the following structure:

$$\begin{bmatrix} a_{11} & a_{12} & & & \\ & a_{22} & a_{23} & & \\ & & a_{33} & & \\ & & a_{43} & a_{44} & \\ & & & a_{54} & a_{55} \end{bmatrix}.$$

The characteristic polynomial of this matrix is:

$$\begin{vmatrix} a_{11}-\lambda & a_{12} & & & \\ & a_{22}-\lambda & a_{23} & & \\ & & a_{33}-\lambda & & \\ & & a_{43} & a_{44}-\lambda & \\ & & & a_{54} & a_{55}-\lambda \end{vmatrix} = (a_{11}-\lambda)\begin{vmatrix} a_{22}-\lambda & a_{23} & & \\ & a_{33}-\lambda & & \\ & a_{43} & a_{44}-\lambda & \\ & & a_{54} & a_{55}-\lambda \end{vmatrix}$$

$$= (a_{11}-\lambda)(a_{22}-\lambda)\begin{vmatrix} a_{33}-\lambda & & \\ a_{43} & a_{44}-\lambda & \\ & a_{54} & a_{55}-\lambda \end{vmatrix}$$

$$= (a_{11}-\lambda)(a_{22}-\lambda)(a_{33}-\lambda)\begin{vmatrix} a_{44}-\lambda & \\ a_{54} & a_{55}-\lambda \end{vmatrix}$$

$$= (a_{11}-\lambda)(a_{22}-\lambda)(a_{33}-\lambda)(a_{44}-\lambda)(a_{55}-\lambda).$$

This means that the eigenvalues are the main diagonal elements and the i-th eigenvalue of $A(t)$ is given by

$$\lambda_i = -(v^-_{i-1/2} + v^+_{i+1/2}),$$

which is real and negative for all values of i. This result implicates that any time integration method can be made stable as long as the stability region of this method contains (a part of) the negative real axis.

The order of the upwind method used in this section is $\mathcal{O}(\Delta r)$.

4.1.2 Time integration methods

The time integration of (4.1) will be done with several different methods. The methods discussed in this section are the θ-method and two Diagonal Implicit Runge-Kutta methods (DIRK-methods) (see [4]).

The θ-method

This section will discuss the θ-method with $\frac{1}{2} \leq \theta \leq 1$, resulting in an implicit method that is unconditionally stable for the system (4.1).

Let $\vec{N}^n$ be defined by

$$\vec{N}^n = \vec{N}(n\Delta t),$$

with Δt the time-step size and all other variables likewise. Then we can approximate system (4.1) with

$$\vec{N}^{n+1} = \vec{N}^n + (1-\theta)\frac{\Delta t}{\Delta r}A^n\vec{N}^n + \theta\frac{\Delta t}{\Delta r}A^{n+1}\vec{N}^{n+1} + (1-\theta)\Delta t\vec{S}^n + \theta\Delta t\vec{S}^{n+1}.$$

To be able to solve this system correctly we will linearize this system by approximating the matrix A^{n+1} and the vector $\vec{S}^{n+1}$ by there values at the previous time step n. This gives

$$\left(I - \theta\frac{\Delta t}{\Delta r}A^n\right)\vec{N}^{n+1} = \left(I + (1-\theta)\frac{\Delta t}{\Delta r}A^n\right)\vec{N}^n + \Delta t\vec{S}^n. \tag{4.2}$$

The discretization of the formulas in Chapter 3 will be down in a straightforward way when needed. The order of the θ-method is $\mathcal{O}(\Delta t)$ for $\theta \neq 1/2$ and $\mathcal{O}(\Delta t^2)$ for $\theta = 1/2$.

THE FIRST DIRK-METHOD

All Runge-Kutta methods that exist are designed for solving the problem

$$w'(t) = F(t, w(t)),$$

for $t > 0$ and an initial condition $w(0) = w_0$. Each method fulfills the general form

$$\begin{aligned} w^{n+1} &= w^n + \Delta t \sum_{i=1}^{s} b_i F(t^n + c_i \Delta t, w^{ni}) \\ w^{ni} &= w^n + \Delta t \sum_{j=1}^{s} \alpha_{ij} F(t^n + c_j \Delta t, w^{nj}) \qquad \text{for } i = 1, \ldots, s, \end{aligned}$$

where α_{ij}, b_i define the method and $c_i = \sum_{j=1}^{s} \alpha_{ij}$. Each Runge-Kutta method can be thus characterized by the values of α_{ij}, b_i and c_i, which can conveniently be expressed in a so-called Butcher array that has the form

$$\begin{array}{c|c} c & \mathcal{A} \\ \hline & b^t \end{array} = \begin{array}{c|ccc} c_1 & \alpha_{11} & \cdots & \alpha_{1s} \\ \vdots & \vdots & \ddots & \vdots \\ c_s & \alpha_{s1} & \cdots & \alpha_{ss} \\ \hline & b_1 & \cdots & b_s \end{array}.$$

The first DIRK-method used is due to Nørsett [8] and Crouzeix [2] and is given by the Butcher array

$$\begin{array}{c|cc} \gamma & \gamma & 0 \\ 1-\gamma & 1-2\gamma & \gamma \\ \hline & 1/2 & 1/2 \end{array},$$

with $\gamma > 0$. Applying this array to the general Runge-Kutta form gives

$$\begin{aligned} w^{n+1} &= w^n + \frac{\Delta t}{2}\left(F(t^n + \gamma\Delta t, w^{n1}) + F(t^n + (1-\gamma)\Delta t, w^{n2})\right) \\ w^{n1} &= w^n + \Delta t \gamma F(t^n + \gamma \Delta t, w^{n1}) \\ w^{n2} &= w^n + \Delta t\left((1-2\gamma)F(t^n + \gamma\Delta t, w^{n1}) + \gamma F(t^n + (1-\gamma)\Delta t, w^{n2})\right), \end{aligned}$$

as numerical scheme.

Applying this model to (4.1) the following system results

$$\begin{aligned} \vec{N}^{n+1} &= \vec{N}^n + \frac{\Delta t}{2}\left(A(t^n + \gamma\Delta t)\vec{N}^{n1} + \vec{S}(t^n + \gamma\Delta t) + A(t^n + (1-\gamma)\Delta t)\vec{N}^{n2} + \vec{S}(t^n + (1-\gamma)\Delta t)\right) \\ \vec{N}^{n1} &= \vec{N}^n + \Delta t\gamma\left(A(t^n + \gamma\Delta t)\vec{N}^{n1} + \vec{S}(t^n + \gamma\Delta t)\right) \\ \vec{N}^{n2} &= \vec{N}^n + \Delta t\left((1-2\gamma)\left(A(t^n + \gamma\Delta t)\vec{N}^{n1} + \vec{S}(t^n + \gamma\Delta t)\right) + \left(\gamma A(t^n + (1-\gamma)\Delta t)\vec{N}^{n2} + \vec{S}(t^n + (1-\gamma)\Delta t)\right)\right). \end{aligned}$$

To be able to solve this system correctly we will linearize this system by approximating the matrix A and vector $\vec{S}$ at other times than t^n by there values at the time step n. This gives

$$\begin{aligned} \vec{N}^{n+1} &= \vec{N}^n + \frac{\Delta t}{2} A^n\left(\vec{N}^{n1} + \vec{N}^{n2}\right) + \Delta t \vec{S}^n \\ \vec{N}^{n1} &= \vec{N}^n + \Delta t\gamma\left(A^n\vec{N}^{n1} + \vec{S}^n\right) \\ \vec{N}^{n2} &= \vec{N}^n + \Delta t A^n\left((1-2\gamma)\vec{N}^{n1} + \gamma\vec{N}^{n2}\right) + \Delta t(1-\gamma)\vec{S}^n. \end{aligned}$$

The order of this method is $\mathcal{O}(\Delta t^3)$ if $\gamma = \frac{1}{2} \pm \frac{1}{6}\sqrt{3}$ and $\mathcal{O}(\Delta t^2)$ otherwise. Also is known that this method is unconditionally stable for (4.1) if $\gamma \geq 1/4$.

The second DIRK-method

The second DIRK-method used is attributed to Alt (1973) by Crouzeix and Raviart [3] and is given by the Butcher array

$$\begin{array}{c|ccc} 0 & 0 & 0 & 0 \\ 2\gamma & \gamma & \gamma & 0 \\ 1 & b_1 & b_2 & \gamma \\ \hline & b_1 & b_2 & \gamma \end{array},$$

with $\gamma > 0$, $b_1 = \frac{3}{2} - \gamma - \frac{1}{4\gamma}$ and $b_2 = -\frac{1}{2} + \frac{1}{4\gamma}$. Applying this array to the general Runge-Kutta form gives

$$\begin{aligned} w^{n+1} &= w^n + \Delta t \left(b_1 F(t^n, w^{n1}) + b_2 F(t^n + 2\gamma\Delta t, w^{n2}) + \gamma F(t^n + \Delta t, w^{n3}) \right) \\ w^{n1} &= w^n \\ w^{n2} &= w^n + \Delta t\gamma \left(F(t^n, w^{n1}) + F(t^n + 2\gamma\Delta t, w^{n2}) \right) \\ w^{n3} &= w^n + \Delta t \left(b_1 F(t^n, w^{n1}) + b_2 F(t^n + 2\gamma\Delta t, w^{n2}) + \gamma F(t^n + \Delta t, w^{n3}) \right), \end{aligned}$$

as numerical scheme.

Applying this model to (4.1) and again linearizing the model as before, the following system results

$$\begin{aligned} \vec{N}^{n+1} &= \vec{N}^n + \Delta t A^n \left(b_1 \vec{N}^{n1} + b_2 \vec{N}^{n2} + \gamma \vec{N}^{n3} \right) + \Delta t \vec{S}^n \\ \vec{N}^{n1} &= \vec{N}^n \\ \vec{N}^{n2} &= \vec{N}^n + \Delta t\gamma A^n \left(\vec{N}^{n1} + \vec{N}^{n2} \right) + 2\Delta t\gamma \vec{S}^n \\ \vec{N}^{n3} &= \vec{N}^n + \Delta t A^n \left(b_1 \vec{N}^{n1} + b_2 \vec{N}^{n2} + \gamma \vec{N}^{n3} \right) + \Delta t \vec{S}^n. \end{aligned}$$

The order of this method is $\mathcal{O}(\Delta t^3)$ if $\gamma = \frac{1}{2} \pm \frac{1}{6}\sqrt{3}$ and $\mathcal{O}(\Delta t^2)$ otherwise. Also is known that this method is unconditionally stable for (4.1) if $\gamma \geq 1/4$.

4.1.3 Solution algorithm

If we look at the structure of the matrix A^n, we see that it is a tri-diagonal matrix, which will only be altered on the diagonal or with a constant factor. A a result we can use the Tri-Diagonal Matrix Algorithm, also known as the Thomas algorithm. For a system that has the form

$$\begin{bmatrix} b_1 & c_1 & & & 0 \\ a_2 & b_2 & c_2 & & \\ & a_3 & b_3 & . & \\ & & . & . & c_{n-1} \\ 0 & & & a_n & b_n \end{bmatrix} \begin{bmatrix} x_1 \\ x_2 \\ . \\ . \\ x_n \end{bmatrix} = \begin{bmatrix} d_1 \\ d_2 \\ . \\ . \\ d_n \end{bmatrix},$$

with $a_1 = 0$ and $c_n = 0$, the algorithm starts with a first forward sweep, that modifies the coefficients of the system. This sweep produces the following coefficients with corresponding formula:

$$\begin{aligned} c'_i &= \begin{cases} \frac{c_i}{b_i} & \text{for } i = 1 \\ \frac{c_i}{b_i - c'_{i-1} a_i} & \text{for } i = 2, \dots n \end{cases} \\ d'_i &= \begin{cases} \frac{d_i}{b_i} & \text{for } i = 1 \\ \frac{d_i - d'_{i-1} a_i}{b_i - c'_{i-1} a_i} & \text{for } i = 2, \dots n. \end{cases} \end{aligned}$$

The system produced has the form:

$$\begin{bmatrix} 1 & c'_1 & & & 0 \\ & 1 & c'_2 & & \\ & & 1 & . & \\ & & & . & c'_{n-1} \\ 0 & & & & 1 \end{bmatrix} \begin{bmatrix} x_1 \\ x_2 \\ . \\ . \\ x_n \end{bmatrix} = \begin{bmatrix} d'_1 \\ d'_2 \\ . \\ . \\ d'_n \end{bmatrix}.$$

This system can be solved by a backward sweep defined by

$$x_i = \begin{cases} d'_n & \text{for } i = n \\ d'_i - c'_i x_{i+1} & \text{for } i = n-1, \ldots, 1. \end{cases}$$

A derivation of this algorithm can be found at [1].

4.2 Elastic deformations

To be able to derive the numerical scheme for the system (3.14), several steps have to be performed. First a weak formulation has to be found, after which an approximation of the solution should be imposed. The last step is to derive the element matrices and vectors. These steps will be performed on the three dimensional model, but first we will discuss the application of these steps on the two dimensional version of (3.14).

4.2.1 Two dimensional model

The model

Although we have derived a three dimensional model, an understanding of this model can be obtained by simulation of the corresponding two dimensional model. This model can be derived from (3.14) by assuming no dependency on x_3 and that no displacements u_3 occur. This reduces the model to:

$$\begin{cases} -\lambda \dfrac{\partial}{\partial x_1} (\nabla \cdot \boldsymbol{u}) - \mu \left(\nabla \cdot \left(\nabla u_1 + \dfrac{\partial \boldsymbol{u}}{\partial x_1} \right) \right) &= b_1 \\ -\lambda \dfrac{\partial}{\partial x_2} (\nabla \cdot \boldsymbol{u}) - \mu \left(\nabla \cdot \left(\nabla u_2 + \dfrac{\partial \boldsymbol{u}}{\partial x_2} \right) \right) &= b_2. \end{cases} \tag{4.3}$$

∇ now refers to $(\partial/\partial x_1, \partial/\partial x_2)^T$.

The weak formulation

To obtain the weak formulation of (4.3) denote by $v_i(\boldsymbol{x}, t), i = 1, 2$ the test functions with $v_i = 0$ on those parts of the boundary for which $u_i = 0$. Instead of using the equations as in (4.3) to derive the weak formulation, we will use the equivalent system

$$-\nabla \cdot \boldsymbol{\sigma} = \boldsymbol{b}. \tag{4.4}$$

Multiplying the i-th row of (4.4) with v_i and integration over the domain Ω results in the system

$$-\int_\Omega (\nabla \cdot \boldsymbol{\sigma})_i \, v_i \, \mathrm{d}\Omega = \int_\Omega b_i v_i \, \mathrm{d}\Omega.$$

The first integral in this equation can be simplified by using the divergence theorem and the boundary condition (3.12):

$$\begin{aligned} \int_\Omega (\nabla \cdot \boldsymbol{\sigma})_i \, v_i \, \mathrm{d}\Omega &= \int_\Omega \left(\nabla \cdot \begin{bmatrix} \sigma_{i1} \\ \sigma_{i2} \end{bmatrix} \right)_i v_i \, \mathrm{d}\Omega \\ &= -\int_\Omega \begin{bmatrix} \sigma_{i1} \\ \sigma_{i2} \end{bmatrix} \cdot \nabla v_i \, \mathrm{d}\Omega + \int_\Gamma \left(\begin{bmatrix} \sigma_{i1} \\ \sigma_{i2} \end{bmatrix} \cdot \boldsymbol{n} \right) v_i \, \mathrm{d}\Gamma \\ &= -\int_\Omega \begin{bmatrix} \sigma_{i1} \\ \sigma_{i2} \end{bmatrix} \cdot \nabla v_i \, \mathrm{d}\Omega + \int_\Gamma (f_i + \alpha_i (u_{bi} - u_i)) \, v_i \, \mathrm{d}\Gamma. \end{aligned}$$

This means we get the following weak formulation of (4.3) where the definition of σ_{ij} should be filled in:

$$\int_\Omega \begin{bmatrix} \sigma_{i1} \\ \sigma_{i2} \end{bmatrix} \cdot \nabla v_i \, \mathrm{d}\Omega + \alpha_i \int_\Gamma u_i v_i \, \mathrm{d}\Gamma = \int_\Omega b_i v_i \, \mathrm{d}\Omega + \int_\Gamma (f_i + \alpha_i u_{bi}) v_i \, \mathrm{d}\Gamma \qquad \text{for } i = 1, 2. \tag{4.5}$$

Galerkin's method

Next we will apply Galerkin's method on (4.5). Let $\varphi_k(\boldsymbol{x}), k = 1, 2, \ldots$ by any appropriate set of basis functions on Ω. Now approximate u_i by

$$u_i(\boldsymbol{x}, t) \approx \sum_{l=1}^{n+n_b} u_{il}\varphi_l(\boldsymbol{x}),$$

where $n+n_b$ is the total number of internal grid points and boundary points and set $v_i = \varphi_k$. Substitution into (4.5) results after manipulation and substitution of the definition of σ_{ij} in

$$\begin{bmatrix} S_{11} & S_{12} \\ S_{21} & S_{22} \end{bmatrix} \begin{bmatrix} \boldsymbol{u}_1 \\ \boldsymbol{u}_2 \end{bmatrix} = \begin{bmatrix} \boldsymbol{q}_1 \\ \boldsymbol{q}_2 \end{bmatrix}, \tag{4.6}$$

and using the Hooke's Law (see equation (3.9)) gives:

$$\begin{aligned} \partial(S_{ij})_{kl} = \delta_{ij}\mu \sum_{m=1}^{2} \int_\Omega \frac{\partial\varphi_k}{\partial x_m}\frac{\partial\varphi_l}{\partial x_m}\,\mathrm{d}\Omega + \lambda\int_\Omega \frac{\partial\varphi_k}{\partial x_i}\frac{\partial\varphi_l}{\partial x_j}\,\mathrm{d}\Omega \\ + \mu\int_\Omega \frac{\partial\varphi_k}{\partial x_j}\frac{\partial\varphi_l}{\partial x_i}\,\mathrm{d}\Omega + \delta_{ij}\alpha_i\int_\Gamma \varphi_k\varphi_l\,\mathrm{d}\Gamma \qquad \text{for } i,j = 1,2 \quad \text{and for } k,l = 1,\ldots,n+n_b \\ (q_i)_k = b_i\int_\Omega \varphi_k\,\mathrm{d}\Omega + \int_\Gamma f_i\varphi_k\,\mathrm{d}\Gamma + \alpha_i u_{bi}\int_\Gamma \varphi_k\,\mathrm{d}\Gamma \qquad \text{for } i = 1,2 \qquad \text{and for } k = 1,\ldots,n+n_b. \end{aligned}$$

Element matrices and vectors

This section will state the element matrices and vectors for internal elements and boundary elements of the domain Ω and boundary Γ. We choose as internal elements linear triangles and as a result linear lines as boundary elements. The Newton-Cotes quadrature for an internal element e with points $\boldsymbol{x}_i, i = 1, \ldots, 3$ is

$$\int_e f\,\mathrm{d}\Omega = \frac{|\Delta|}{6}\sum_{i=1}^{3} f(\boldsymbol{x}_i),$$

where $|\Delta|/2$ is the area of e and for a boundary element b

$$\int_b f\,\mathrm{d}\Gamma = \frac{l}{2}\sum_{i=1}^{2} f(\boldsymbol{x}_i),$$

where l is the length of b.

The basis function φ_i can be represented by the formula

$$\varphi_i(\boldsymbol{x}) = a_i^0 + \begin{bmatrix} a_i^1 \\ a_i^2 \end{bmatrix} \cdot \boldsymbol{x},$$

where a_i^0, a_i^1, a_i^2 can be solved from the equation

$$\begin{bmatrix} 1 & x_1^1 & x_1^2 \\ 1 & x_2^1 & x_2^2 \\ 1 & x_3^1 & x_3^2 \end{bmatrix} \begin{bmatrix} a_i^0 \\ a_i^1 \\ a_i^2 \end{bmatrix} = \begin{bmatrix} \delta_{i1} \\ \delta_{i2} \\ \delta_{i3} \end{bmatrix}.$$

Using the above notations and quadratures we arrive for an internal element e at the element matrices and vectors:

$$\begin{aligned} (S_{ij}^e)_{kl} = \frac{|\Delta|}{2}\left(\lambda a_k^i a_l^j + \mu a_k^j a_l^i + \delta_{ij}\mu\sum_{m=1}^{2} a_k^m a_l^m\right) \qquad \text{for } i,j = 1,2 \qquad \text{and for } k,l = 1,2,3 \\ (q_i^e)_k = \frac{|\Delta|}{6}b_i \qquad \text{for } i = 1,2 \qquad \text{and for } k = 1,2,3, \end{aligned}$$

and for a boundary element b

$$(S_{ij}^b)_{kl} = \alpha_i \delta_{kl} \delta_{ij} \frac{l}{2} \qquad \text{for } i,j = 1,2 \qquad \text{and for } k,l = 1,2$$
$$(q_i^b)_k = \frac{l}{2} f_i(\boldsymbol{x}_k) + \frac{l}{2} \alpha_i u_{bi} \qquad \text{for } i = 1,2 \qquad \text{and for } k = 1,2.$$

4.2.2 Three dimensional model

The weak formulation

To obtain the weak formulation of (3.14) denote by $v_i(\boldsymbol{x},t), i = 1,2,3$ the test functions with $v_i = 0$ on those parts of the boundary for which $u_i = 0$. Instead of using the equations as in (3.14) to derive the weak formulation, we will use the equivalent system (3.10) in its time independent form:

$$-\nabla \cdot \boldsymbol{\sigma} = \boldsymbol{b}. \tag{4.7}$$

Multiplying the i-th row of (4.7) with v_i and integration over the domain Ω results in the system

$$-\int_\Omega (\nabla \cdot \boldsymbol{\sigma})_i \, v_i \, \mathrm{d}\Omega = \int_\Omega b_i v_i \, \mathrm{d}\Omega.$$

The second integral in this equation can be simplified by using the divergence theorem and the boundary condition (3.12):

$$\begin{aligned}
\int_\Omega (\nabla \cdot \boldsymbol{\sigma})_i \, v_i \, \mathrm{d}\Omega &= \int_\Omega \left(\nabla \cdot \begin{bmatrix} \sigma_{i1} \\ \sigma_{i2} \\ \sigma_{i3} \end{bmatrix} \right)_i v_i \, \mathrm{d}\Omega \\
&= -\int_\Omega \begin{bmatrix} \sigma_{i1} \\ \sigma_{i2} \\ \sigma_{i3} \end{bmatrix} \cdot \nabla v_i \, \mathrm{d}\Omega + \int_\Gamma \left(\begin{bmatrix} \sigma_{i1} \\ \sigma_{i2} \\ \sigma_{i3} \end{bmatrix} \cdot \boldsymbol{n} \right) v_i \, \mathrm{d}\Gamma \\
&= -\int_\Omega \begin{bmatrix} \sigma_{i1} \\ \sigma_{i2} \\ \sigma_{i3} \end{bmatrix} \cdot \nabla v_i \, \mathrm{d}\Omega + \int_\Gamma \left(f_i + \alpha_i (u_{bi} - u_i) \right) v_i \, \mathrm{d}\Gamma.
\end{aligned}$$

This means we get the following weak formulation of (3.14) where the definition of σ_{ij} should be filled in:

$$\int_\Omega \begin{bmatrix} \sigma_{i1} \\ \sigma_{i2} \\ \sigma_{i3} \end{bmatrix} \cdot \nabla v_i \, \mathrm{d}\Omega + \alpha_i \int_\Gamma u_i v_i \, \mathrm{d}\Gamma = \int_\Omega b_i v_i \, \mathrm{d}\Omega + \int_\Gamma (f_i + \alpha_i u_{ib}) v_i \, \mathrm{d}\Gamma \qquad \text{for } i = 1,2,3. \tag{4.8}$$

Galerkin's method

Next we will apply Galerkin's method on (4.8). Let $\varphi_k(\boldsymbol{x}), k = 1,2,\ldots$ by any appropriate set of basis functions on Ω. Now approximate u_i by

$$u_i(\boldsymbol{x},t) \approx \sum_{l=1}^{n+n_b} u_{il} \varphi_l(\boldsymbol{x}),$$

where $n+n_b$ is the total number of internal grid points and boundary points and set $v_i = \varphi_k$. Substitution into (4.8) results after manipulation and substitution of the definition of σ_{ij} in

$$\begin{bmatrix} S_{11} & S_{12} & S_{13} \\ S_{21} & S_{22} & S_{23} \\ S_{31} & S_{32} & S_{33} \end{bmatrix} \begin{bmatrix} \boldsymbol{u}_1 \\ \boldsymbol{u}_2 \\ \boldsymbol{u}_3 \end{bmatrix} = \begin{bmatrix} \boldsymbol{q}_1 \\ \boldsymbol{q}_2 \\ \boldsymbol{q}_3 \end{bmatrix}, \tag{4.9}$$

and definitions:

$$(S_{ij})_{kl} = \delta_{ij}\mu \sum_{m=1}^{3} \int_\Omega \frac{\partial \varphi_k}{\partial x_m}\frac{\partial \varphi_l}{\partial x_m}\,\mathrm{d}\Omega + \lambda \int_\Omega \frac{\partial \varphi_k}{\partial x_i}\frac{\partial \varphi_l}{\partial x_j}\,\mathrm{d}\Omega$$
$$+ \mu \int_\Omega \frac{\partial \varphi_k}{\partial x_j}\frac{\partial \varphi_l}{\partial x_i}\,\mathrm{d}\Omega + \delta_{ij}\alpha_i \int_\Gamma \varphi_k \varphi_l\,\mathrm{d}\Gamma \qquad \text{for } i,j = 1,2,3 \quad \text{and for } k,l = 1,\ldots,n+n_b$$
$$(q_i)_k = b_i \int_\Omega \varphi_k\,\mathrm{d}\Omega + \int_\Gamma (f_i + \alpha_i u_{bi})\varphi_k\,\mathrm{d}\Gamma \qquad \text{for } i = 1,2,3 \quad \text{and for } k = 1,\ldots,n+n_b.$$

Element matrices and vectors

This section will state the element matrices and vectors for internal elements and boundary elements of the domain Ω and boundary Γ. We choose as internal elements linear tetrahedra and as a result linear triangles as boundary elements. The Newton-Cotes quadrature for an internal element e with points $\boldsymbol{x}_i, i = 1,\ldots,4$ is

$$\int_e f\,\mathrm{d}\Omega = \frac{|V|}{24}\sum_{i=1}^{4} f(\boldsymbol{x}_i),$$

where $|V|/6$ is the volume of e and for a boundary element b

$$\int_b f\,\mathrm{d}\Gamma = \frac{|\Delta|}{6}\sum_{i=1}^{3} f(\boldsymbol{x}_i),$$

where $|\Delta|/2$ is the area of b.

The basis function φ_i can be represented by the formula

$$\varphi_i(\boldsymbol{x}) = a_i^0 + \begin{bmatrix} a_i^1 \\ a_i^2 \\ a_i^3 \end{bmatrix} \cdot \boldsymbol{x},$$

where $a_i^0, a_i^1, a_i^2, a_i^3$ can be solved from the equation

$$\begin{bmatrix} 1 & x_1^1 & x_1^2 & x_1^3 \\ 1 & x_2^1 & x_2^2 & x_2^3 \\ 1 & x_3^1 & x_3^2 & x_3^3 \\ 1 & x_4^1 & x_4^2 & x_4^3 \end{bmatrix} \begin{bmatrix} a_i^0 \\ a_i^1 \\ a_i^2 \\ a_i^3 \end{bmatrix} = \begin{bmatrix} \delta_{i1} \\ \delta_{i2} \\ \delta_{i3} \\ \delta_{i4} \end{bmatrix}.$$

Using the above notations and quadratures we arrive for an internal element e at the element matrices and vectors:

$$(S_{ij}^e)_{kl} = \delta_{ij}\mu\frac{|V|}{6}\sum_{m=1}^{3} a_k^m a_l^m + \lambda\frac{|V|}{6}a_k^i a_l^j + \mu\frac{|V|}{6}a_k^j a_l^i \qquad \text{for } i,j = 1,2,3 \quad \text{and for } k,l = 1,2,3,4$$
$$(q_i^e)_k = b_i\frac{|V|}{24} \qquad \text{for } i = 1,2,3 \quad \text{and for } k = 1,2,3,4,$$

and for a boundary element b

$$(S_{ij}^b)_{kl} = \delta_{kl}\delta_{ij}\alpha_i\frac{|\Delta|}{6} \qquad \text{for } i,j = 1,2,3 \quad \text{and for } k,l = 1,2,3$$
$$(q_i^b)_k = \frac{|\Delta|}{6}f_i(\boldsymbol{x}_k) + \frac{|\Delta|}{6}\alpha_i u_{bi} \qquad \text{for } i = 1,2,3 \quad \text{and for } k = 1,2,3.$$

Chapter 5

Numerical results

This chapter has as purpose to state and discuss the results obtained from the numerical schemes in Chapter 4.

5.1 Particle nucleation and growth

In this section simulations of the numerical schemes from Section 4.1 will be performed with several applications. The first application will serve as a test case for the quality of the mathematical model formulated in Section 3.1. The second application will test the temperature dependence of the mathematical model. These two test cases are the first two simulations carried out by Myhr and Grong in [7]. The other applications involve the determination of usable values for θ and γ used in the numerical schemes, but also to determine the difference in results and work for those values of θ and γ that can be used.

5.1.1 Context of the simulations from [7]

Both simulations carried out in the next sections will be concerned with the nucleation and growth of particles in a block of the aluminum alloy AA 6082, characterized by a nominal composition of 0.9 wt% silicium and 0.63 wt% magnesium. Due to the strong bond that exists between the atoms of the molecul Mg_2Si, this ternary alloy can be viewed as a quasi-binary alloy (see Section 2.1).

The values of the parameters needed in the simulation are copied from [7] and are given in Table 5.1.

Parameter	Value
C_p	63.4
C_0	0.63
C_s	970
D_0	2.2×10^{-4}
A_0	1.622×10^{4}
j_0	9.66×10^{34}
Q_d	1.3×10^{5}
Q_s	4.7175×10^{4}
σ	0.2
V_m	3.95×10^{-5}
Δr^*	$0.05 r^*$

Table 5.1: Value of parameters used during simulation. Data from [7].

We will assume that no particles are present at the beginning of our simulations, which means that $N(r, 0) = 0$ for $r \in (0, \infty)$. The numerical values needed in the simulations can be found in Table 5.2. The value of Δt will be stated for each simulation separately.

The numerical scheme in use here will be the θ-method with $\theta = 1$, as this is the same scheme used in [7].

Parameter	Value
Δr	0.95×10^{-10}
G	100
$r_{\max}$	100×10^{-10}
$r_{\min}$	5×10^{-10}
θ	1

Table 5.2: Value of numerical parameters used during simulation.

5.1.2 Long term behavior

The first simulation in [7] investigates the long term behavior of a system of the alloy AA 6082 under influence of a temperature of $180°C$ or the equivalent temperature $453.15K$. This method is called prolonged artificial ageing in the field of metallurgy. During the simulation, we will let the time run from 1 to 3×10^6 seconds, which corresponds with approximately 35 days. The value of the time step will be $\Delta t = 1$. The results from the simulation can be found in Figures 5.1 and 5.2.

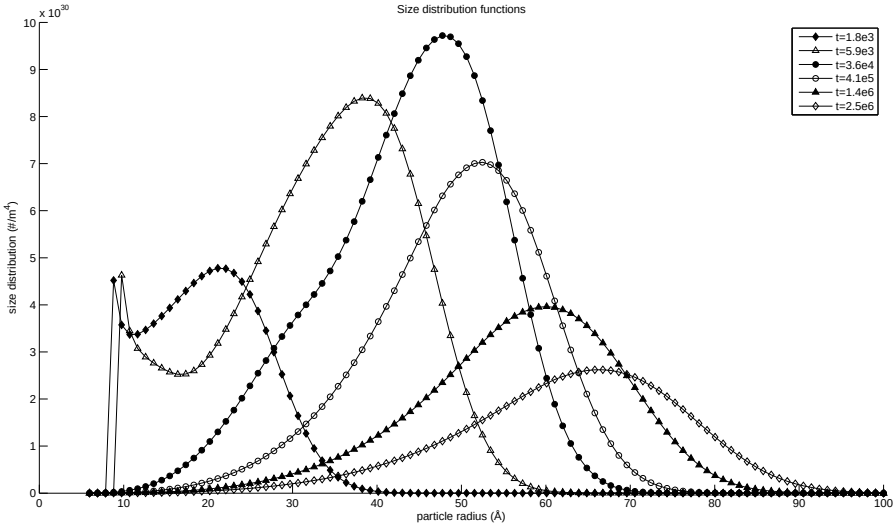

Figure 5.1: Evolution of the size distribution function ϕ during prolonged artificial ageing at $180°C$.

From these results we can observe that the behavior of the system consists of three subsequent stages. For the first 10^3 seconds, we see that the particle volume fraction f and the mean concentration $\bar{C}$ are close to constant. This means that the overall composition of the system does not change significantly. We also see that the nucleation rate j is also close to constant. This means that the overall number of particles should increase at a reasonable constant rate, which is the case as can be seen from Figure 5.2(b). Although the number of particles is increasing due to nucleation, the size of the particles remains small, since the mean radius $\bar{r}$ remains close to constant.

The next stage during the prolonged artificial ageing process is characterized by the growth of the particles present. This stages last from approximately 10^3 seconds to about 2×10^4 seconds. During this stage we see that the mean particles radius $\bar{r}$ increases rapidly and away from r^*, which is what should be expected, since only particles larger than r^* can increase. Due to the growth of the particles, the particle volume fraction starts to increase sharply and the mean concentration and nucleation rate drop significantly. The latter is a result from the fact that $\bar{C}$ approaches the equilibrium concentration C_e during this stage. Due to the low nucleation rate, the particle number density starts to stabilize.

During the prolonged artificial ageing process the last stage is the coarsening stage. This stage is characterized by the growth of larger particles at the expense of the smaller particles. This behavior can be observed by the fairly constant values of the particle volume fraction and mean concentration. We

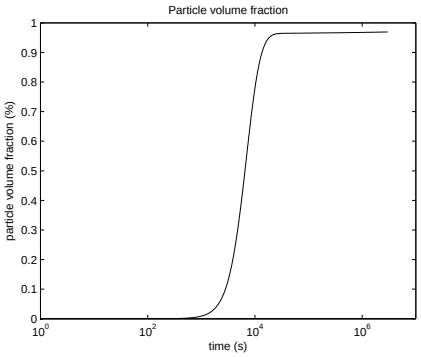

(a) Evolution of the particle volume fraction f during prolonged artificial ageing at $180°C$.

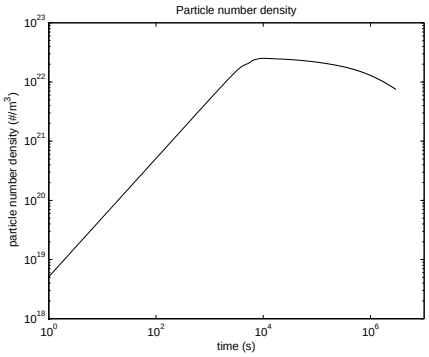

(b) Evolution of the particle number density n during prolonged artificial ageing at $180°C$.

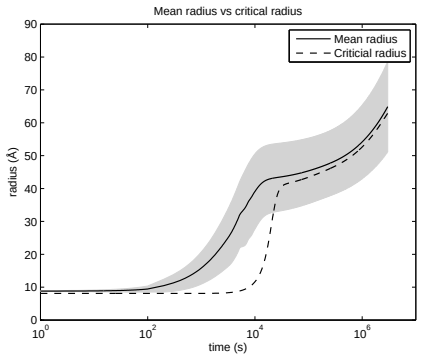

(c) Evolution of the particle radii $\bar{r}$ and r^* during prolonged artificial ageing at $180°C$. Shaded area is the spread of radii around $\bar{r}$ by the standard deviation ρ.

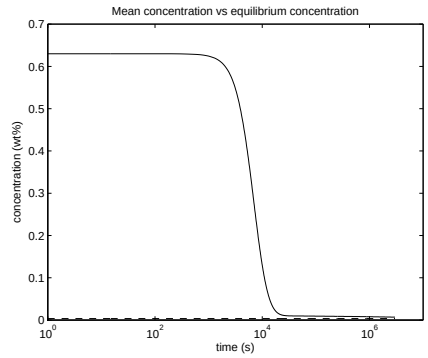

(d) Evolution of the concentrations $\bar{C}$ and C_e during prolonged artificial ageing at $180°C$.

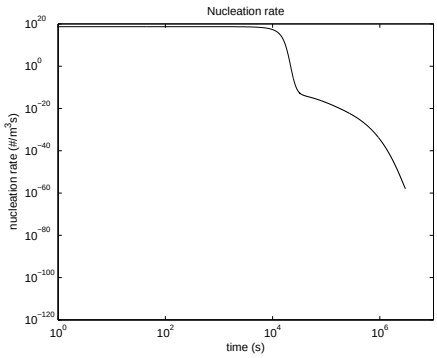

(e) Evolution of the nucleation rate j during prolonged artificial ageing at $180°C$.

Figure 5.2: Evolution of several quantities during prolonged ageing at 180° C.

also see that the mean radius and critical radius converges, but still continue to increase. Due to the dissolution of the smaller particles the number of particles starts to decrease, as can be observed from the particle number density.

Figure 5.1 contains two visible peaks that seem to be of an unphysical nature. If we investigate the height and location of each peak at the relevant times, we see that the peaks are of the magnitude $j/\Delta r$ at the location $r^* + \Delta r^*$. This means that the peaks are directly related to the nucleation term S of the model (3.5). In the later stages of the simulation the peaks do not show, since then the magnitude of $j/\Delta r$ is significantly lower than that of ϕ at the location $r^* + \Delta r^*$.

5.1.3 Up-quenching

The next simulation will be the up-quenching of the system of the alloy AA 6082. Up-quenching is a technique in which the alloy is aged at a fixed temperature after which the temperature is suddenly increased to a higher temperature. We will perform the same simulation as in [7], in which the system is aged for 10^4 seconds at a temperature of $180°C$ after which the temperature is increased to $380°C$. The behavior of the system at the temperature of $180°C$ can be found in the previous section. The behavior of the system at $380°C$ can be found in Figures 5.3 and 5.4. We have chosen $\Delta t = 1$ for the time at $180°C$ and $\Delta t = 10^{-2}$ at $380°C$.

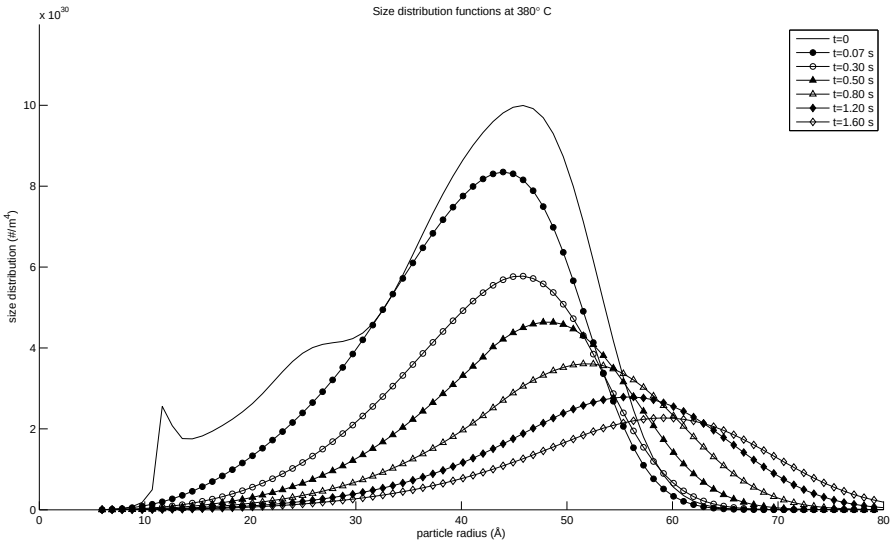

Figure 5.3: Evolution of the size distribution function ϕ during up-quenching at $380°C$. The time in this figure is the time *after* upquenching.

If we investigate the dependency of the derived quantities on the temperature, we see that the critical particle radius $r**$, the equilibrium concentration C_e and the nucleation rate j are influenced. The highest dependence on temperature has the critical particle radius, which can be seen in Figure 5.4(c), which shows a sudden increase of r^* at the temperature jump from $180°C$ to $380°C$.

During the time that the system is at $380°C$, it goes through two stages. The first stages last from 0 to 0.3 seconds and is characterized by a decreasing critical radius and particle volume fraction. This is due to the dissolving of the particles in the system. After enough particles have dissolved, the mean radius becomes larger then the critical radius and the second stage is entered.

The second stage consist of the growth of the remaining particles. The increase in the critical and mean particle radii is only due to the growth of the particles, since there is no or little nucleation, as can be seen from Figures 5.4(e) and 5.4(b). The growth initiates a increase in the particle volume fraction and decrease in the mean concentration, as should be expected.

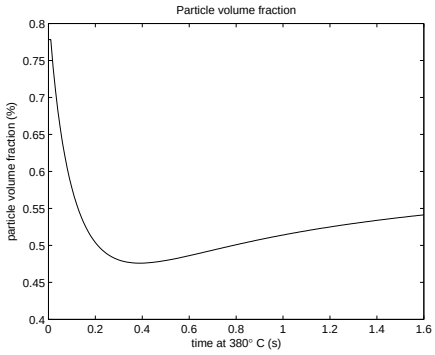

(a) Evolution of the particle volume fraction f during up-quenching at $380°C$.

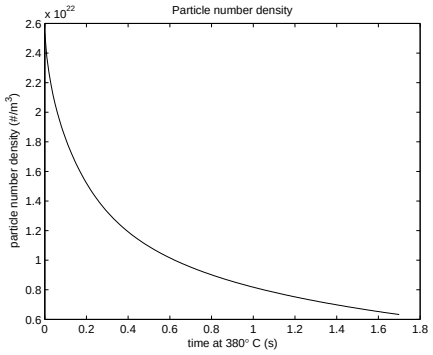

(b) Evolution of the particle number density n during up-quenching at $380°C$.

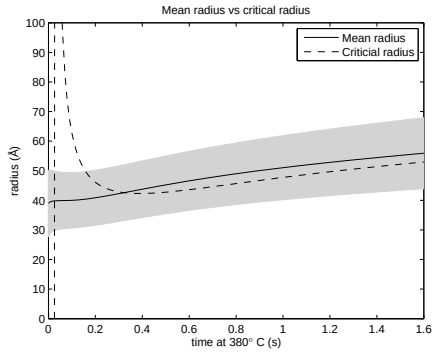

(c) Evolution of the particle radii $\bar{r}$ and r^* during up-quenching at $380°C$. Shaded area is the spread of radii around $\bar{r}$ by the standard deviation ρ.

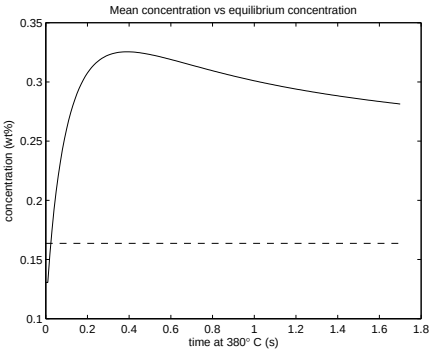

(d) Evolution of the concentrations $\bar{C}$ and C_e during up-quenching at $380°C$.

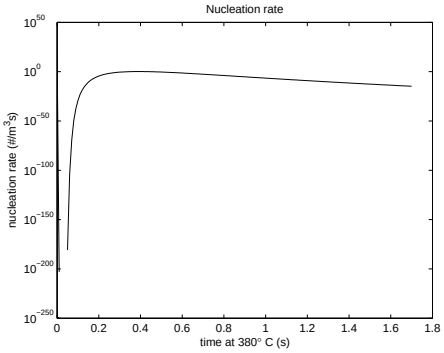

(e) Evolution of the nucleation rate j during up-quenching at $380°C$.

Figure 5.4: Evolution of several quantities during up-quenching at $380°C$.

5.1.4 The θ-method

This section will discuss simulations performed with the θ-method for different values of θ. First the values of θ for which correct physical results can be obtained are determined. After this the results for these values are discussed.

Correct values for θ-method

Although the numerical scheme (4.2) is unconditionally stable if we choose θ between 1/2 and 1, it does not mean that the results are physically correct. Since the function N defines the number of particles with a particular radius per cubic meter, we cannot have that this function becomes negative. This means that we cannot use those θ, if any, that produce negative numbers. Using the implementation in Matlab and a heuristic approach the lower and upper bound of the region for allowable values of θ for which no negative values occur during simulation can be determined. The bounds are calculated up to a precision of 5 digits. The simulation used is the same as in the first simulation, see Section 5.1.2.

The simulations resulted in the bounds as in Table 5.3. Figure 5.5 gives the minimum of ϕ for several θ below the lower bound as a function of time. Only those time regions for which negative values occur are plotted. In the next section results will be compared between values that fall between the two bounds.

Lower bound	Upper bound
0.56760	1.00000

Table 5.3: Numerically derived lower and upper bounds for θ.

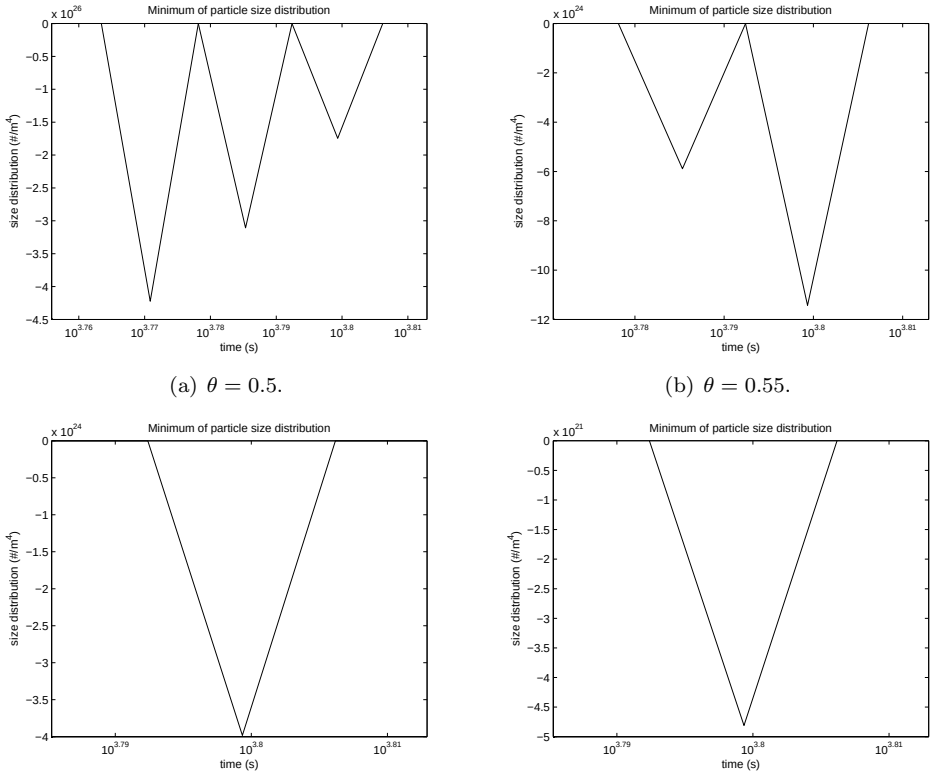

(a) $\theta = 0.5$.

(b) $\theta = 0.55$.

(c) $\theta = 0.56$.

(d) $\theta = 0.56758$.

Figure 5.5: Evolution of the minimum of ϕ for several $\theta < 0.56759$.

Comparison of θ-methods

Although the θ-method is stable and provides physically correct results if θ is between the bounds from Table 5.3, differences between the results at different θ could occur. To this end four simulations have been done in the same context as in Section 5.1.2 with θ from Table 5.4. The resulting figures of these simulations can be found in Figures 5.6 and 5.7.

Simulation	θ
1	0.5676
2	0.7
3	0.85
4	1

Table 5.4: Values of θ for which simulations have been done.

From the results obtained above some interesting conclusion can be drawn. The plots from Figure 5.6 seem to indicate that the different values for θ do not influence the outcome of the model at all, which means that choosing θ at a random value between the derived bounds gives the desired results. On the other hand, the plots in Figure 5.7 show that there is a difference in outcomes for the chosen values for θ. The difference between Figure 5.6 and Figure 5.7 can be explained by inspecting how the two plots of Figure 5.7 differ. In the plot of the sample standard deviation ρ it can be seen that for increasing θ ρ also increases. This means that the plots of the size distribution function ϕ will be wider for increasing θ. The plot of the maximum of ϕ shows that for increasing θ the maximum will decrease. This means that the size distribution ϕ will be lower for increasing θ. One can verify this result with the plot from Figure 5.8.

As a result the conclusion can be made that although the value of θ influences the shape of the size distribution slightly, it does not alter the outcome of the other functions, such as the particle volume fraction. This means that any θ between 0.5676 and 1 can be used. If we investigate the amount of work that must be done during simulation, we see that if $\theta \neq 1$ one matrix multiplication and one matrix inversion is needed per time step. If $\theta = 1$ only one matrix inversion is needed and no matrix multiplications are needed. This means that choosing $\theta = 1$ gives physically correct results at the lowest costs. This gives as a result that the method used by Myhr and Grong [7] is mathematically preferable, which is the combination of an upwind spacial discretization, an implicit Euler time integration[1] and a linearization in time.

To further compare the different values for θ, we have computed the time-dependent differences of the output form different θ with the output for $\theta = 1$ relative to the last. The chosen reference value $\theta = 1$ results from the fact that Myhr and Grong also use this value and their results have been assumed correct. The relative differences can be found in Figure 5.9.

If we say that a difference up to five percent is not relevant, the functions that come (temporarily) above this threshold, are the particle volume fraction f, the nucleation rate j, the sample standard deviation ρ and the maximum of the size distribution function ϕ. The relative differences with $\theta = 1$ for the last two functions can be explained by the same behavior observed above. Recalling the function for the particle volume fraction,

$$f(t) = \int_0^\infty \frac{4}{3}\pi r^3 \phi dr,$$

we can explain the relative differences for this function. We can formally say that a wider size distribution function ϕ will have more large particles, which influences the overall particle volume fraction. The moment in time at which the highest relative differences occur overlaps with the moment at which the particle size distribution and particle volume fraction rapidly increase in magnitude. Although the relative differences for f occur, they are not visible for the mean concentration $\bar{C}$. This can be explained by the fact that the formula for $\bar{C}$ involves a fraction with in the denominator and numerator the particle volume fraction, which cancels the effect of different f significantly. The peak in the relative differences for the nucleation rate j is six hundred percent, and occurs at the end of the algorithm. At this moment the value of j is of the order of $10^{-\alpha}$ with $\alpha \geq 40$, which is significantly small. This means that any deviation relative to $\theta = 1$ is of the order of $10^{-(\alpha+2)}$, which is neglectable in the overall system.

[1] This corresponds with the θ-method where $\theta = 1$.

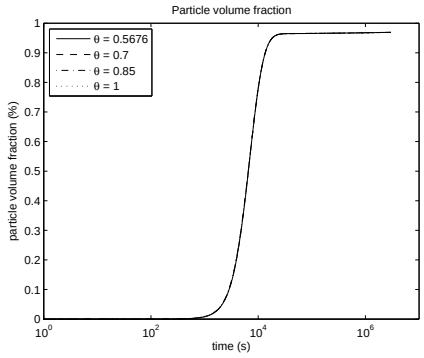

(a) Evolution of the particle volume fraction f.

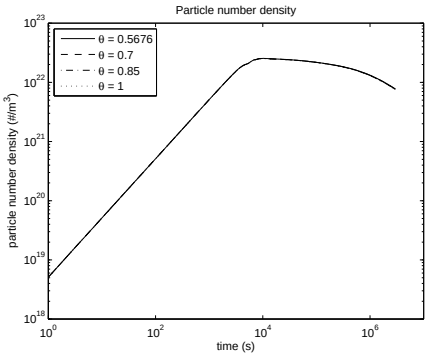

(b) Evolution of the particle number density n.

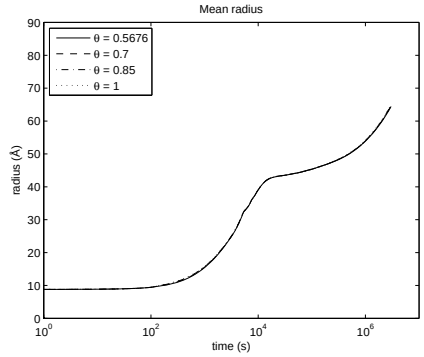

(c) Evolution of the mean particle radius $\bar{r}$.

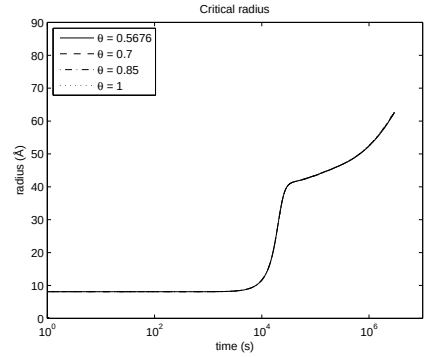

(d) Evolution of the critical particle radius r^*.

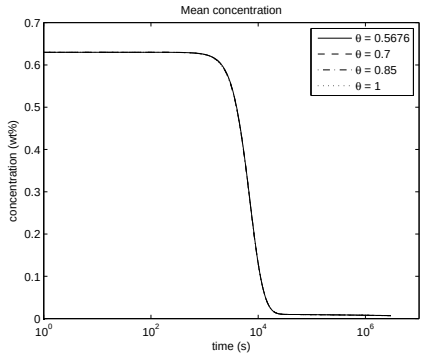

(e) Evolution of the mean concentration $\bar{C}$.

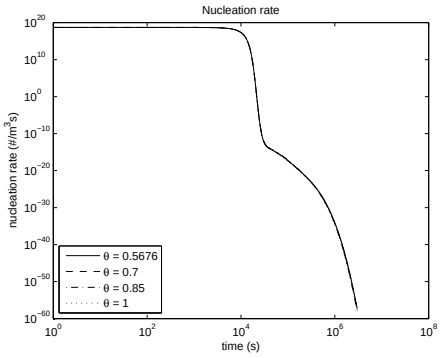

(f) Evolution of the nucleation rate j.

Figure 5.6: Results from simulation with various θ.

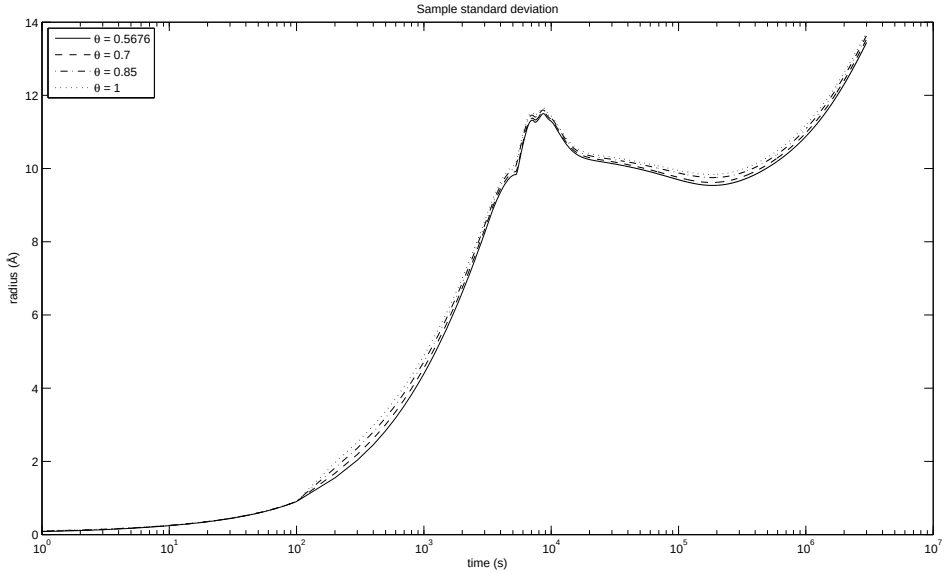

(a) Evolution of the sample standard deviation ρ of the particle radii.

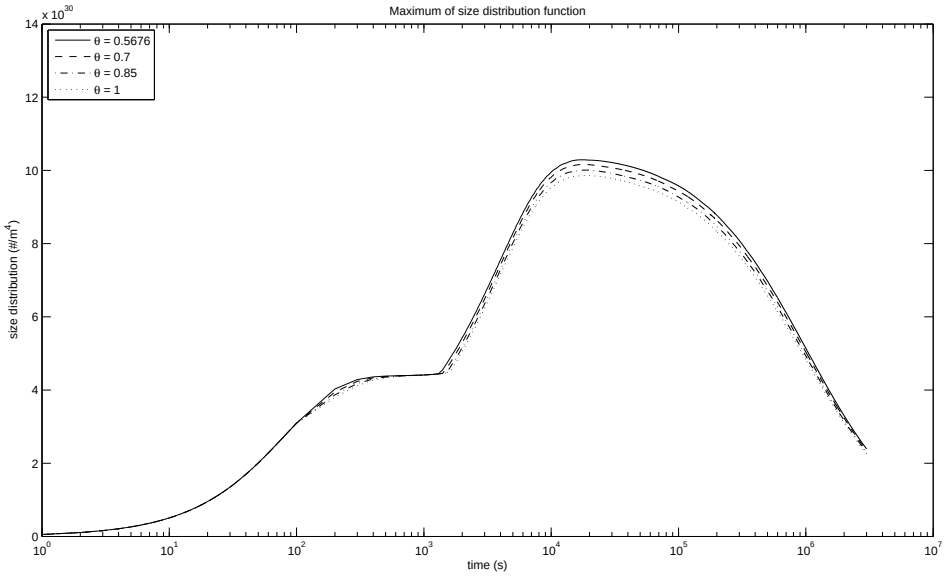

(b) Evolution of the maximum of particle size distribution function ϕ.

Figure 5.7: Results from simulation with various θ.

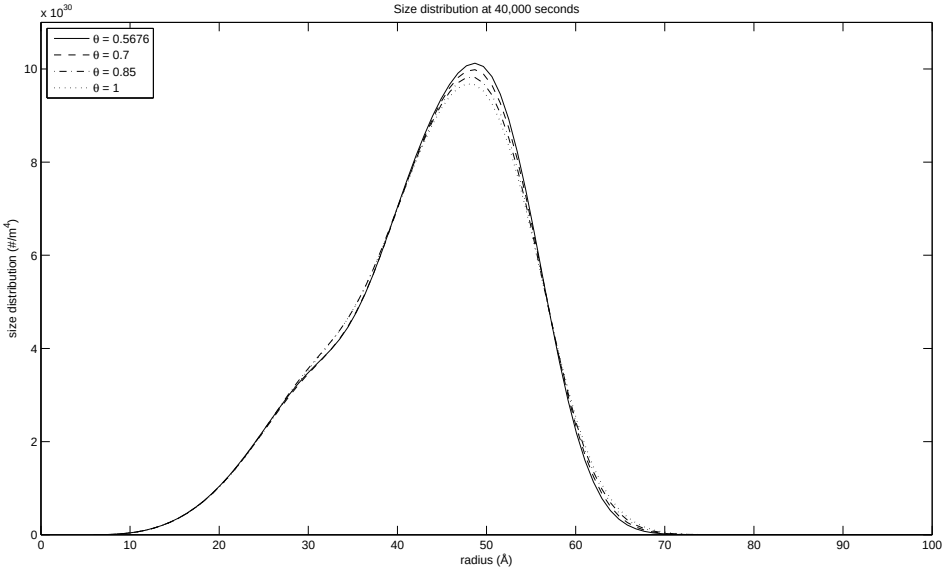

Figure 5.8: Snapshot of the size distribution ϕ at $40,000$ seconds for the chosen θ.

In some of the plots of Figure 5.9 a jump or sudden increase is visible at the time of 100 seconds. At this time the algorithm changes from a time step of one second to that of 100 seconds. To investigate the influence of this change in time step the simulation has be run with the change of the time step at the later time of $10,000$ seconds. This gave the relative results as in Figure 5.10. From these figures we can conclude that now some jumps are present at the time of 10,000 seconds, which means that the change in time step influences the performance of the algorithm. Since the size of the jumps is lower in the latter simulations, we will change the time step from 1 second to 100 seconds at the time of 10,000 seconds.

The change in the algorithm could have as effect that the bounds for θ change. Recalculation of these bounds gave the values as in Table 5.5. This means we can conclude two things. First that the value and adaption of Δt through time influences the physical outcome of the simulations. Second that a value of $\Delta t = 1$ is the best value to perform simulations.

Lower bound	Upper bound
0.50000	1.00000

Table 5.5: Numerically derived lower and upper bounds for θ.

The discussion about the relative differences for different values for θ confirms that although differences occur, these differences are neglectable. This supports the conclusion that choosing the value $\theta = 1$ results in the correct physical values for the model and results in the least amount of work. But the order of the time error is influenced by choosing $\theta = 1$ since the time error is of order Δt for all θ unequal to $\theta = 1/2$ and of order Δt^2 for $\theta = 1/2$. This means that although choosing $\theta = 1/2$ results in more computations, it will lead to more accurate results.

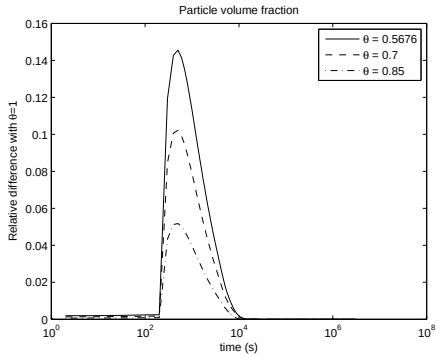

(a) Evolution of the relative particle volume fraction f.

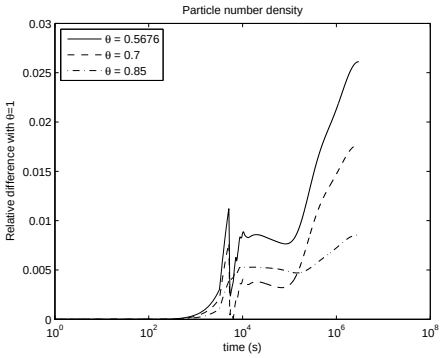

(b) Evolution of the relative particle number density n.

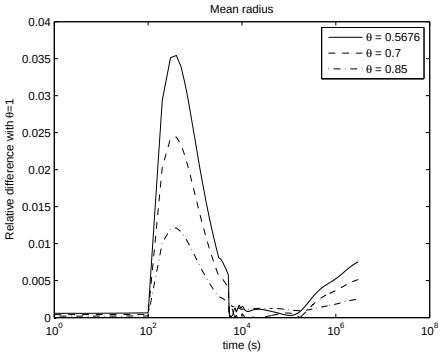

(c) Evolution of the relative mean particle radius $\bar{r}$.

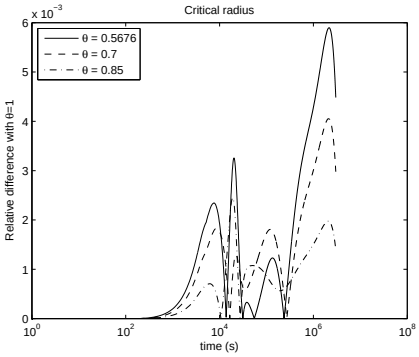

(d) Evolution of the relative critical particle radius r^*.

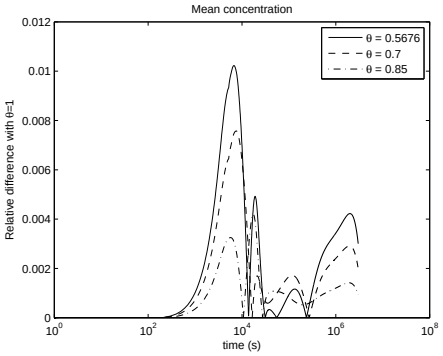

(e) Evolution of the relative mean concentration $\bar{C}$.

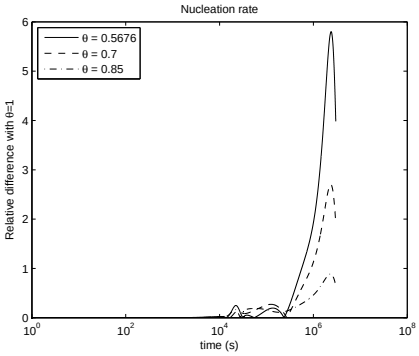

(f) Evolution of the relative nucleation rate j.

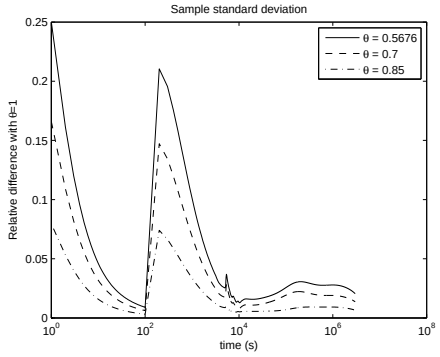

(g) Evolution of the relative sample standard deviation ρ.

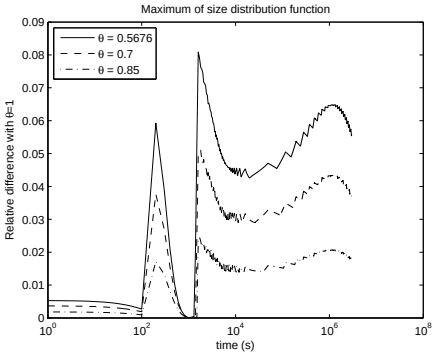

(h) Evolution of the relative maximum of size distribution function ϕ.

Figure 5.9: Relative results from simulation with various θ.

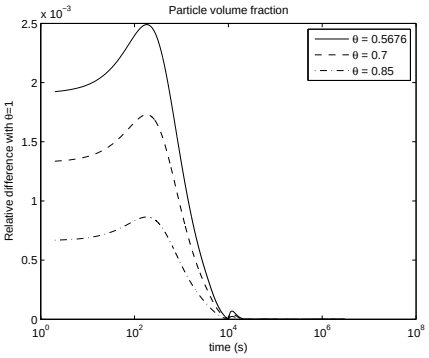

(a) Evolution of the relative particle volume fraction f.

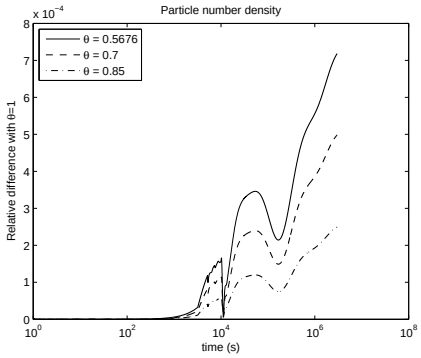

(b) Evolution of the relative particle number density n.

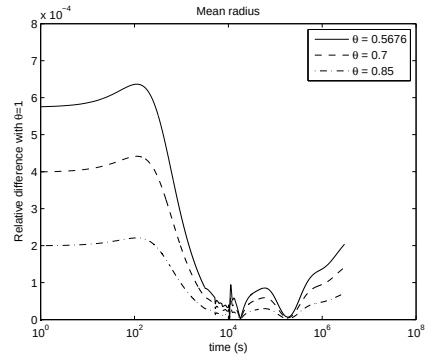

(c) Evolution of the relative mean particle radius $\bar{r}$.

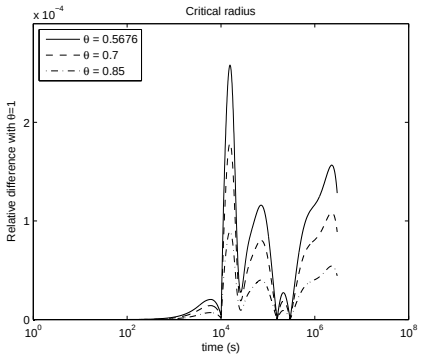

(d) Evolution of the relative critical particle radius r^*.

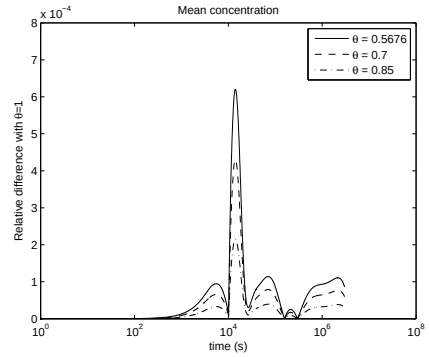

(e) Evolution of the relative mean concentration $\bar{C}$.

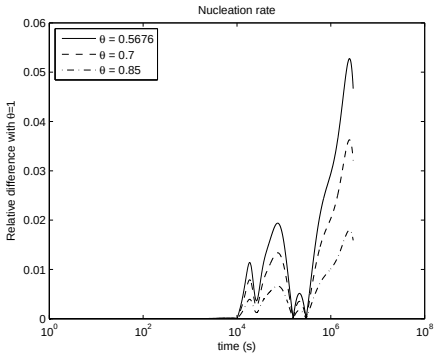

(f) Evolution of the relative nucleation rate j.

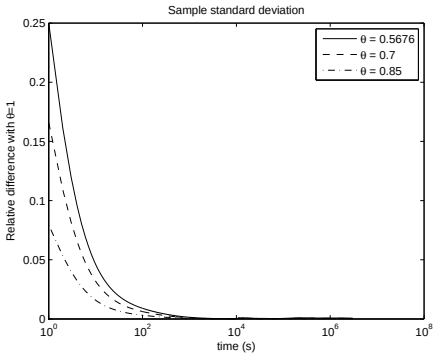

(g) Evolution of the relative sample standard deviation ρ.

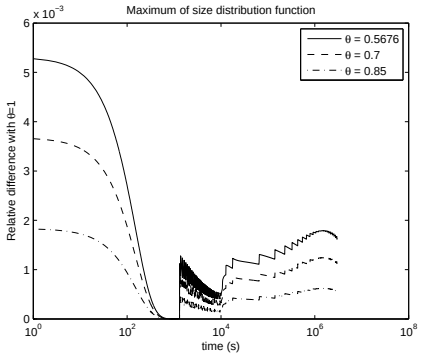

(h) Evolution of the relative maximum of size distribution function ϕ.

Figure 5.10: Relative results from simulation with various θ.

5.1.5 The first DIRK-method

This section will discuss simulations performed with the first DIRK-method for different values of γ. First the values of γ for which correct physical results can be obtained are determined. After this the results for these values are discussed.

Correct values for the first DIRK-method

Although the numerical scheme (4.2) is unconditionally stable if we choose γ above 1/4, it does not mean that the results are physically correct. Since the function N defines the number of particles with a particular radius per cubic meter, we cannot have that this function becomes negative. This means that we cannot use those γ, if any, that produce negative numbers. Using the implementation in Matlab and a heuristic approach the lower and upper bound of the region for which no negative values occur during simulation can be determined. The bounds are calculated up to 5 digits exact. The simulation used is the same as in the first simulation, see Section 5.1.2.

The simulations resulted in the bounds as in Table 5.6. Figure 5.11 gives the minimum of ϕ for several γ below the lower bound and above the upper bound as a function of time. Only those time regions for which negative values occur are plotted. In the next section results will be compared between values that fall between the two bounds.

Lower bound	Upper bound
0.25000	0.50533

Table 5.6: Numerically derived lower and upper bounds for γ.

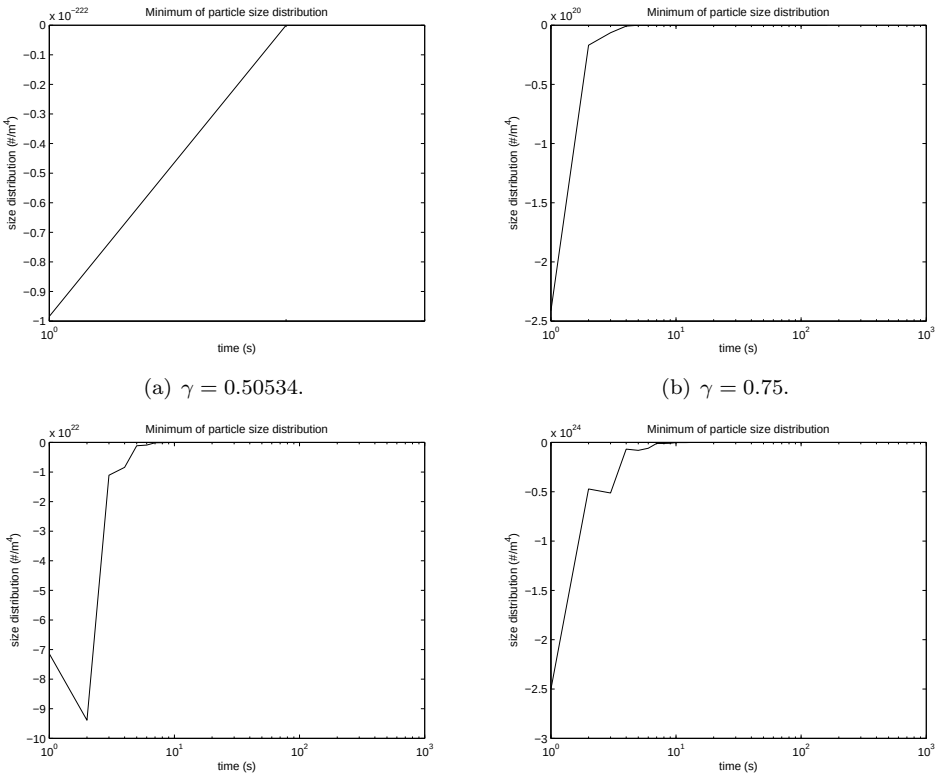

(a) $\gamma = 0.50534$.

(b) $\gamma = 0.75$.

(c) $\gamma = 1$.

(d) $\gamma = 1.25$.

Figure 5.11: Evolution of the minimum of ϕ for several γ.

Comparison of the first DIRK-method

Although the first DIRK-method is stable and provides physically correct results if γ is between the bounds from Table 5.6, differences between the results at different γ could occur. To this end four simulations have been done in the same context as in Section 5.1.2 with γ from Table 5.7. The resulting figures of these simulations can be found in Figures 5.12 and 5.13. The time step Δt has a value of 1 second for until a time of 10^4 seconds has been reached, after which Δt is increased to 100 seconds.

Simulation	γ
1	0.25
2	0.34
3	0.42
4	0.50533

Table 5.7: Values of γ for which simulations have been done.

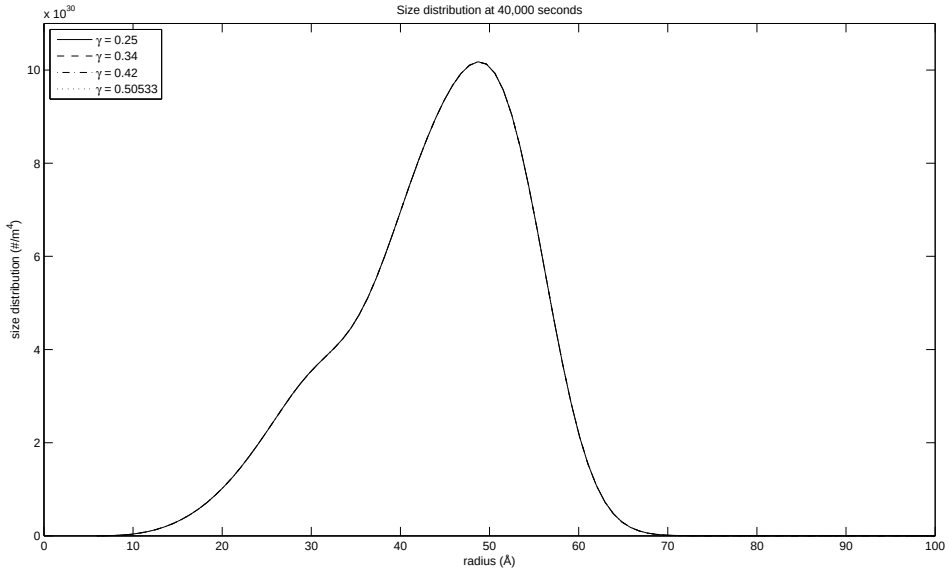

Figure 5.12: Snapshot of the size distribution ϕ at $40,000$ seconds for the chosen γ.

On inspection of the Figures 5.12 and 5.13, no significant differences between the four chosen values of γ can be determined. To this end the relative differences have been calculated with γ equal to the upper bound from Table 5.6 as reference value. This resulted in the data from Figure 5.14.

Under the assumption that significant differences only occur when a relative difference of more than five percent is present, we see that for all four values of γ we obtain the same results. This means that choosing a value for γ depends on the order preferred and the resulting amount of work. But this order is $\mathcal{O}(\Delta t^3)$ if $\gamma = \frac{1}{2} \pm \frac{1}{6}\sqrt{3}$ and $\mathcal{O}(\Delta t^2)$ otherwise. Since the two values for γ that result in third order accuracy fall outside the bounds determined, we can say that only second order accuracy in time is obtained, regardless of the chosen value for γ. The amount of work is also independent of the value of γ, which again does not influence the decision for the value of γ.

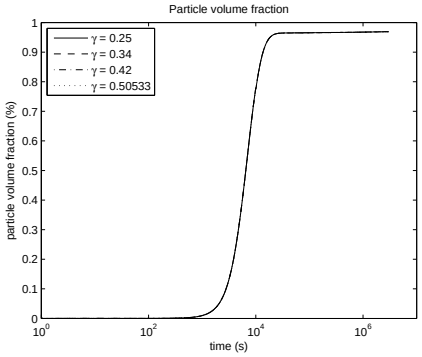

(a) Evolution of the particle volume fraction f.

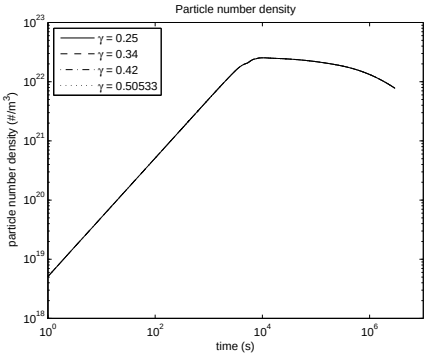

(b) Evolution of the particle number density n.

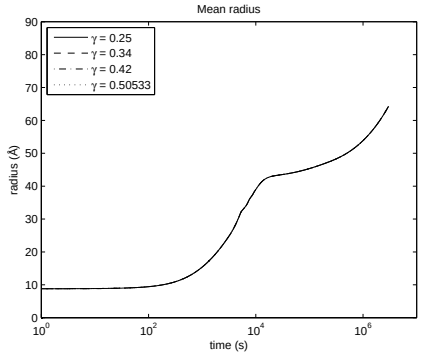

(c) Evolution of the mean particle radius $\bar{r}$.

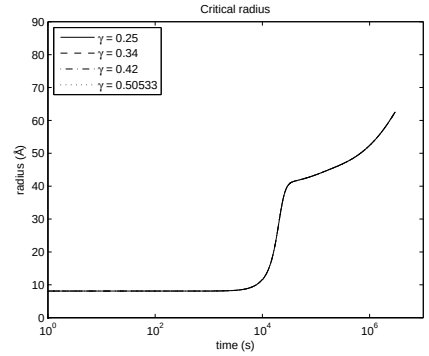

(d) Evolution of the critical particle radius r^*.

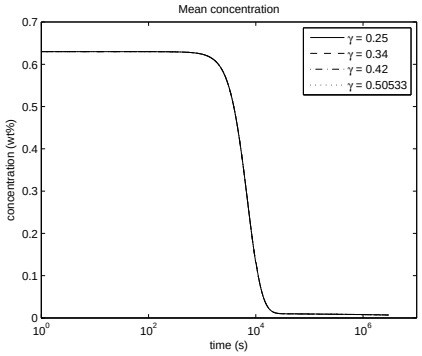

(e) Evolution of the mean concentration $\bar{C}$.

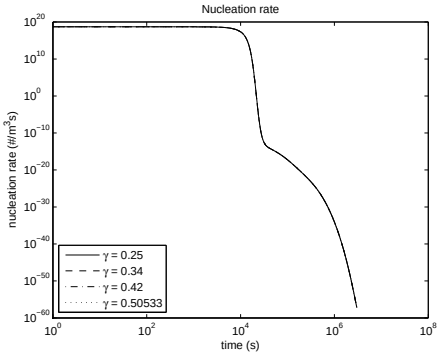

(f) Evolution of the nucleation rate j.

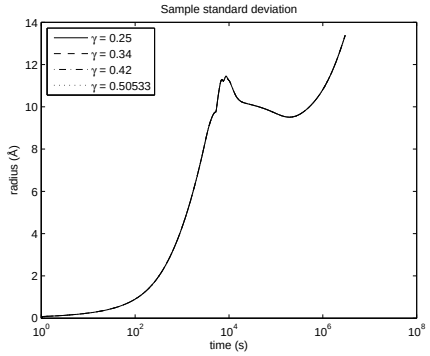

(g) Evolution of the sample standard deviation ρ of the particle radii.

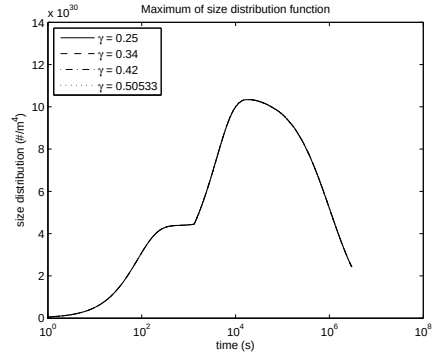

(h) Evolution of the maximum of particle size distribution function ϕ.

Figure 5.13: Results from simulation with various γ.

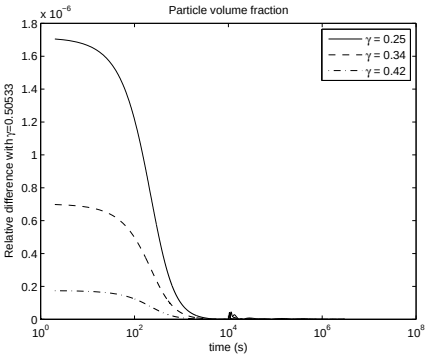

(a) Evolution of the relative particle volume fraction f.

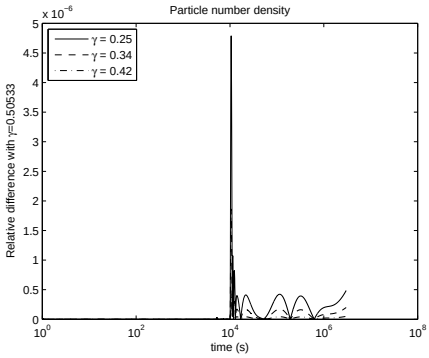

(b) Evolution of the relative particle number density n.

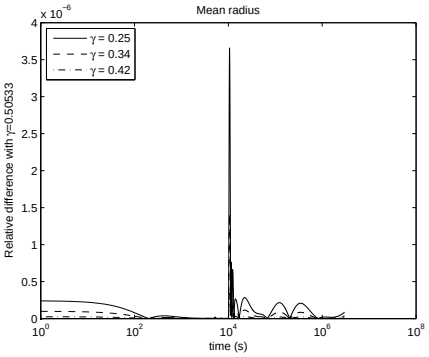

(c) Evolution of the relative mean particle radius $\bar{r}$.

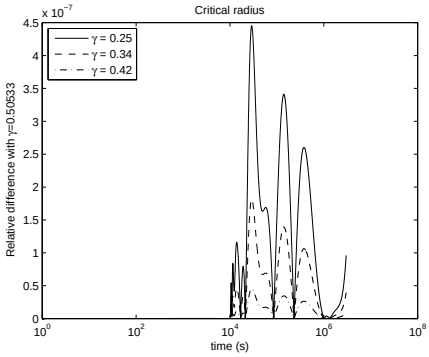

(d) Evolution of the relative critical particle radius r^*.

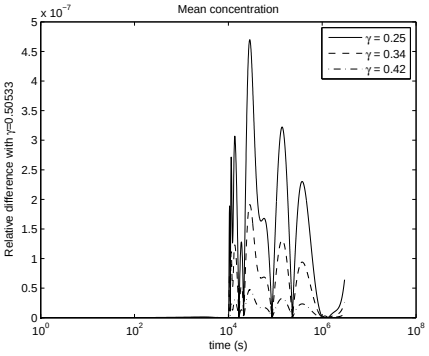

(e) Evolution of the relative mean concentration $\bar{C}$.

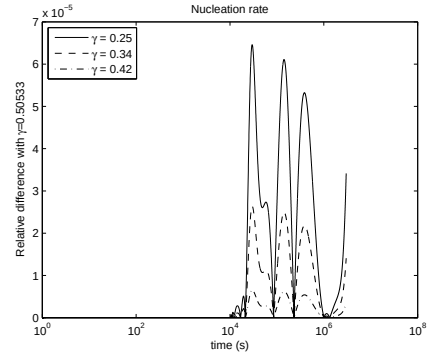

(f) Evolution of the relative nucleation rate j.

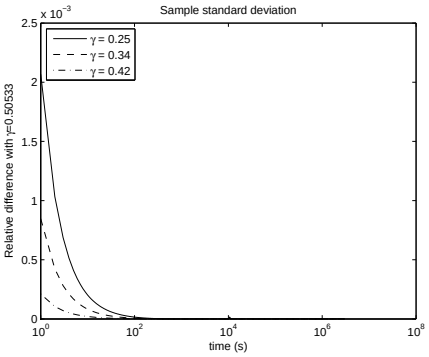

(g) Evolution of the relative sample standard deviation ρ.

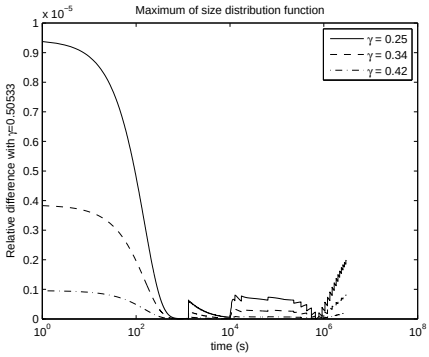

(h) Evolution of the relative maximum of size distribution function ϕ.

Figure 5.14: Relative results from simulation with various γ.

5.1.6 The second DIRK-method

This section will discuss simulations performed with the second DIRK-method for different values of γ. First the values of γ for which correct physical results can be obtained are determined. After this the results for these values are discussed.

Correct values for the second DIRK-method

Although the numerical scheme (4.2) is unconditionally stable if we choose γ above 1/4, it does not mean that the results are physically correct. Since the function N defines the number of particles with a particular radius per cubic meter, we cannot have that this function becomes negative. This means that we cannot use those γ, if any, that produce negative numbers. Using the implementation in Matlab and a heuristic approach the lower and upper bound of the region for which no negative values occur during simulation can be determined. The bounds are calculated up to 5 digits exact. The simulation used is the same as in the first simulation, see Section 5.1.2.

The simulations resulted in the bounds as in Table 5.8. Note that we have obtained the same bounds for γ as with the first DIRK-method. Figure 5.15 gives the minimum of ϕ for several γ below the lower bound and above the upper bound as a function of time. Only those time regions for which negative values occur are plotted. In the next section results will be compared between values that fall between the two bounds.

Lower bound	Upper bound
0.25000	0.50533

Table 5.8: Numerically derived lower and upper bounds for γ.

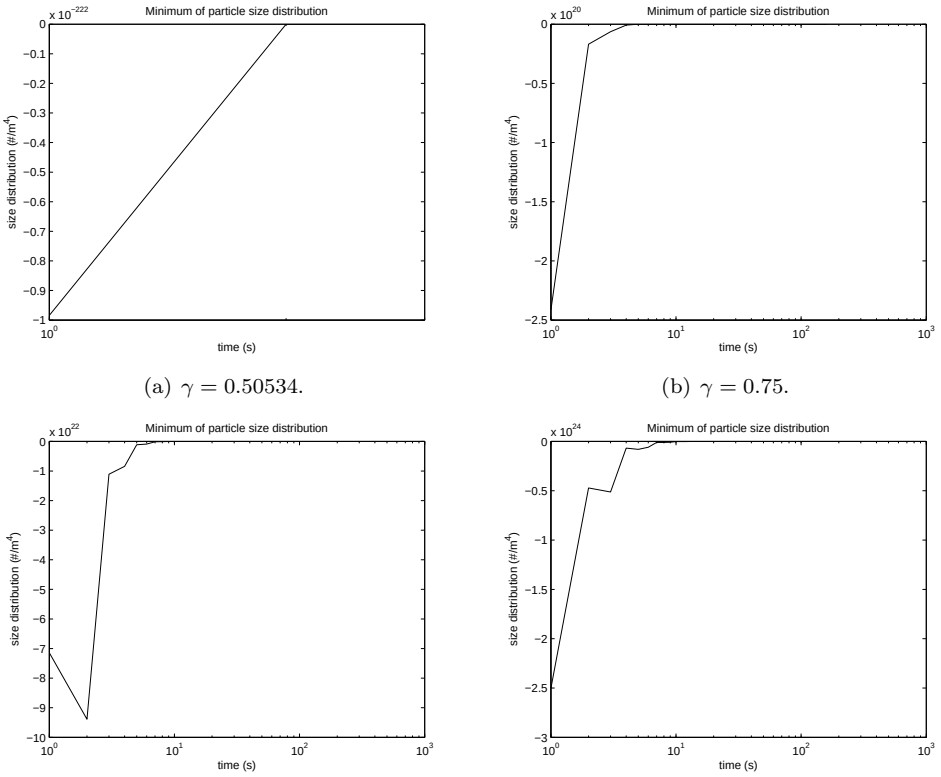

(a) $\gamma = 0.50534$.

(b) $\gamma = 0.75$.

(c) $\gamma = 1$.

(d) $\gamma = 1.25$.

Figure 5.15: Evolution of the minimum of ϕ for several θ.

Comparison of the second DIRK-method

Although the second DIRK-method is stable and provides physically correct results if γ is between the bounds from Table 5.8, differences between the results at different γ could occur. To this end four simulations have been done in the same context as in Section 5.1.2 with γ from Table 5.9. The resulting figures of these simulations can be found in Figures 5.16 and 5.17.

Simulation	γ
1	0.25
2	0.34
3	0.42
4	0.50533

Table 5.9: Values of γ for which simulations have been done.

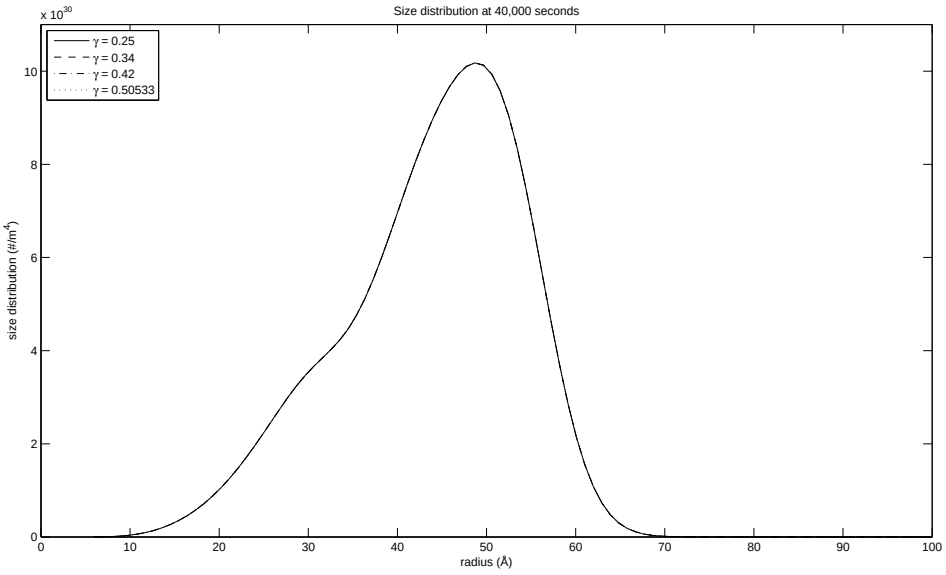

Figure 5.16: Snapshot of the size distribution ϕ at $40,000$ seconds for the chosen γ.

On inspection of the Figures 5.16 and 5.17, no significant differences between the four chosen values of γ can be determined. To this end the relative differences have been calculated with γ equal to the upper bound from Table 5.6 as reference value. This resulted in the data from Figure 5.18.

Under the assumption that significant differences only occur when a relative difference of more than five percent is present, we see that for all four values of γ we obtain the same results. This means that choosing a value for γ depends on the order preferred and the resulting amount of work. But this order is $\mathcal{O}(\Delta t^3)$ if $\gamma = \frac{1}{2} \pm \frac{1}{6}\sqrt{3}$ and $\mathcal{O}(\Delta t^2)$ otherwise. Since the two values for γ that result in third order accuracy fall outside the bounds determined, we can say that only second order accuracy in time is obtained, regardless of the chosen value for γ. The amount of work is also independent of the value of γ, which again does not influence the decision for the value of γ.

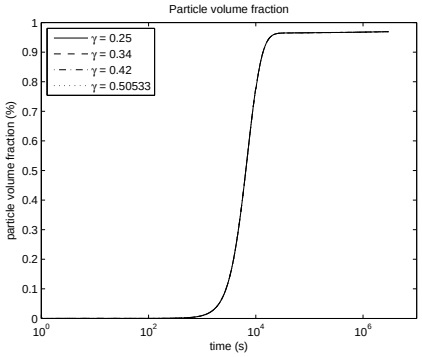

(a) Evolution of the particle volume fraction f.

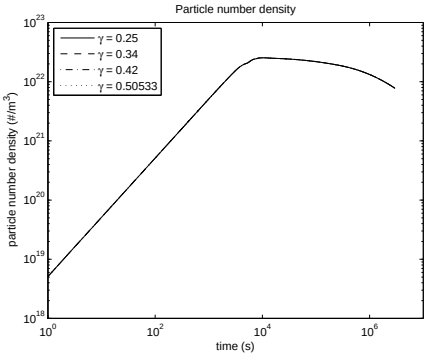

(b) Evolution of the particle number density n.

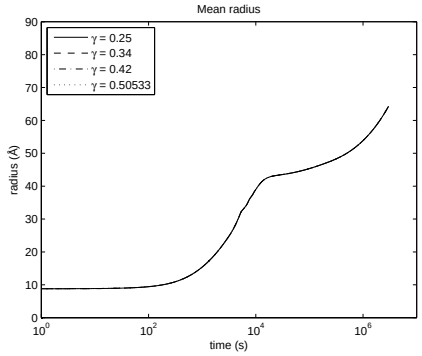

(c) Evolution of the mean particle radius $\bar{r}$.

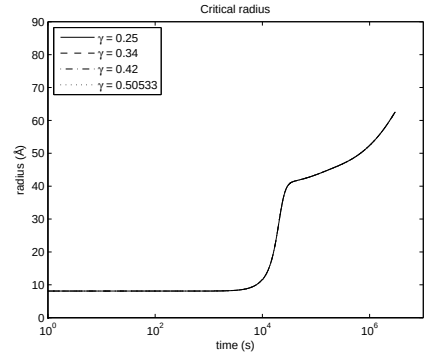

(d) Evolution of the critical particle radius r^*.

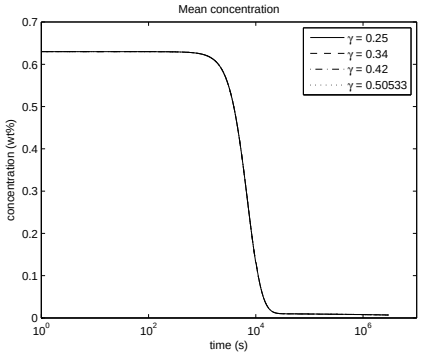

(e) Evolution of the mean concentration $\bar{C}$.

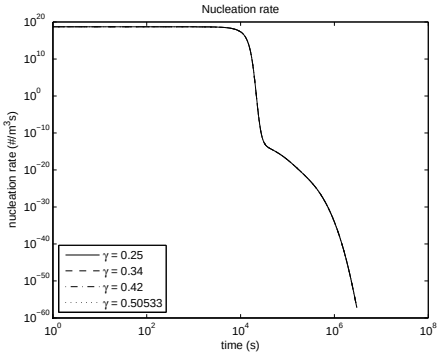

(f) Evolution of the nucleation rate j.

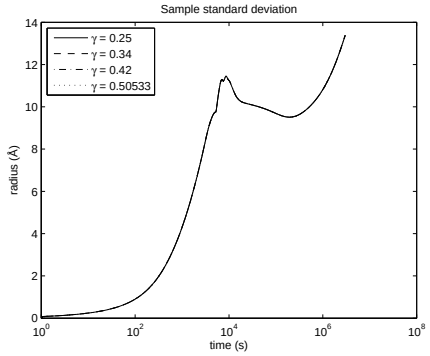

(g) Evolution of the sample standard deviation ρ of the particle radii.

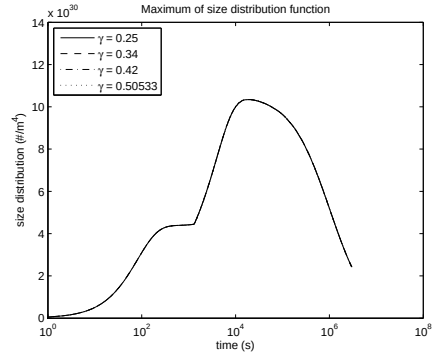

(h) Evolution of the maximum of particle size distribution function ϕ.

Figure 5.17: Results from simulation with various γ.

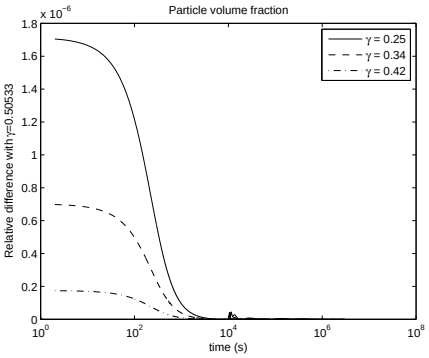

(a) Evolution of the relative particle volume fraction f.

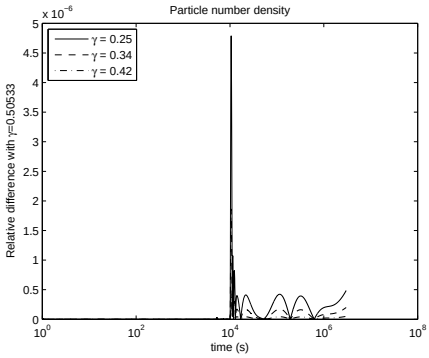

(b) Evolution of the relative particle number density n.

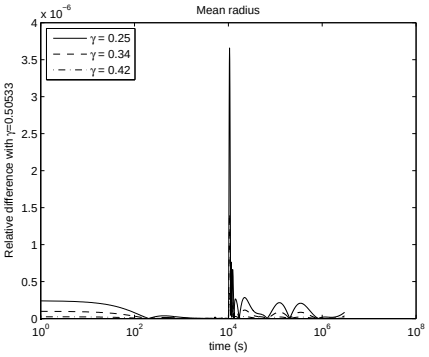

(c) Evolution of the relative mean particle radius $\bar{r}$.

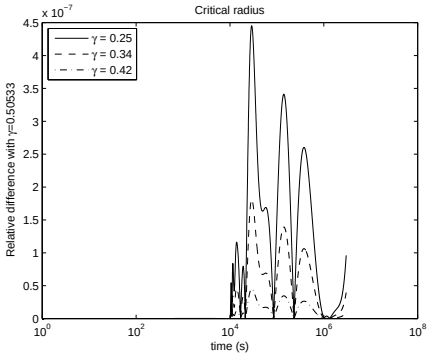

(d) Evolution of the relative critical particle radius r^*.

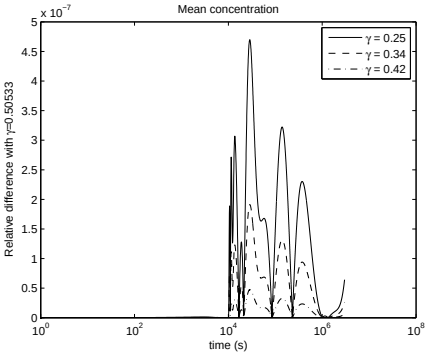

(e) Evolution of the relative mean concentration $\bar{C}$.

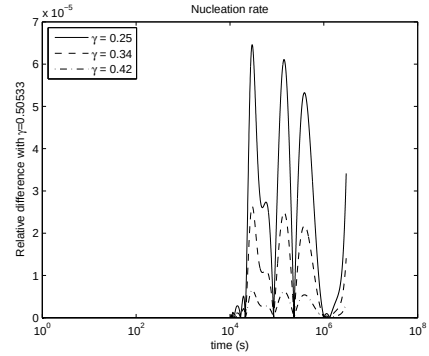

(f) Evolution of the relative nucleation rate j.

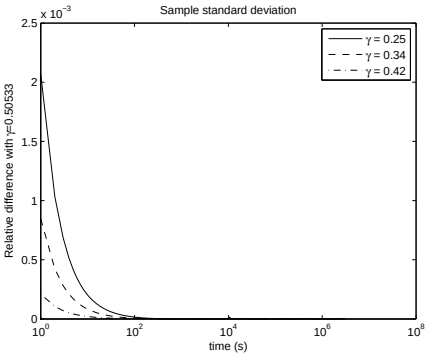

(g) Evolution of the relative sample standard deviation ρ.

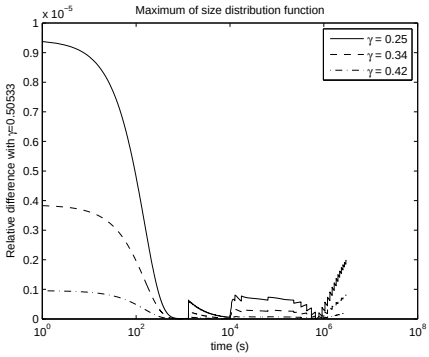

(h) Evolution of the relative maximum of size distribution function ϕ.

Figure 5.18: Relative results from simulation with various γ.

5.1.7 Comparison of time integration methods

The above sections have only discussed the results obtained with one single time integration method. Now a comparison will be made between the three time integration methods discussed in this thesis. All three methods have a parameter that influences it's behavior and complexity. For the θ-method we will choose the value $\theta = 1/2$, which leads to a second order accuracy. For both DIRK-methods we have chosen the value 0.50533 for γ, which is the upper bound for γ as derived above and leads also to second order accuracy. Table 5.10 can be used for reference for these chosen values.

	Method		
	θ-method	DIRK-method 1	DIRK-method 2
Parameter	θ	γ	γ
Value	0.5	0.50533	0.50533

Table 5.10: Parameter values for comparison of the time integration methods.

Simulations with the three methods provided the results as in Figures 5.19 and 5.20. From these results we can conclude that the θ-method and both DIRK-methods give the same size distribution function ϕ on graphical investigation. The relative differences with the θ-method are given in Figure 5.21 and back up the previous conclusion.

All three time integration methods provide physically correct results with the same order of accuracy.

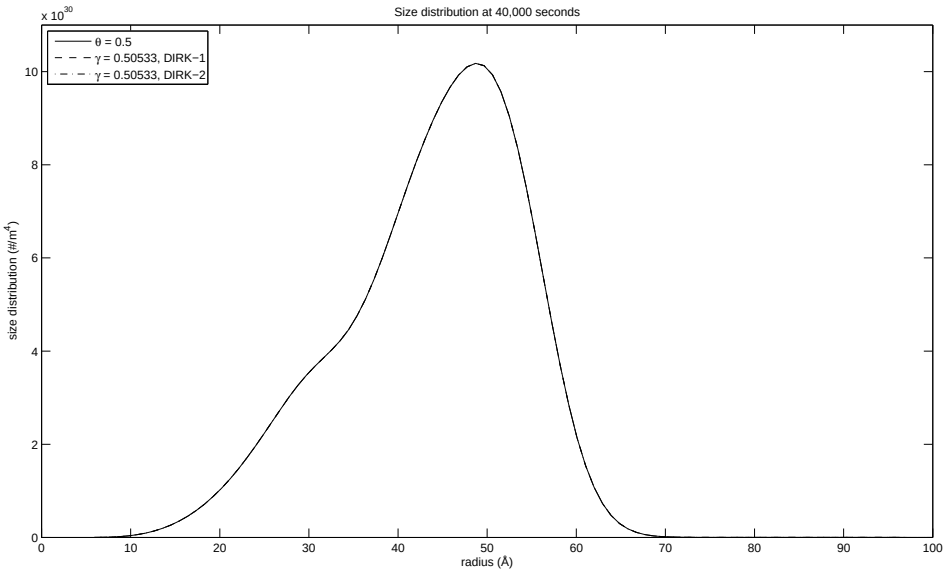

Figure 5.19: Snapshot of the size distribution ϕ at $40,000$ seconds for the chosen γ.

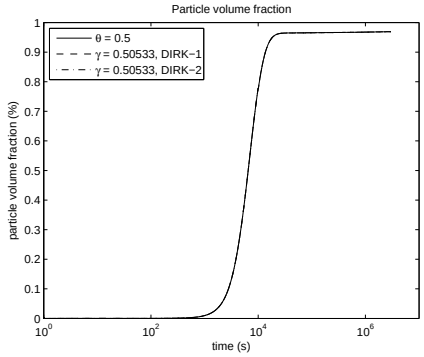

(a) Evolution of the particle volume fraction f.

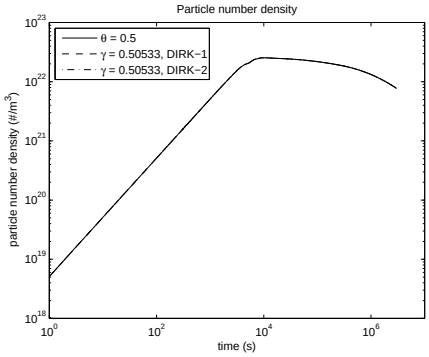

(b) Evolution of the particle number density n.

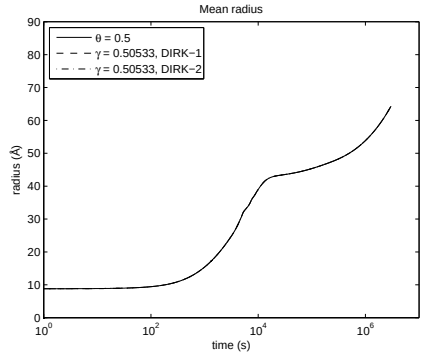

(c) Evolution of the mean particle radius $\bar{r}$.

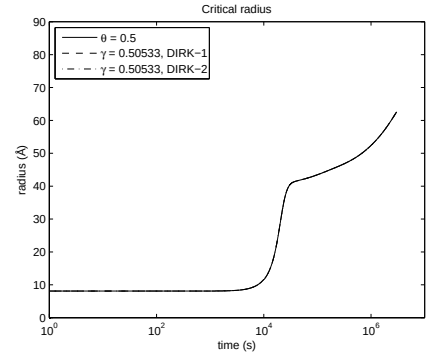

(d) Evolution of the critical particle radius r^*.

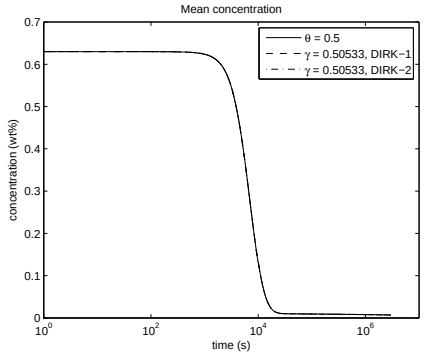

(e) Evolution of the mean concentration $\bar{C}$.

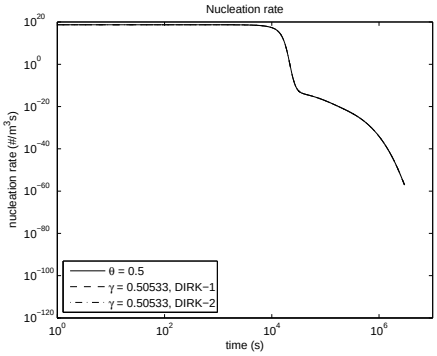

(f) Evolution of the nucleation rate j.

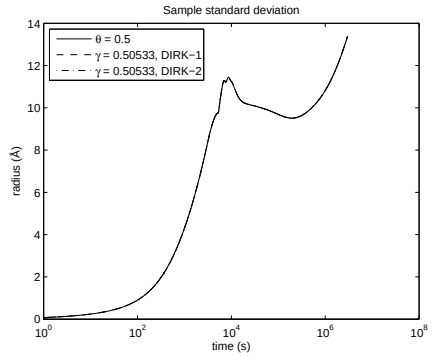

(g) Evolution of the sample standard deviation ρ of the particle radii.

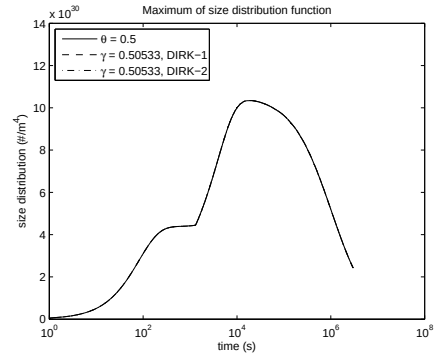

(h) Evolution of the maximum of particle size distribution function ϕ.

Figure 5.20: Results from simulation with three time integration methods.

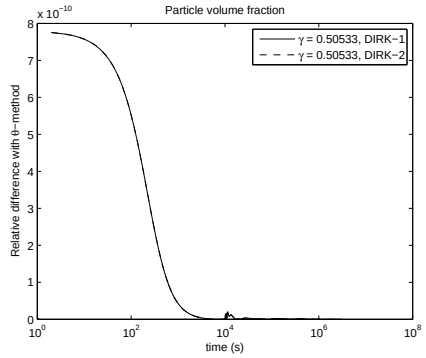

(a) Evolution of the relative particle volume fraction f.

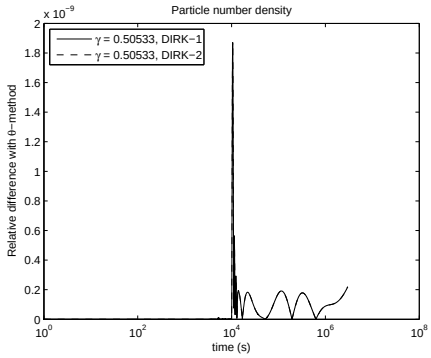

(b) Evolution of the relative particle number density n.

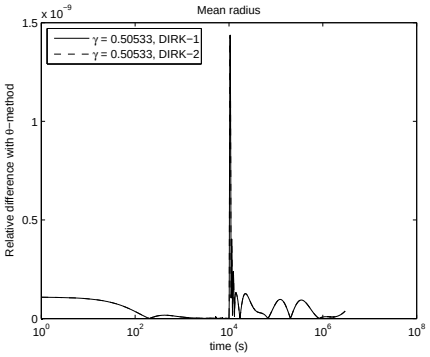

(c) Evolution of the relative mean particle radius $\bar{r}$.

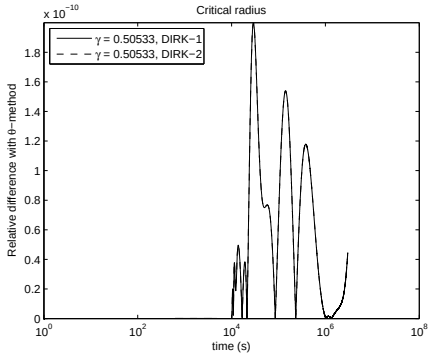

(d) Evolution of the relative critical particle radius r^*.

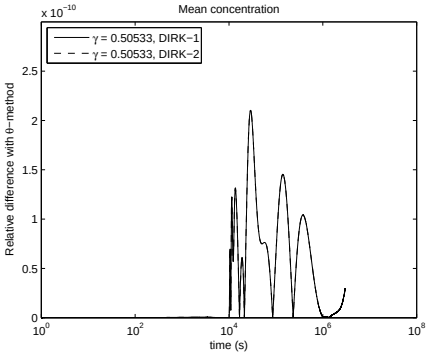

(e) Evolution of the relative mean concentration $\bar{C}$.

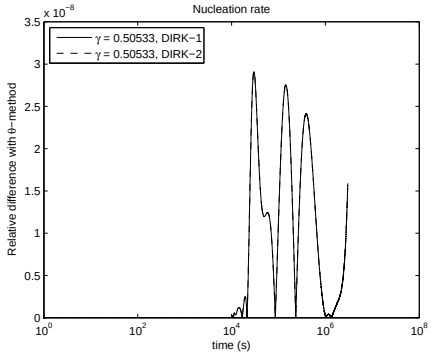

(f) Evolution of the relative nucleation rate j.

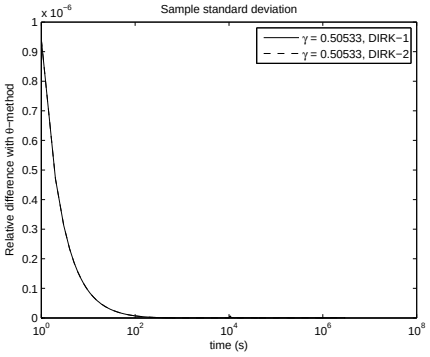

(g) Evolution of the relative sample standard deviation ρ.

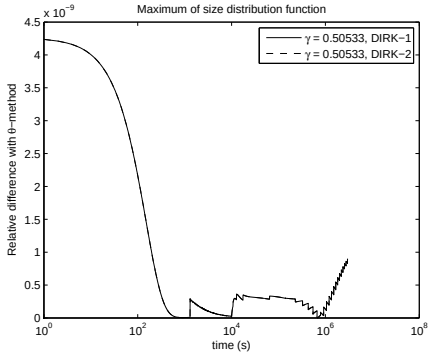

(h) Evolution of the relative maximum of size distribution function ϕ.

Figure 5.21: Relative results from simulation with three time integration methods.

Both DIRK-methods and the θ-method have a second order time error and provide the same results, but the amount of work for the methods differs. For all methods the high level computation costs are shown in Table 5.11 independent of the value of the parameters. From this table we can see that the θ-method has the lowest computation costs and the second DIRK-method the highest. This means that the θ-method is the cheapest and the preferable time integration method *if* we choose $\theta = 1/2$, since then all methods are of second order time accuracy. If only first order accuracy is wanted, the θ-method should be used with $\theta = 1$, since this reduces the computational costs with one matrix multiplication and one matrix addition.

	Operation			
Method	Vector addition	Matrix addition	Matrix multiplication	Matrix inversion
θ-method	1	2	1	1
DIRK-1	6	2	2	2
DIRK-2	9	2	3	2

Table 5.11: Computational costs for the three time integration methods per time step.

5.2 Two dimensional elastic deformations

This section will show and discuss results obtained by the implementation of the two dimensional finite element approximation of the solution of (4.3), by means of solving the system (4.6). The cases we will study will be presented at the beginning of each discussion. One remark has to be made, is that although we will choose some exterior forces in these simulations, the value of these forces do not physically mean they cause the system to obey Hooke's Law, but we will for simplicity assume it does. Incorporation of the behavior of (parts of) the block under nonelastic deformations due to external forces will be done at a later stage of this Master thesis project.

5.2.1 Gravitational model 1

The simulation performed in this section describe the steady state behavior of a plate of aluminum under basic gravitational forces, no external forces and fixed boundaries. This means that the boundary conditions are given by:

$$\boldsymbol{u} = 0 \qquad \text{on } \Gamma.$$

The plate we will investigate has width and height equal to 1 meter.

The values for all parameters used in the simulation can be found in Table 5.12. We will use a grid with 31 nodes in both the x_1 and the x_2 direction. The results of the simulation can be found in Figure 5.22. From these figures we can conclude that the influence of gravity is present in the simulated block, but only causes small deformations (Figures 5.22(c) to 5.22(f)). This is supported by the plot in Figure 5.22(b), which shows no visible differences with Figure 5.22(a).

Parameter	Value
E	70×10^9
ν	0.33
ρ_m	2700
b_1	0
b_2	$-\rho_m \cdot 9.81$

Table 5.12: Parameter values used during simulation.

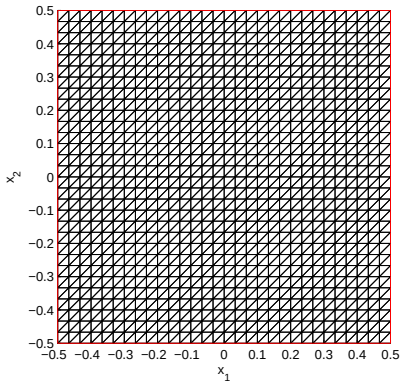

(a) Finite element mesh before deformation.

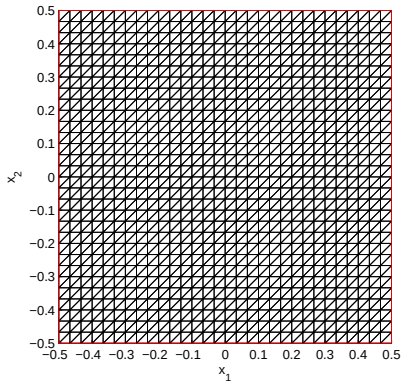

(b) Finite element mesh after deformation

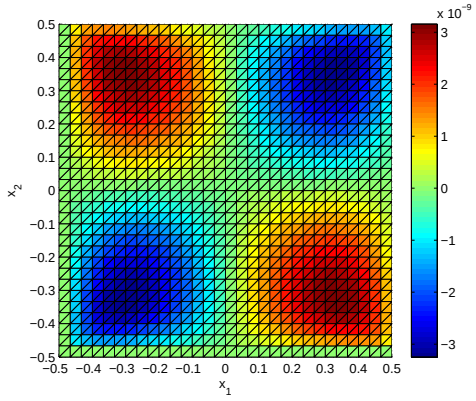

(c) Displacement u_1.

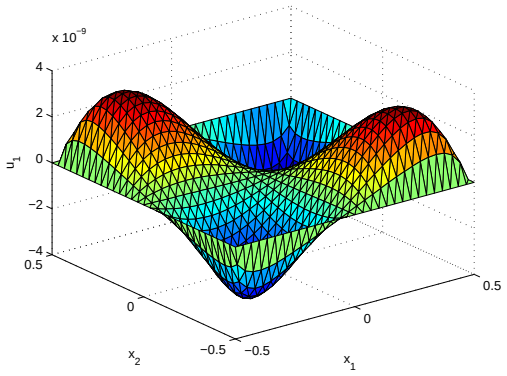

(d) Displacement u_1.

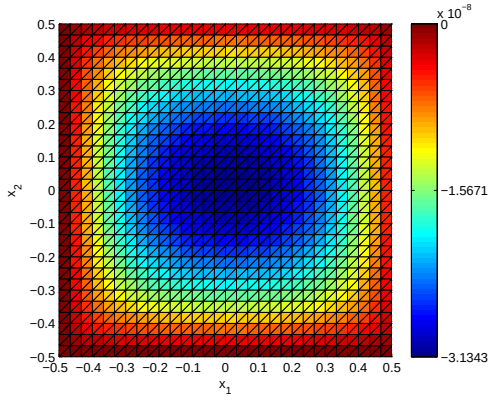

(e) Displacement u_2.

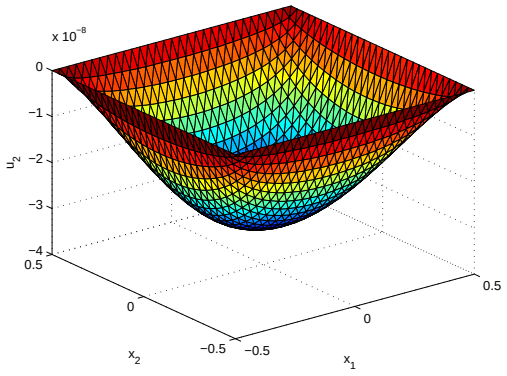

(f) Displacement u_2.

Figure 5.22: Results for gravitational model 1.

5.2.2 Gravitational model 2

The simulation performed in this section describe the steady state behavior of a plate of aluminum under basic gravitational forces, no external forces and partial fixed boundaries. We fix the left and right boundary of the plate, but let the upper and lower boundary free. This means that the boundary conditions at the left and right boundary are given by

$$\boldsymbol{u} = 0 \qquad \text{on } \Gamma_1,$$

and on the lower and upper boundary by

$$\boldsymbol{\sigma} \cdot \boldsymbol{n} = \boldsymbol{0} \qquad \text{on } \Gamma_2.$$

The plate we will investigate has width equal to 1 meter and height equal to 1 meter.

The values for all parameters used in the simulation can be found in Table 5.13. We will use a grid with 31 nodes in both the x_1 and the x_2 direction. The results of the simulation can be found in Figure 5.24.

Parameter	Value
E	70×10^9
ν	0.33
ρ_m	2700
b_1	0
b_2	$-\rho_m \cdot 9.81$

Table 5.13: Parameter values used during simulation.

From these figures we can conclude that the influence of gravity is present in the simulated block, but only causes small deformations (Figures 5.24(c) to 5.24(f)). This is supported by the plot in Figure 5.24(b), which shows no visible differences with Figure 5.24(a). If we compare with the results from Figure 5.22, we see that the displacements are an order 10 larger for u_1 and u_2. This means that setting boundaries free influences the behavior of a plate aluminum significantly.

The above conclusion that free boundaries influences the behavior of a plate aluminum can be further strengthened by running the same simulation, but now with a plate that has a height/width ratio of 0.001. Setting the width to 1 meter and the height to 1 millimeter gives the results as in Figure 5.25.

These results support indeed the previous conclusion. Note that Figure 5.25(b) shows a deformation. This visibility can be explained by the different scales of x_1 and x_2. If we set both scales to the same width, the result in Figure 5.23 is obtained. Here no significant deformation is visible.

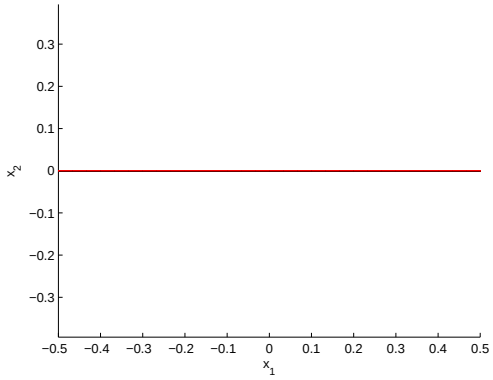

Figure 5.23: Finite element mesh after deformation, width/height ratio equals 0.001.

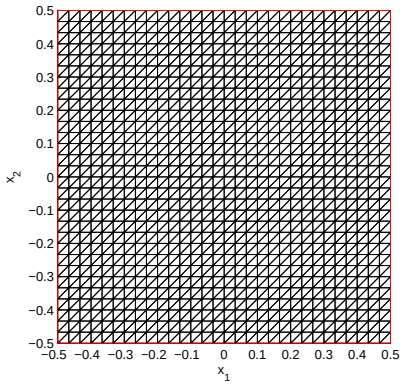

(a) Finite element mesh before deformation.

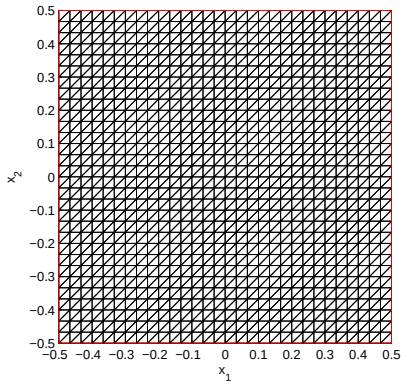

(b) Finite element mesh after deformation

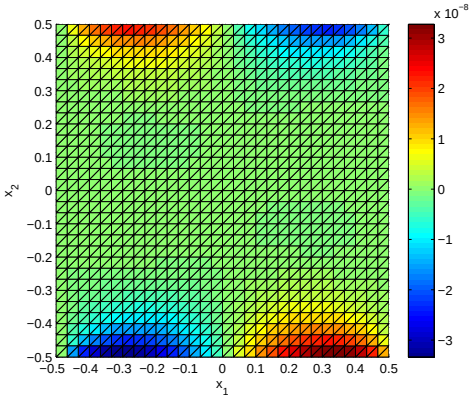

(c) Displacement u_1.

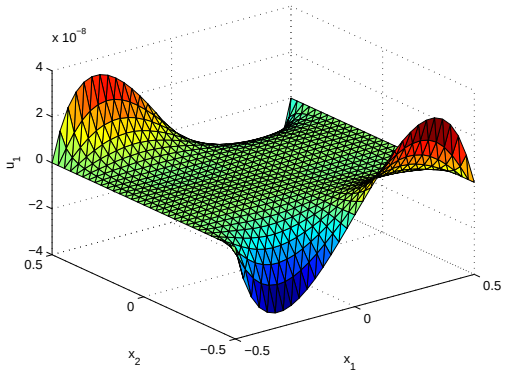

(d) Displacement u_1.

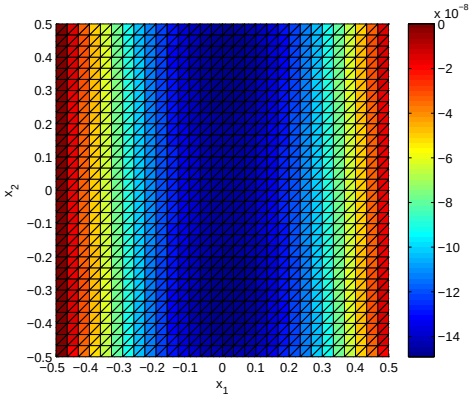

(e) Displacement u_2.

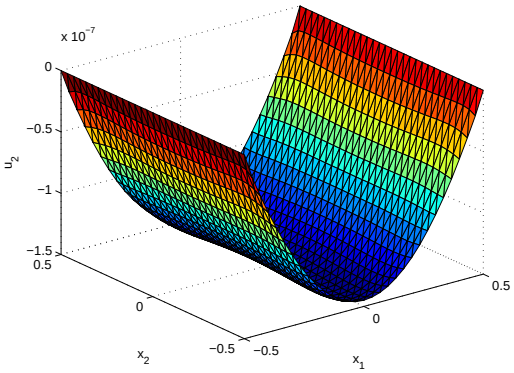

(f) Displacement u_2.

Figure 5.24: Results for gravitational model 2.

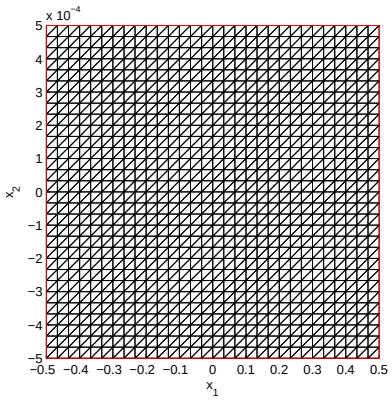

(a) Finite element mesh before deformation.

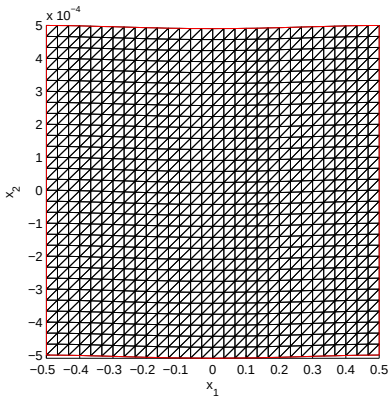

(b) Finite element mesh after deformation

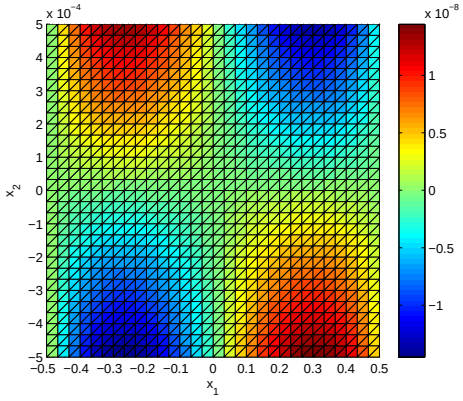

(c) Displacement u_1.

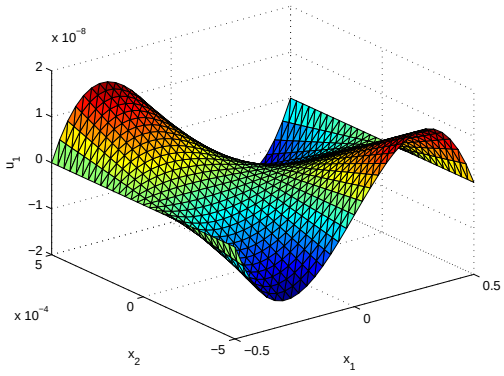

(d) Displacement u_1.

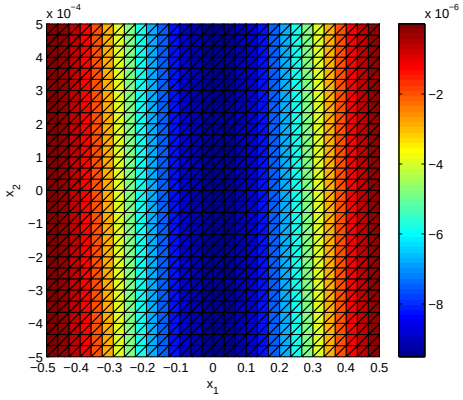

(e) Displacement u_2.

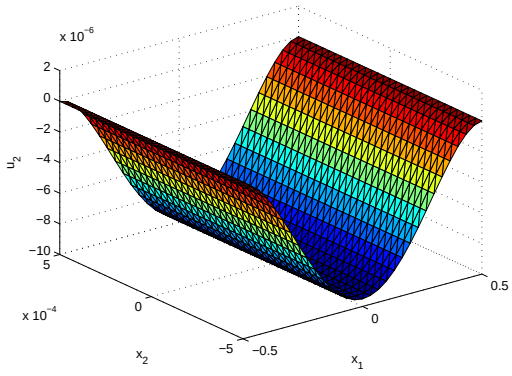

(f) Displacement u_2.

Figure 5.25: Results for gravitational model 2.

5.2.3 Normal force model 1

The simulation performed in this section describe the steady state behavior of a plate of aluminum under no gravitational forces, external forces and partial fixed boundaries. We fix the left, right and lower boundary of the plate and apply a uniform normal force on the upper boundary. This means that the boundary conditions at the left, right and lower boundary are given by

$$\boldsymbol{u} = 0 \qquad \text{on } \Gamma_1,$$

and on the upper boundary by

$$\boldsymbol{\sigma} \cdot \boldsymbol{n} = \begin{bmatrix} 0 \\ -10 \times 10^9 \end{bmatrix} \qquad \text{on } \Gamma_2.$$

The plate we will investigate has width equal to 1 meter and height equal to 1 meter.

The values for all parameters used in the simulation can be found in Table 5.14. We will use a grid with 31 nodes in both the x_1 and the x_2 direction. The results of the simulation can be found in Figure 5.26. The results show that all fixed boundaries remain fixed and only the upper boundary shows deformation. The deformation of the upper boundary is also visible throughout the entire interior of the plate.

Parameter	Value
E	70×10^9
ν	0.33
ρ_m	2700
b_1	0
b_2	0

Table 5.14: Parameter values used during simulation.

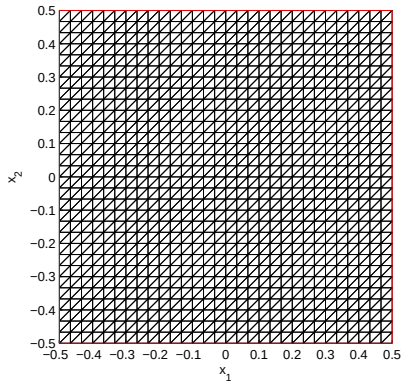

(a) Finite element mesh before deformation.

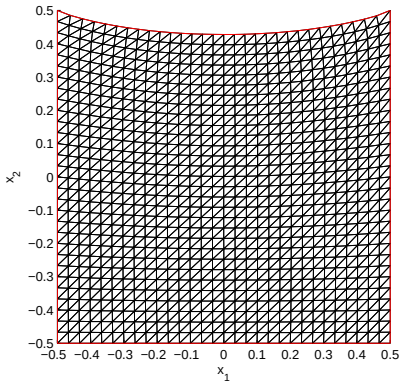

(b) Finite element mesh after deformation

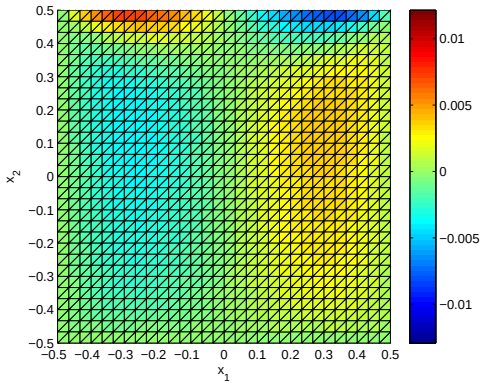

(c) Displacement u_1.

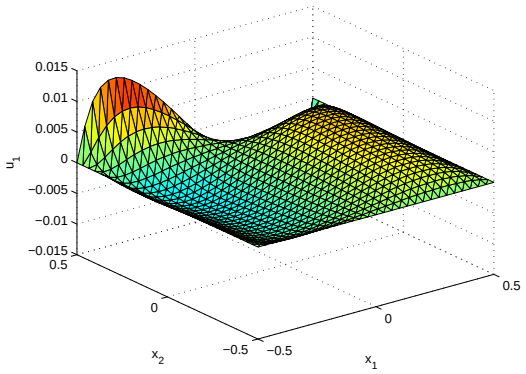

(d) Displacement u_1.

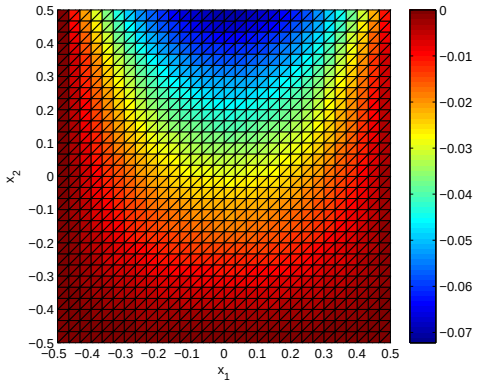

(e) Displacement u_2.

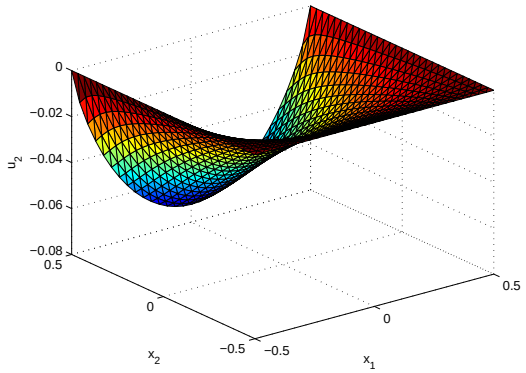

(f) Displacement u_2.

Figure 5.26: Results for uniform normal force model 1.

5.2.4 Normal force model 2

The simulation performed in this section describe the steady state behavior of a plate of aluminum under no gravitational forces, external forces and partial fixed boundaries. We fix only the lower boundary of the plate and apply a uniform normal force on the upper boundary. This means that the boundary conditions at the lower boundary is given by

$$\boldsymbol{u} = 0 \qquad \text{on } \Gamma_1,$$

on the right and left boundary by

$$\boldsymbol{\sigma} \cdot \boldsymbol{n} = 0 \qquad \text{on } \Gamma_2,$$

and on the upper boundary by

$$\boldsymbol{\sigma} \cdot \boldsymbol{n} = \begin{bmatrix} 0 \\ -10 \times 10^9 \end{bmatrix} \qquad \text{on } \Gamma_3.$$

The plate we will investigate has width equal to 1 meter and height equal to 1 meter.

The values for all parameters used in the simulation can be found in Table 5.15. We will use a grid with 31 nodes in both the x_1 and the x_2 direction. The results of the simulation can be found in Figure 5.27. The results show that all fixed boundaries remain fixed and all other boundaries show deformations. The deformation of the upper boundary is also visible throughout the entire interior of the plate.

Parameter	Value
E	70×10^9
ν	0.33
ρ_m	2700
b_1	0
b_2	0

Table 5.15: Parameter values used during simulation.

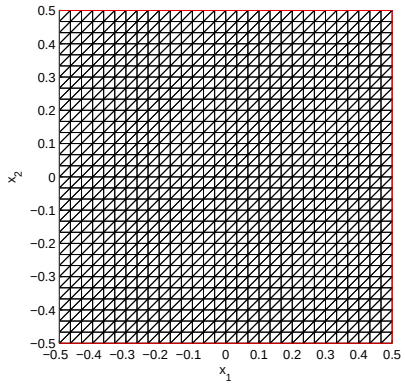

(a) Finite element mesh before deformation.

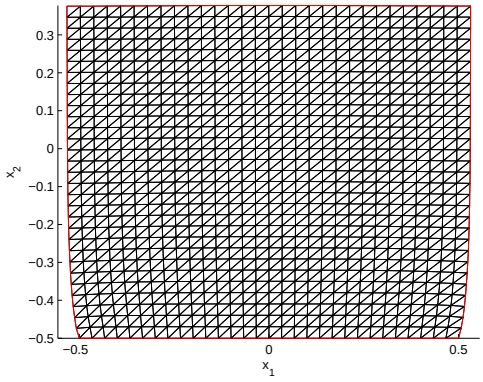

(b) Finite element mesh after deformation

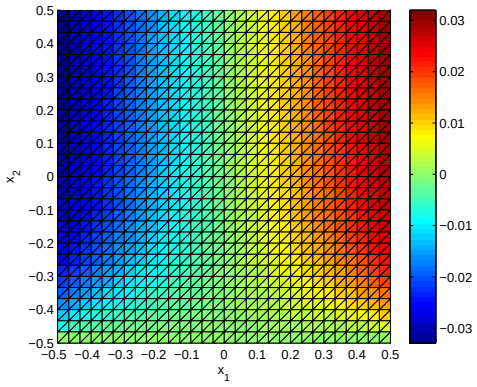

(c) Displacement u_1.

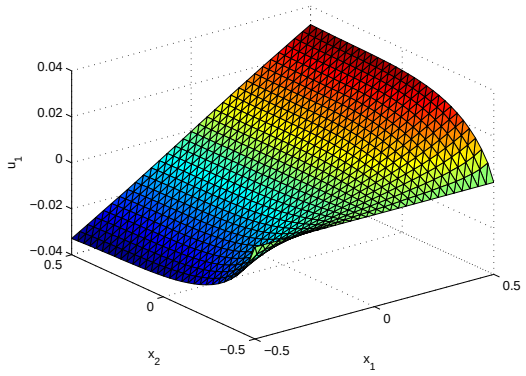

(d) Displacement u_1.

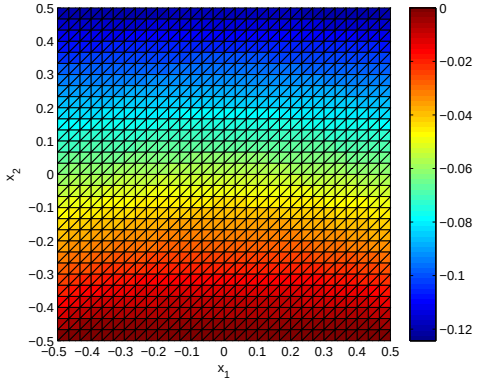

(e) Displacement u_2.

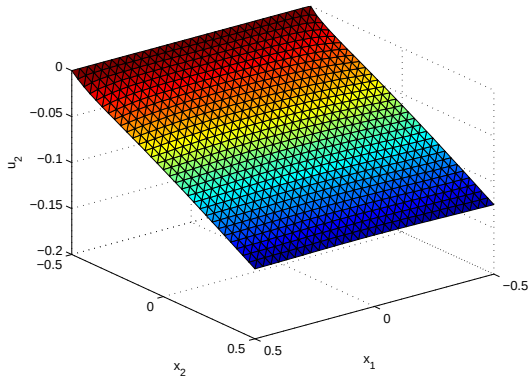

(f) Displacement u_2.

Figure 5.27: Results for uniform normal force model 2.

5.2.5 Normal point force model 1

The simulation performed in this section describe the steady state behavior of a plate of aluminum under no gravitational forces, external forces and partial fixed boundaries. We fix the left, right and lower boundary of the plate and apply a point normal force on the upper boundary at $x_1 = 0$ and further a free upper boundary. This means that the boundary conditions at the left, right and lower boundary are given by

$$\boldsymbol{u} = 0 \qquad \text{on } \Gamma_1,$$

on the upper boundary at $x_1 = 0$ by

$$\boldsymbol{\sigma} \cdot \boldsymbol{n} = \begin{bmatrix} 0 \\ -10 \times 10^9 \end{bmatrix} \qquad \text{on } \Gamma_2,$$

and on the remainder of the upper boundary by

$$\boldsymbol{\sigma} \cdot \boldsymbol{n} = 0 \qquad \text{on } \Gamma_3.$$

The plate we will investigate has width equal to 1 meter and height equal to 1 meter.

The values for all parameters used in the simulation can be found in Table 5.16. We will use a grid with 31 nodes in both the x_1 and the x_2 direction. The results of the simulation can be found in Figure 5.28. The results show that all fixed boundaries remain fixed and only the upper boundary shows deformation. The deformation of the upper boundary is also visible throughout the entire interior of the plate.

Parameter	Value
E	70×10^9
ν	0.33
ρ_m	2700
b_1	0
b_2	0

Table 5.16: Parameter values used during simulation.

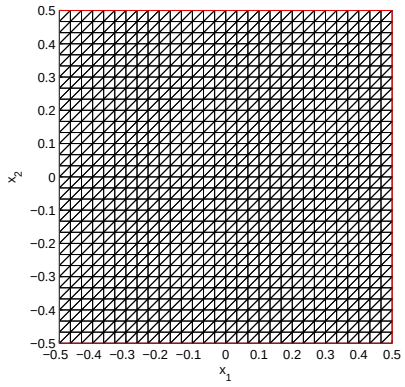

(a) Finite element mesh before deformation.

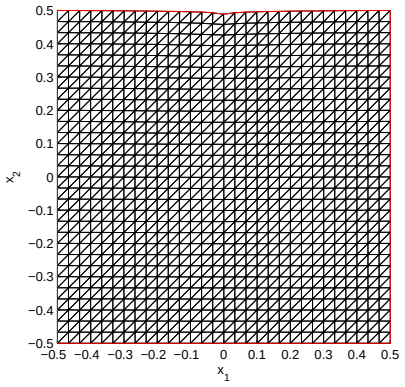

(b) Finite element mesh after deformation.

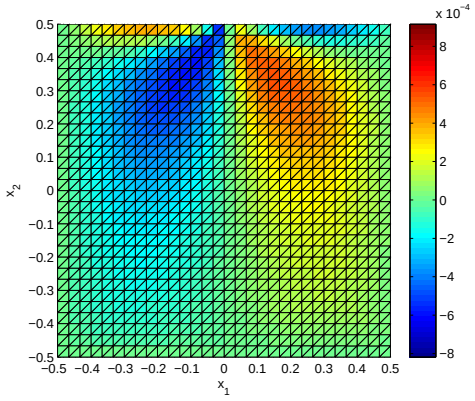

(c) Displacement u_1.

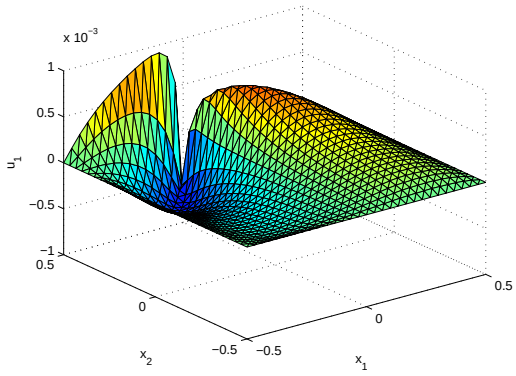

(d) Displacement u_1.

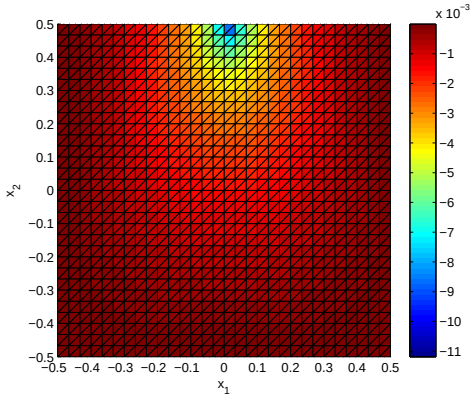

(e) Displacement u_2.

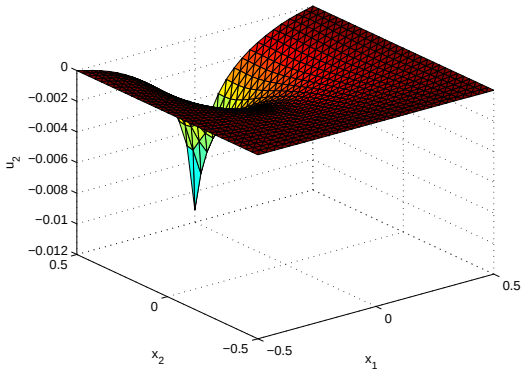

(f) Displacement u_2.

Figure 5.28: Results for normal point force model 1.

5.2.6 Normal point force model 2

The simulation performed in this section describe the steady state behavior of a plate of aluminum under no gravitational forces, external forces and partial fixed boundaries. We fix only the lower boundary of the plate and apply a normal point force on the upper boundary. This means that the boundary conditions at the lower boundary is given by

$$\boldsymbol{u} = 0 \qquad \text{on } \Gamma_1,$$

on the upper boundary at $x_1 = 0$ by

$$\boldsymbol{\sigma} \cdot \boldsymbol{n} = \begin{bmatrix} 0 \\ -10 \times 10^9 \end{bmatrix} \qquad \text{on } \Gamma_2,$$

and on the right, left and the remainder of the upper boundary by

$$\boldsymbol{\sigma} \cdot \boldsymbol{n} = 0 \qquad \text{on } \Gamma_3.$$

The plate we will investigate has width equal to 1 meter and height equal to 1 meter.

The values for all parameters used in the simulation can be found in Table 5.17. We will use a grid with 31 nodes in both the x_1 and the x_2 direction. The results of the simulation can be found in Figure 5.29. The results show that all fixed boundaries remain fixed and only the upper boundary shows deformation. The deformation of the upper boundary is also visible throughout the entire interior of the plate.

Parameter	Value
E	70×10^9
ν	0.33
ρ_m	2700
b_1	0
b_2	0

Table 5.17: Parameter values used during simulation.

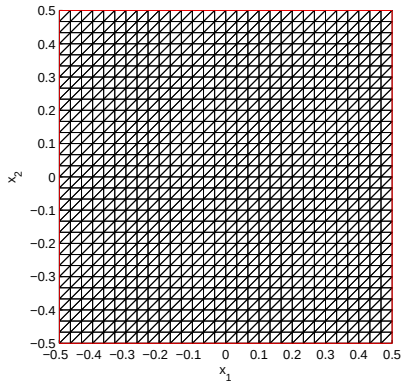

(a) Finite element mesh before deformation.

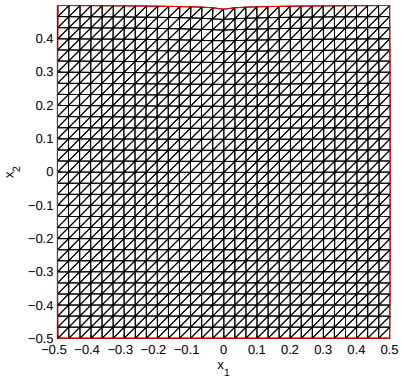

(b) Finite element mesh after deformation.

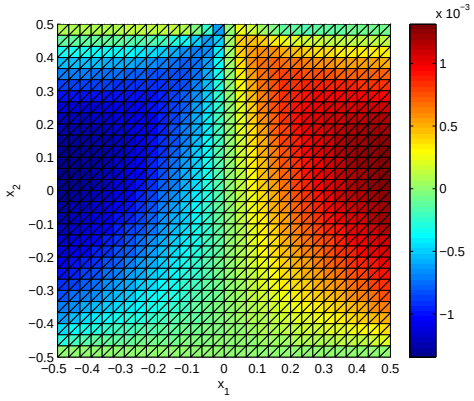

(c) Displacement u_1.

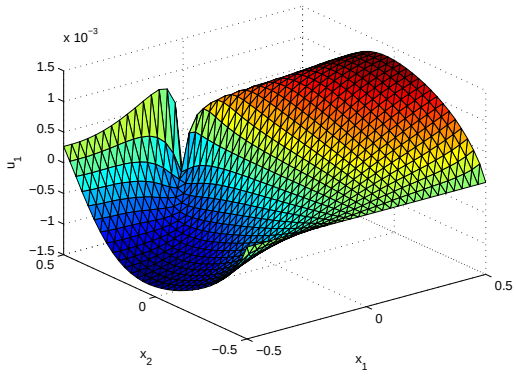

(d) Displacement u_1.

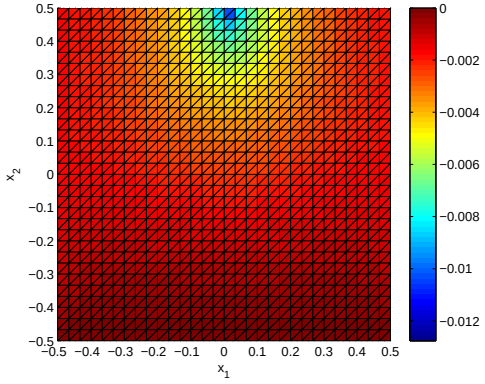

(e) Displacement u_2.

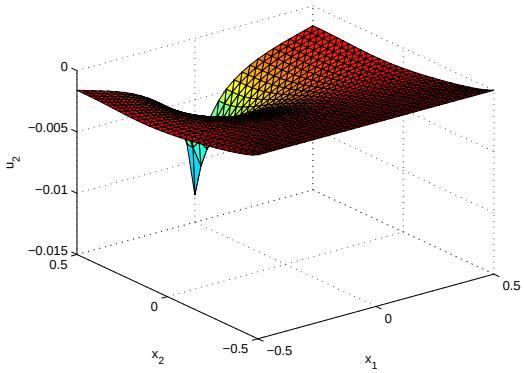

(f) Displacement u_2.

Figure 5.29: Results for normal point force model 2.

5.2.7 Shear force model 1

The simulation performed in this section describe the steady state behavior of a plate of aluminum under no gravitational forces, external forces and partial fixed boundaries. We fix the left, right and lower boundary of the plate and apply a uniform shear force on the upper boundary to the right and further a free upper boundary. This means that the boundary conditions at the left, right and lower boundary are given by

$$\boldsymbol{u} = 0 \qquad \text{on } \Gamma_1,$$

and on the upper boundary by

$$\boldsymbol{\sigma} \cdot \boldsymbol{n} = \begin{bmatrix} 10 \times 10^9 \\ 0 \end{bmatrix} \qquad \text{on } \Gamma_2.$$

The plate we will investigate has width equal to 1 meter and height equal to 1 meter.

The values for all parameters used in the simulation can be found in Table 5.18. We will use a grid with 31 nodes in both the x_1 and the x_2 direction. The results of the simulation can be found in Figure 5.30. The results show that all fixed boundaries remain fixed and only the upper boundary shows deformation. The deformation of the upper boundary is also visible throughout the entire interior of the plate.

Parameter	Value
E	70×10^9
ν	0.33
ρ_m	2700
b_1	0
b_2	0

Table 5.18: Parameter values used during simulation.

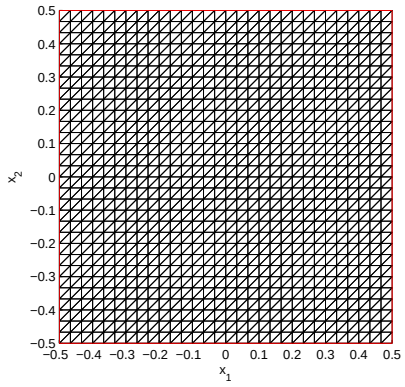

(a) Finite element mesh before deformation.

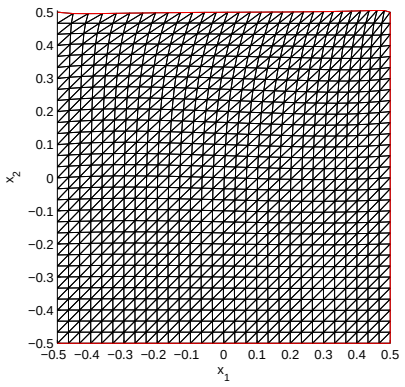

(b) Finite element mesh after deformation.

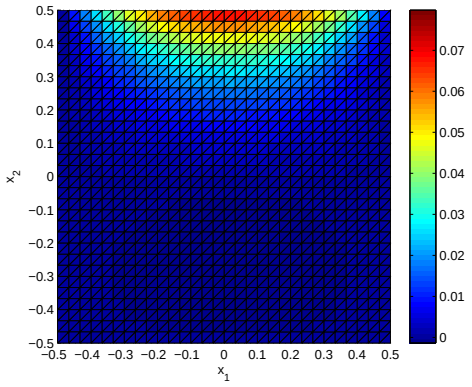

(c) Displacement u_1.

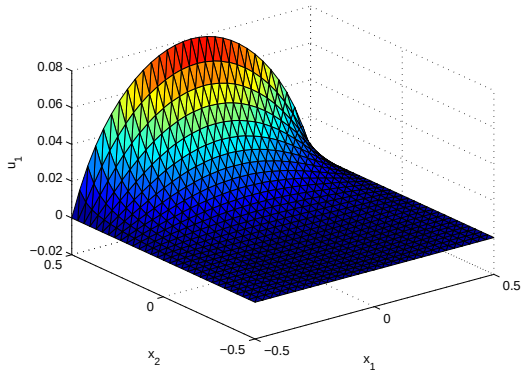

(d) Displacement u_1.

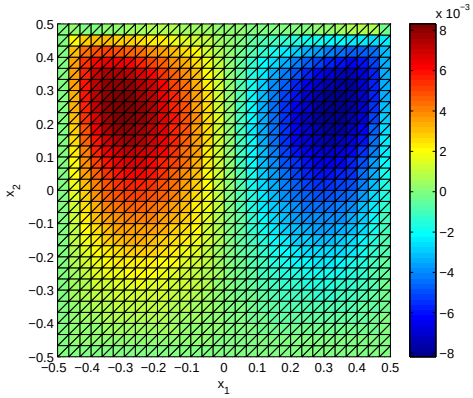

(e) Displacement u_2.

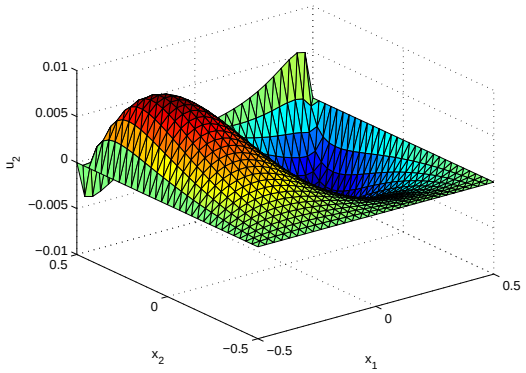

(f) Displacement u_2.

Figure 5.30: Results for shear force model 1.

5.2.8 Shear force model 2

The simulation performed in this section describe the steady state behavior of a plate of aluminum under no gravitational forces, external forces and partial fixed boundaries. We fix the left, right and lower boundary of the plate and apply a uniform shear force on the upper boundary to the right and further a free upper boundary. This means that the boundary condition at lower boundary is given by

$$\boldsymbol{u} = 0 \qquad \text{on } \Gamma_1,$$

on the upper boundary by

$$\boldsymbol{\sigma} \cdot \boldsymbol{n} = \begin{bmatrix} 1 \times 10^9 \\ 0 \end{bmatrix} \qquad \text{on } \Gamma_2,$$

and on the left and right boundary by

$$\boldsymbol{\sigma} \cdot \boldsymbol{n} = \begin{bmatrix} 1 \times 10^9 \\ 0 \end{bmatrix} \qquad \text{on } \Gamma_3.$$

The plate we will investigate has width equal to 1 meter and height equal to 1 meter.

The values for all parameters used in the simulation can be found in Table 5.19. We will use a grid with 31 nodes in both the x_1 and the x_2 direction. The results of the simulation can be found in Figure 5.31. The results show that all fixed boundaries remain fixed and only the upper boundary shows deformation. The deformation of the upper boundary is also visible throughout the entire interior of the plate.

Parameter	Value
E	70×10^9
ν	0.33
ρ_m	2700
b_1	0
b_2	0

Table 5.19: Parameter values used during simulation.

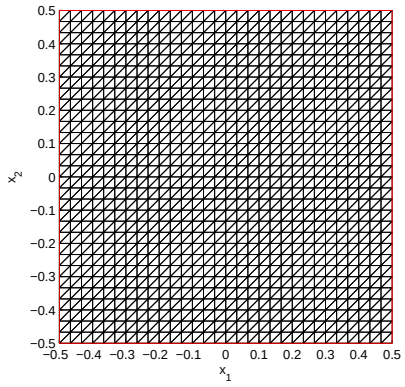

(a) Finite element mesh before deformation.

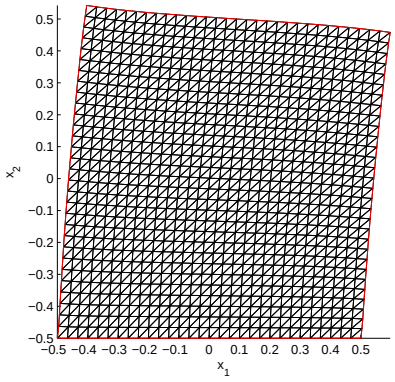

(b) Finite element mesh after deformation.

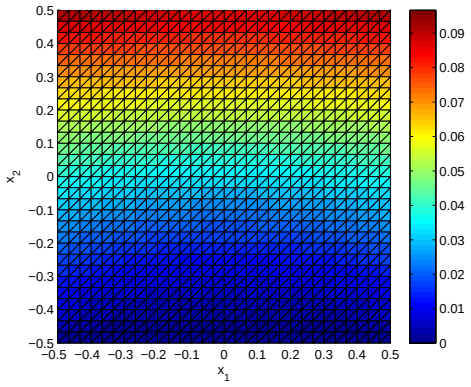

(c) Displacement u_1.

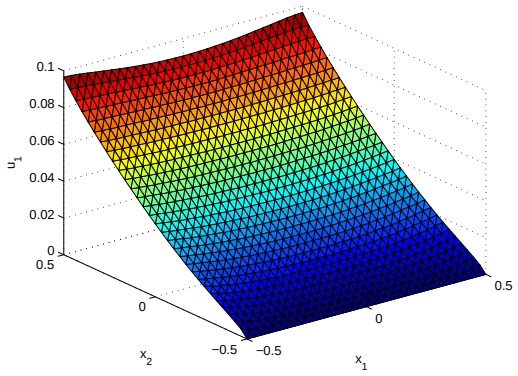

(d) Displacement u_1.

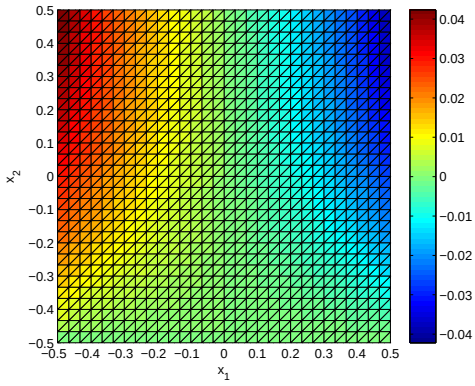

(e) Displacement u_2.

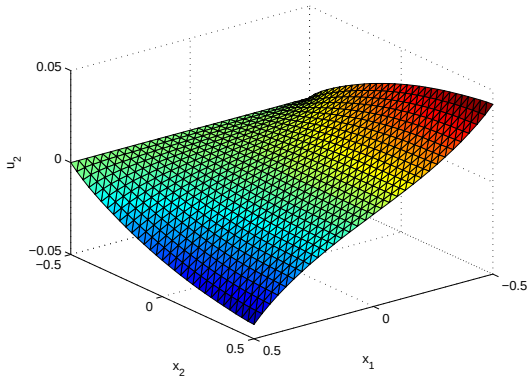

(f) Displacement u_2.

Figure 5.31: Results for shear force model 2.

5.3 Three dimensional elastic deformations

This section will show and discuss results obtained by the implementation of the two dimensional finite element approximation of the solution of (3.14), by means of solving the system (4.9). The cases we will study will be presented at the beginning of each discussion.

5.3.1 Finite element grid

The grid we will use in the simulations of this section will be based on the splitting of a cuboid into 6 tetrahedra. The entire domain of interest will be divided into cuboid which will then be devided into six tetrahedra. The division of a cuboid in to 6 tetrahedra can be seen in Figure 5.32 and Table 5.20. If cuboids of the same dimensions are joint, all green lines will land on green lines, as will red on red and blue on blue. This means that consistency of the overall mesh is guaranteed.

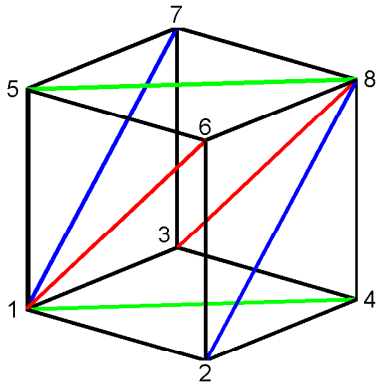

Figure 5.32: Topology of used mesh.

Tetrahedron	Points			
A	1	2	4	8
B	1	2	6	8
C	1	5	6	8
D	1	3	4	8
E	1	3	7	8
F	1	5	7	8

Table 5.20: Topology of used mesh.

5.3.2 Normal force model 1

The simulation performed in this section describe the steady state behavior of a block of aluminum under no gravitational forces, external forces and partial fixed boundaries. We fix all boundaries except the top boundary of the block and apply a uniform normal force on the top boundary. This means that the boundary conditions on the top boundary is given by

$$\boldsymbol{\sigma} \cdot \boldsymbol{n} = \begin{bmatrix} 0 \\ -10 \times 10^9 \end{bmatrix} \qquad \text{on } \Gamma_1,$$

and on all other boundaries by

$$\boldsymbol{u} = 0 \qquad \text{on } \Gamma_2.$$

The block we will investigate has width, height and depth equal to 1 meter.

The values for all parameters used in the simulation can be found in Table 5.21. We will use a grid with 21 nodes in both the x_1-, x_2- and the x_3-direction. The results of the simulation can be found in Figures 5.33 and 5.34. The results show that all fixed boundaries remain fixed and only the upper boundary shows deformation. The deformation of the upper boundary is also visible throughout the entire interior of the plate.

Parameter	Value
E	70×10^9
ν	0.33
ρ_m	2700
b_1	0
b_2	0
b_3	0

Table 5.21: Parameter values used during simulation.

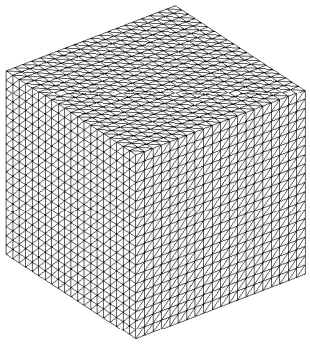

(a) Finite element mesh before deformation.

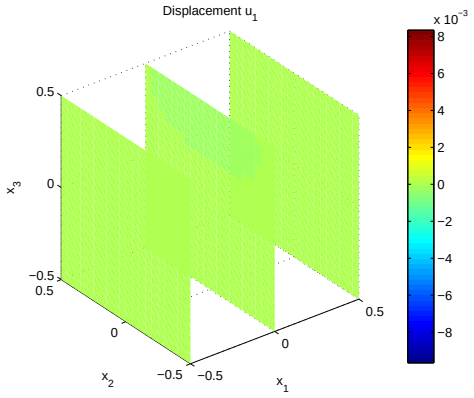

(b) Displacement u_1.

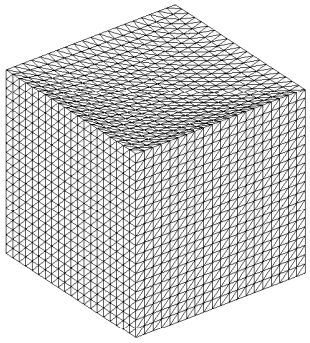

(c) Finite element mesh after deformation

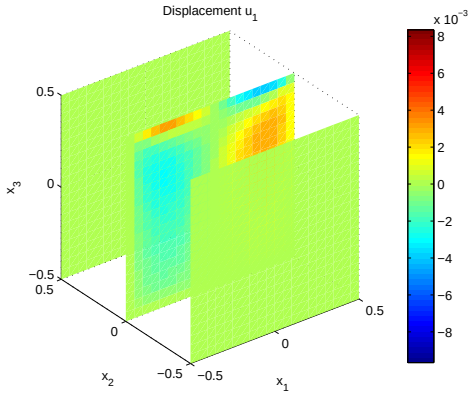

(d) Displacement u_1.

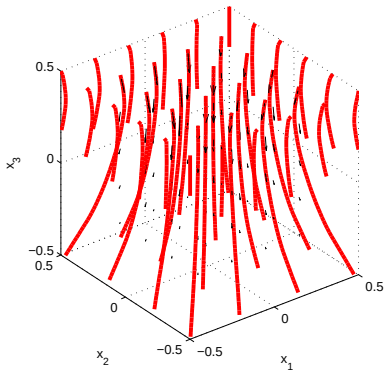

(e) Displacement vector field.

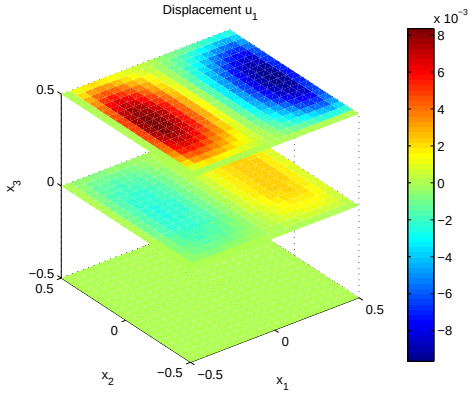

(f) Displacement u_1.

Figure 5.33: Results for uniform normal force model 1.

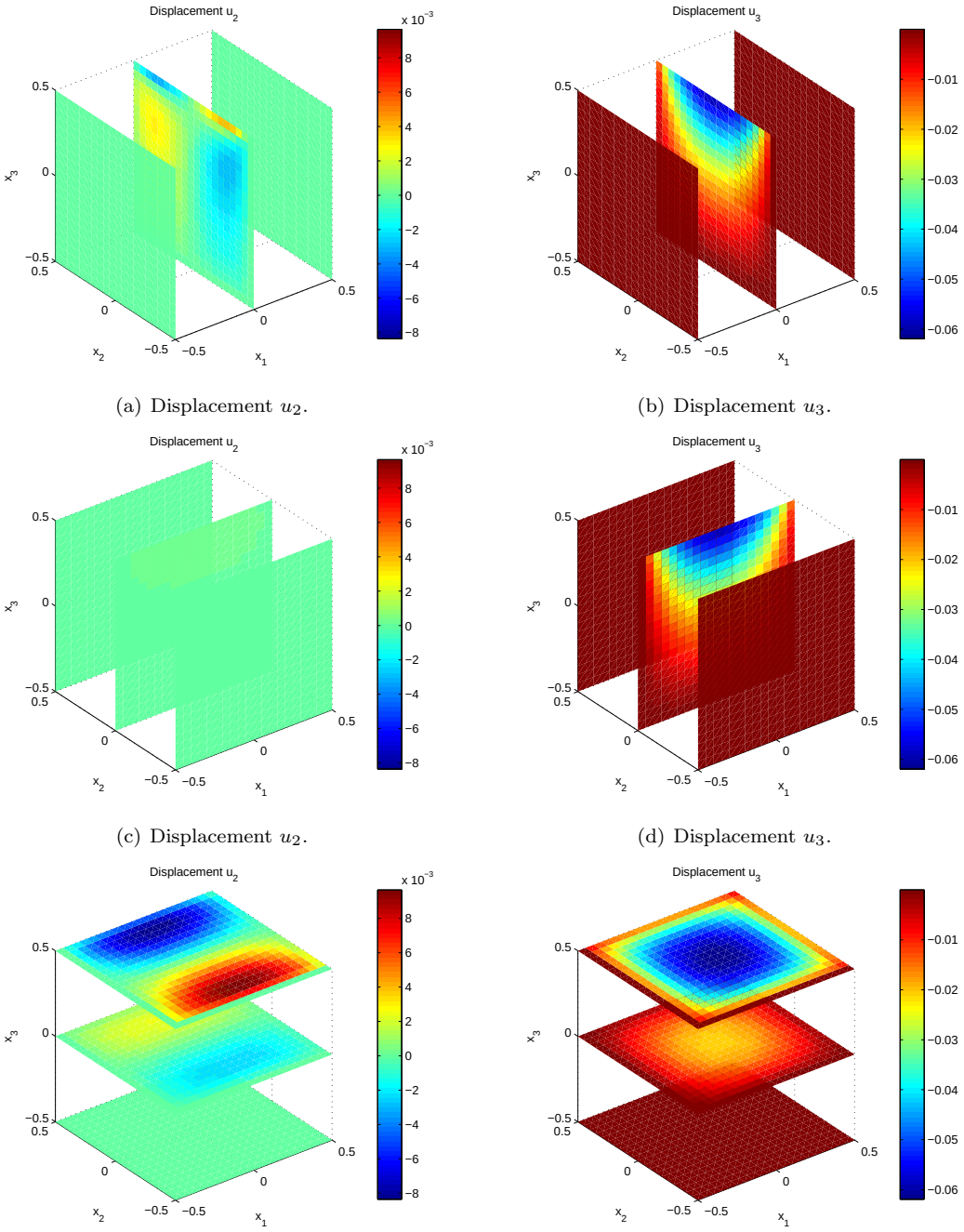

(a) Displacement u_2.

(b) Displacement u_3.

(c) Displacement u_2.

(d) Displacement u_3.

(e) Displacement u_2.

(f) Displacement u_3.

Figure 5.34: Results for uniform normal force model 1.

5.3.3 Normal force model 2

The simulation performed in this section describe the steady state behavior of a block of aluminum under no gravitational forces, external forces and partial fixed boundaries. We fix only the lower boundary of the block and apply a uniform normal force on the upper boundary. This means that the boundary conditions at the lower boundary is given by

$$\boldsymbol{u} = 0 \qquad \text{on } \Gamma_1,$$

on the upper boundary by

$$\boldsymbol{\sigma} \cdot \boldsymbol{n} = \begin{bmatrix} 0 \\ -10 \times 10^9 \end{bmatrix} \qquad \text{on } \Gamma_2,$$

and on all other boundaries by

$$\boldsymbol{\sigma} \cdot \boldsymbol{n} = 0 \qquad \text{on } \Gamma_3.$$

The block we will investigate has width, height and depth equal to 1 meter.

The values for all parameters used in the simulation can be found in Table 5.22. We will use a grid with 21 nodes in both the x_1-, x_2- and the x_3-direction. The results of the simulation can be found in Figures 5.35 and 5.36. The results show that all fixed boundaries remain fixed and all other boundaries show deformations. The deformation of the upper boundary is also visible throughout the entire interior of the plate.

Parameter	Value
E	70×10^9
ν	0.33
ρ_m	2700
b_1	0
b_2	0
b_3	0

Table 5.22: Parameter values used during simulation.

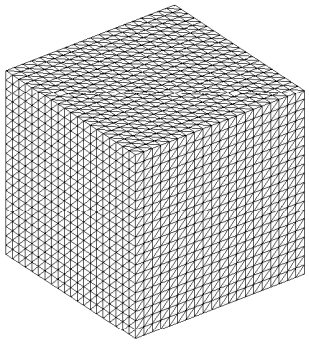

(a) Finite element mesh before deformation.

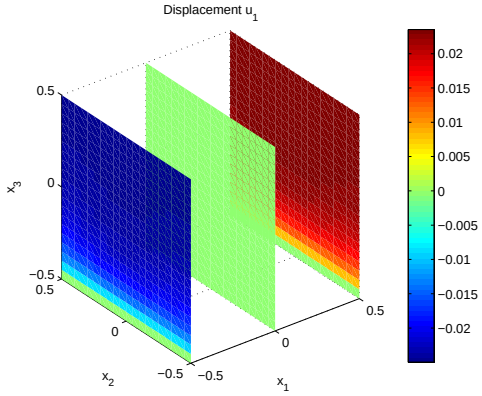

(b) Displacement u_1.

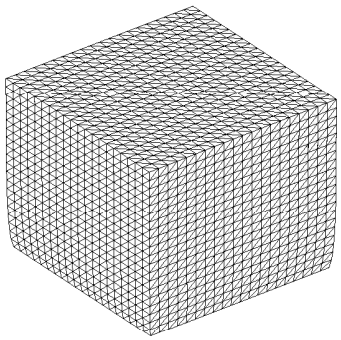

(c) Finite element mesh after deformation

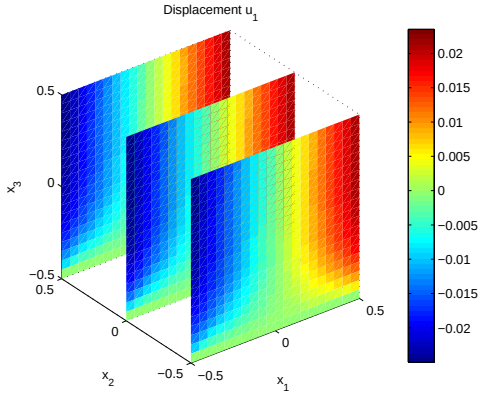

(d) Displacement u_1.

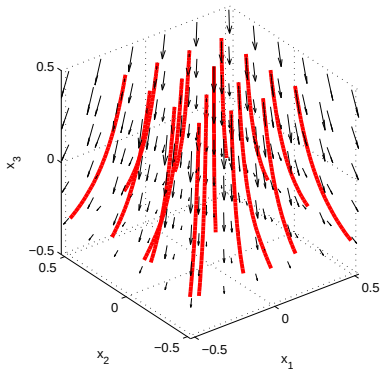

(e) Displacement vector field.

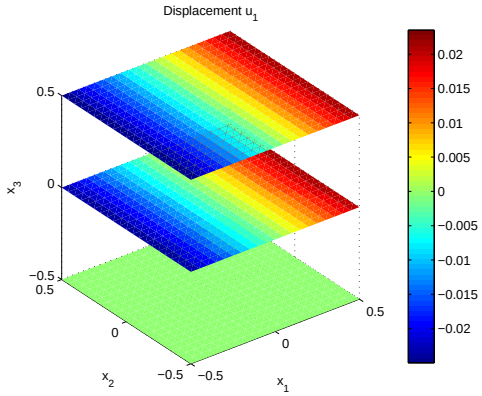

(f) Displacement u_1.

Figure 5.35: Results for uniform normal force model 2.

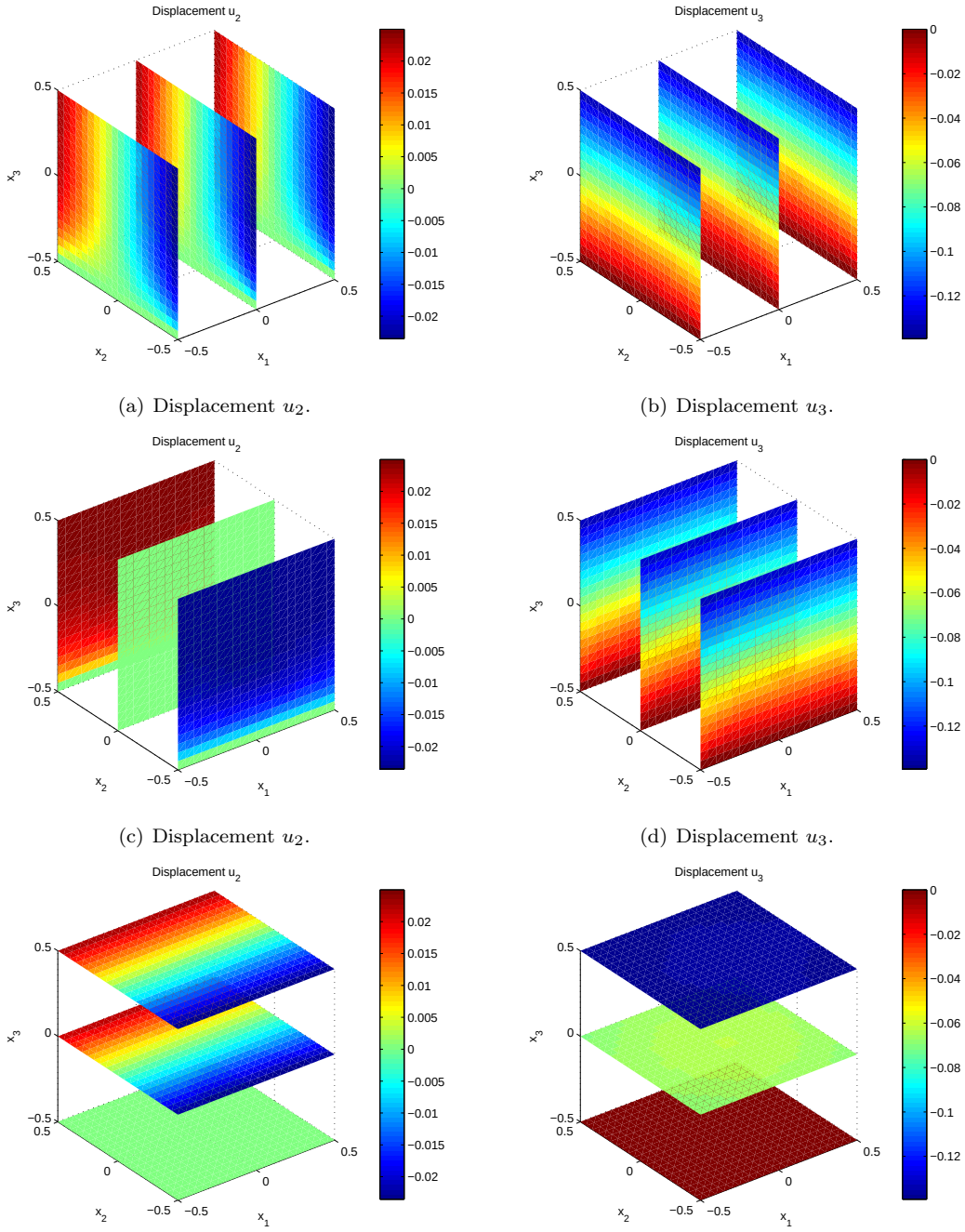

(a) Displacement u_2.

(b) Displacement u_3.

(c) Displacement u_2.

(d) Displacement u_3.

(e) Displacement u_2.

(f) Displacement u_3.

Figure 5.36: Results for uniform normal force model 2.

5.3.4 Normal point force model 1

The simulation performed in this section describe the steady state behavior of a block of aluminum under no gravitational forces, external forces and partial fixed boundaries. We fix all boundaries except the upper boundary of the block and apply a normal point force on the upper boundary at the location $x_1 = x_2 = 0$. This means that the boundary conditions at the upper boundary at $x_1 = x_2 = 0$ is given by

$$\boldsymbol{\sigma} \cdot \boldsymbol{n} = \begin{bmatrix} 0 \\ -10 \times 10^9 \end{bmatrix} \qquad \text{on } \Gamma_1,$$

on the remainder of the upper boundary by

$$\boldsymbol{\sigma} \cdot \boldsymbol{n} = 0 \qquad \text{on } \Gamma_2,$$

and on all other boundaries by

$$\boldsymbol{u} = 0 \qquad \text{on } \Gamma_3.$$

The block we will investigate has width, height and depth equal to 1 meter.

The values for all parameters used in the simulation can be found in Table 5.23. We will use a grid with 21 nodes in both the x_1-, x_2- and the x_3-direction. The results of the simulation can be found in Figures 5.37 and 5.38. The results show that all fixed boundaries remain fixed and all other boundaries show deformations. The deformation of the upper boundary is also visible throughout the entire interior of the plate.

Parameter	Value
E	70×10^9
ν	0.33
ρ_m	2700
b_1	0
b_2	0
b_3	0

Table 5.23: Parameter values used during simulation.

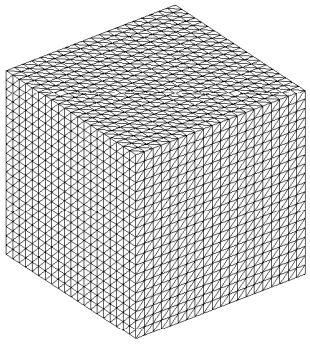

(a) Finite element mesh before deformation.

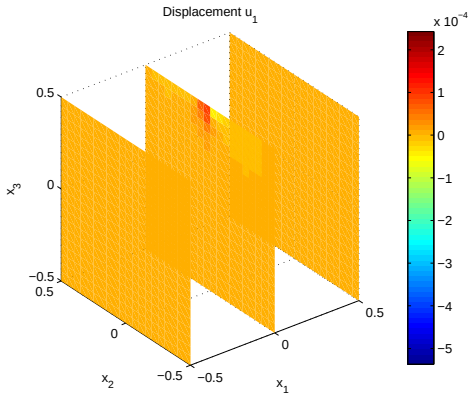

(b) Displacement u_1.

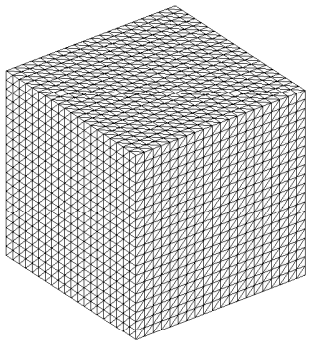

(c) Finite element mesh after deformation

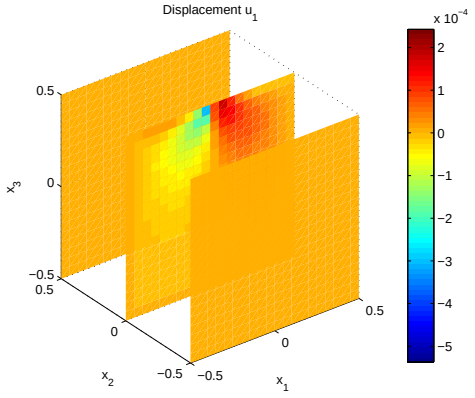

(d) Displacement u_1.

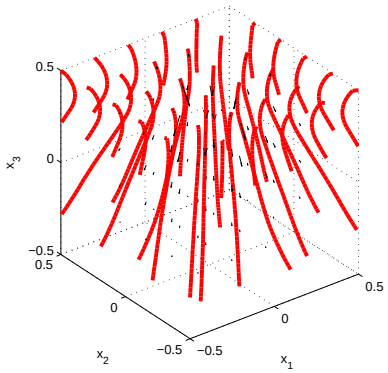

(e) Displacement vector field.

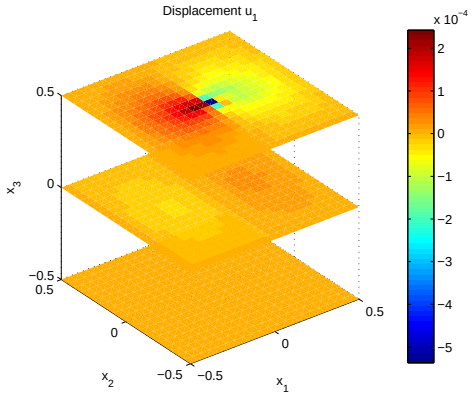

(f) Displacement u_1.

Figure 5.37: Results for normal point force model 1.

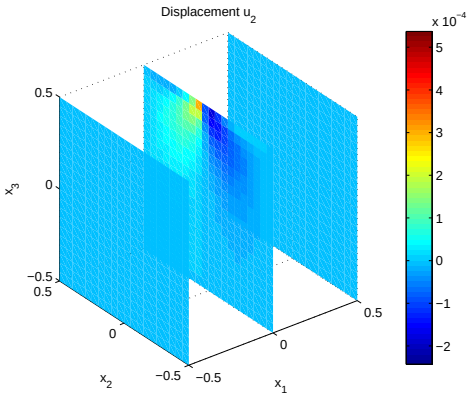

(a) Displacement u_2.

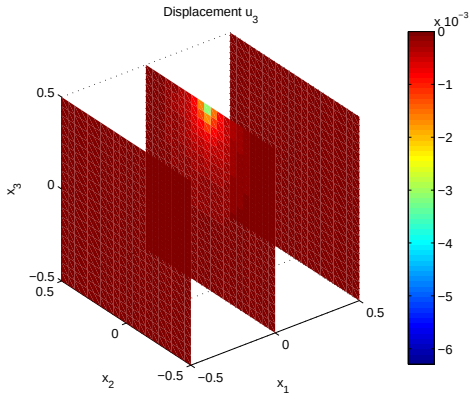

(b) Displacement u_3.

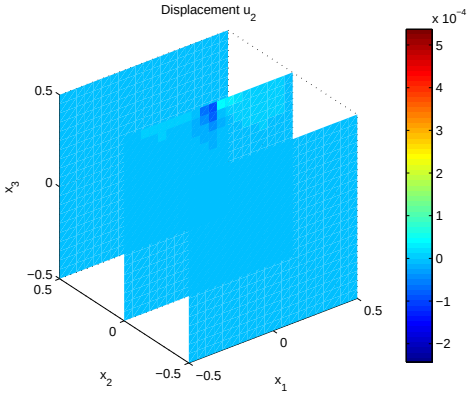

(c) Displacement u_2.

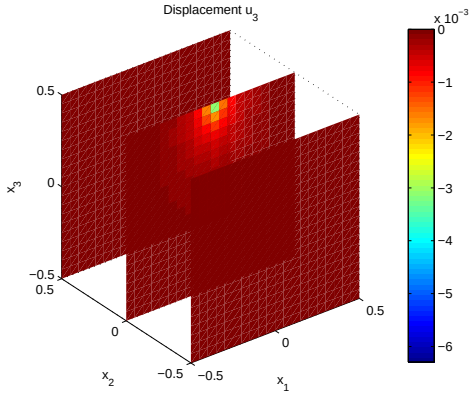

(d) Displacement u_3.

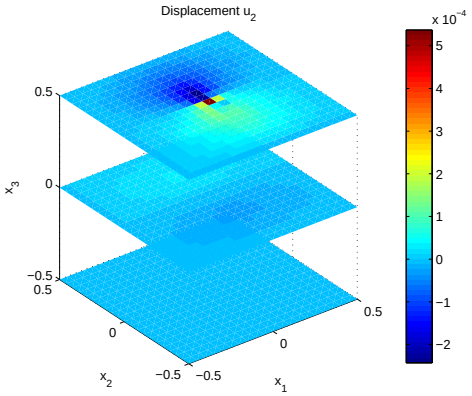

(e) Displacement u_2.

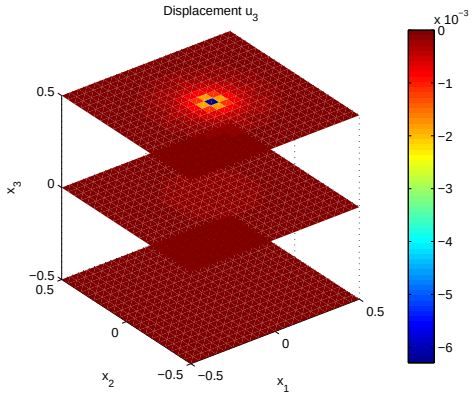

(f) Displacement u_3.

Figure 5.38: Results for normal point force model 1.

5.3.5 Normal point force model 2

The simulation performed in this section describe the steady state behavior of a block of aluminum under no gravitational forces, external forces and partial fixed boundaries. We fix only the lower boundary and apply a normal point force on the upper boundary at the location $x_1 = x_2 = 0$. This means that the boundary conditions at the upper boundary at $x_1 = x_2 = 0$ is given by

$$\boldsymbol{\sigma} \cdot \boldsymbol{n} = \begin{bmatrix} 0 \\ -10 \times 10^9 \end{bmatrix} \qquad \text{on } \Gamma_1,$$

on the remainder of the upper boundary by

$$\boldsymbol{\sigma} \cdot \boldsymbol{n} = 0 \qquad \text{on } \Gamma_2,$$

on the lower boundary by

$$\boldsymbol{u} = 0 \qquad \text{on } \Gamma_3,$$

and on all other boundaries by

$$\boldsymbol{\sigma} \cdot \boldsymbol{n} = 0 \qquad \text{on } \Gamma_4.$$

The block we will investigate has width, height and depth equal to 1 meter.

The values for all parameters used in the simulation can be found in Table 5.24. We will use a grid with 21 nodes in both the x_1-, x_2- and the x_3-direction. The results of the simulation can be found in Figures 5.39 and 5.40. The results show that all fixed boundaries remain fixed and all other boundaries show deformations. The deformation of the upper boundary is also visible throughout the entire interior of the plate.

Parameter	Value
E	70×10^9
ν	0.33
ρ_m	2700
b_1	0
b_2	0
b_3	0

Table 5.24: Parameter values used during simulation.

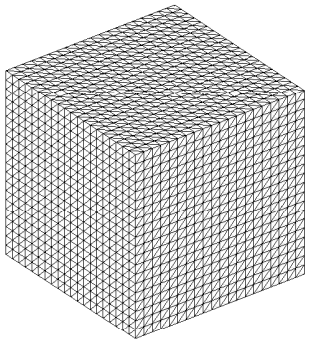

(a) Finite element mesh before deformation.

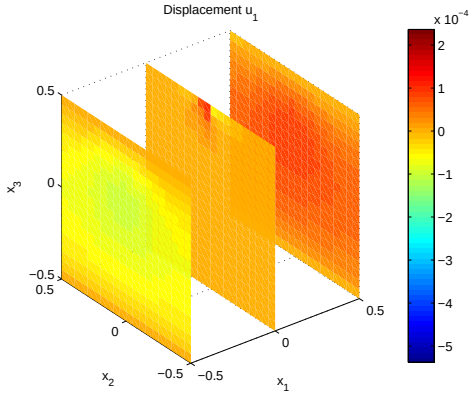

(b) Displacement u_1.

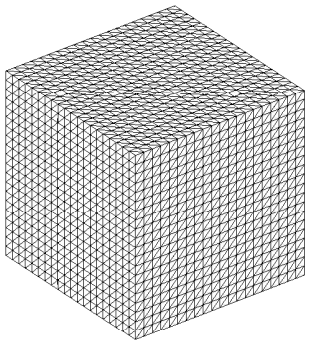

(c) Finite element mesh after deformation

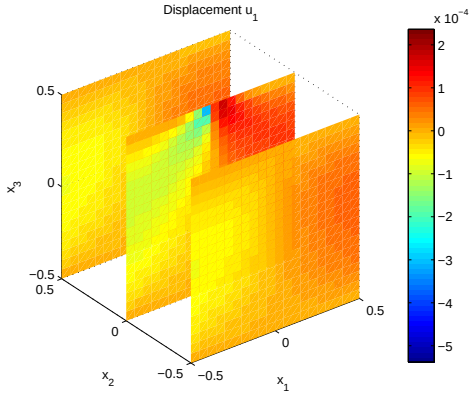

(d) Displacement u_1.

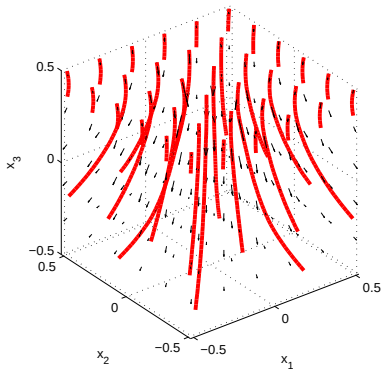

(e) Displacement vector field.

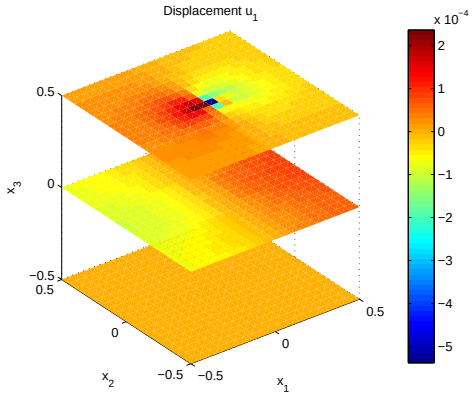

(f) Displacement u_1.

Figure 5.39: Results for normal point force model 2.

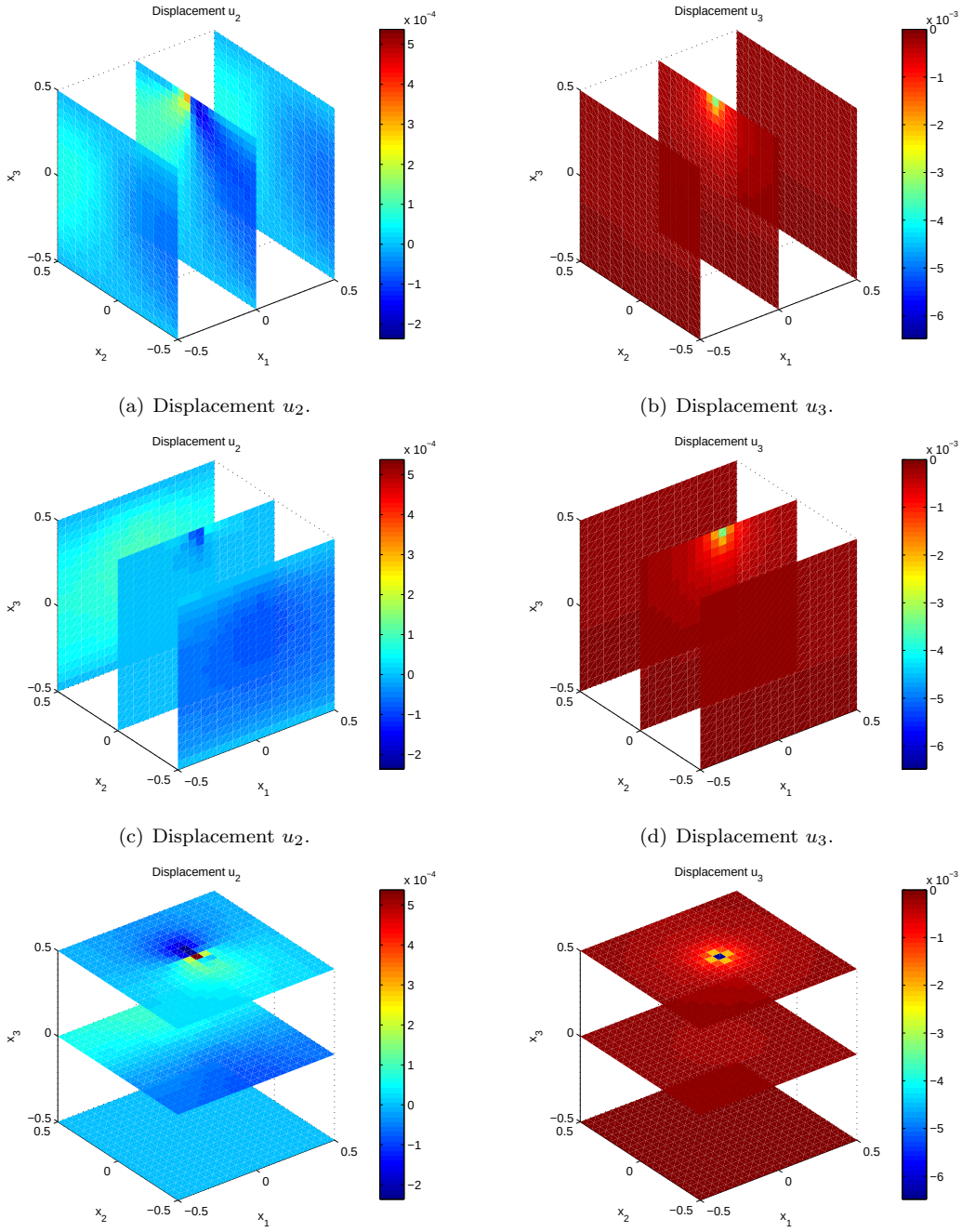

(a) Displacement u_2.

(b) Displacement u_3.

(c) Displacement u_2.

(d) Displacement u_3.

(e) Displacement u_2.

(f) Displacement u_3.

Figure 5.40: Results for normal point force model 2.

5.3.6 Remarks

Although the results from the above simulations seem to be physically correct, it must be noted that the chosen mesh for both the two dimensional and three dimensional model could have one downside. This downside is that both meshes use a single base for construction of the mesh, which uses a the same orientation for the edges of the triangles and tetrahedron. This could has as effect that in certain cases the displacements in some directions could be ignored or miscalculated.

To resolve this situation for the two dimensional model, a mesh can be used based on squares with alternating diagonals. One option for this solution is to say that the after numbering the squares from left to right and then from bottom to top any odd square has a diagonal that runs from the top right to the bottom left and any even block has a diagonal that runs from the bottom right to the top left.

To resolve this situation for the three dimensional model, a mesh can be used based on cubes with alternating tetrahedral divisions. One option for this solution is to say that the after numbering the squares from left to right, then from front to back and finally from bottom to top any odd cube has an odd decomposition and any even block has even decomposition. For the odd and even decomposition one can use a decomposition of a cube into five tetrahedron with the topology as in Figure 5.41.

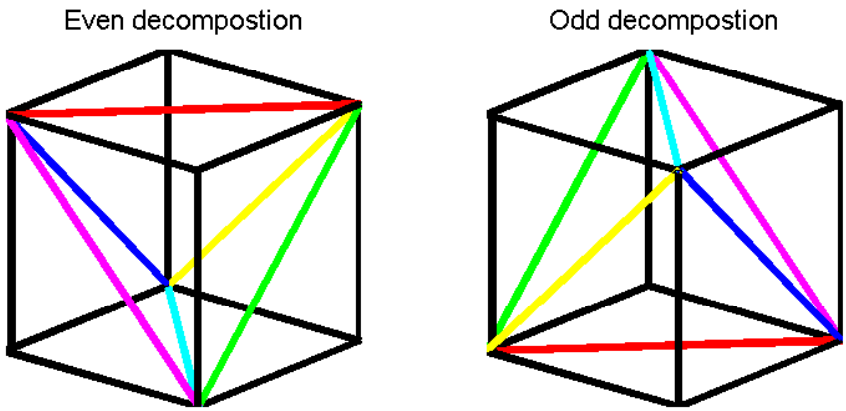

Figure 5.41: Topology for odd-even decomposition for three dimensional mesh.

Chapter 6

Concluding remarks and future work

6.1 Conclusions

In this document we have derived a model for the nucleation and growth of particles and numerically simulated this model. From the results we can conclude that the model correctly predicts the number of particles in a block aluminum alloy. We have also obtained that the time integration method used in [7] can be improved from first order to second order time accuracy by using the θ-method with $\theta = 1/2$ or by use of one of the two discussed DIRK-methods. Both DIRK-methods require significantly more computations than the θ-method, so that we recommend to use the θ-method with $\theta = 1/2$ to obtain the particle distribution as a function of time.

The results from simulation with the derived elastic deformation model show that the model is correct for small deformations and small external forces. The influence of gravitational body forces causes small deformations, but these do not influence the overall structure of the metal. We therefore recommend to neglect the gravitational body forces when the object under investigation has a size of a micrometer or larger.

6.2 Future work

Although a model for elastic deformation of aluminum objects has been formulated, this model will have no use in practice, since our domain of interest is in the influence of inelastic deformations within a aluminum object. We will therefore investigate in part of the remainder of this Master thesis project the derivation and simulation of a model for elastic-plastic deformations within a object.

Besides the model for elastic deformations a model has been propose and validated for particle nucleation and growth in aluminum alloys. The influence of metalworking on the derived particle size distributions is of interest to us as this has not been modeled yet. To this end we will investigate the coupling between a model for (in)elastic deformations and particle nucleation and growth in aluminum alloys and if obtained simulate this coupled model. After some preliminary research it seems likely that the strain energy present in a system can be of influence to the particle distribution.

If the two goals above have been obtained before the end of this Master thesis, it maybe possible to extend the model for particle nucleation and growth to ternary, quaternary or more complex alloys and again to couple this with the model for inelastic deformations.

Taking these considerations into account, the steps we will perform are the following:

1. Couple the elastic model and the nucleation model in one dimension;
2. Derive the elastic-plastic model in one dimension;
3. Couple the elastic-plastic model and the nucleation model in one dimension;
4. Couple the elastic model and the nucleation model in two and three dimensions;

5. Derive the elastic-plastic model in two and three dimensions;
6. Couple the elastic-plastic model and the nucleation model in two and three dimensions;
7. Extend the nucleation model to ternary and complexer alloys.

From the steps stated above the goal of the Master thesis project is to at least complete steps 1 to 3 and preferable to have achieved parts of steps 4 to 6.

Bibliography

[1] CFD-Online. (2005). Tridiagonal matrix algorithm - TDMA (Thomas algorithm). Available: http://www.cfd-online.com/Wiki/Tridiagonal_matrix_algorithm_-_TDMA_(Thomas_algorithm). Last accessed 7 March 2009.

[2] Crouzeix, M. (1975). Sur l'approximation des é quations différentielles opérationelles par des méthodes de Runge-Kutta. Paris: University Paris VI.

[3] Crouzeix, M. & Raviart, P.A. (1980). Approximation des Problèmes d'Evolution. Rennes: University de Rennes.

[4] Hundsdorfer, W. & Verwer, J.G. (2003). Numerical Solution of Time-Dependent Advection-Diffusion-Reaction Equations. Heidelberg: Springer-Verlag.

[5] Kampmann, R., Eckerlebe, H. & Wagner, R.. (1987). Materials Research Society Symposium Proceedings. 57, p525.

[6] Langer, J.S. & Schwartz, A.J.. (1980). Kinetics of nucleation in near-critical fluids. Physical Review A. 21 (3), p948-958.

[7] Myhr, O.R. & Grong, Ø.. (2000). Modelling of non-isothermal transformations in alloys containing a particle distribution. Acta Materialia. 48 (7), p1605-1615.

[8] Nørsett, S.P.. (1974). Semi-explicit Runge-Kutta methods. In: Report Mathematics and Compuations. Trondheim: University of Trondheim. No 6/74.

[9] Porter, D.A. & Easterling, K.E. (1981). Phase Transformations in Metals and Alloys. London: Chapman & Hall.

[10] Seagrave, S. & Canty, T.. (1999). Part I Crystallography Tutorial - Diffusion. Available: http://www.soton.ac.uk/∼engmats/xtal/diffusion/index.html. Last accessed 5 March 2009.

[11] Wagner, R. & Kampmann, R. (1991). Materials Science and Technology - A Comprehensive Treatment, Vol. 5. Weinheim: VCH. p21.

[12] Wikipedia. (2002). Phase diagram. Available: http://en.wikipedia.org/wiki/Phase_diagram. Last accessed 5 March 2009.

[13] Wikipedia. (2005). Rolling (metalworking). Available: http://en.wikipedia.org/wiki/Rolling_(metalworking). Last accessed 26 March 2009.

[14] Wikipedia. (2004). Extrusion. Available: http://en.wikipedia.org/wiki/Extrusion. Last accessed 26 March 2009.

[15] Wikipedia. (2003). Tensile strength. Available: http://en.wikipedia.org/wiki/Tensile_strength. Last accessed 3 April 2009.

Nomenclature

α_i	Parameter in boundary condition for elasticity model
A_0	Parameter related to the energy barrier for nucleation (J/mol)
$\boldsymbol{b}$	Internal force vector per unit volume (N/m^3)
$\bar{C}$	Mean solute concentration in the system (wt%)
C_0	Overall solute concentration in the system (wt%)
C_e	Equilibrium solute concentration at the particle/matrix interface (wt%)
C_i	Solute concentration at the particle/matrix interface (wt%)
C_p	Solute concentration inside the particle (wt%)
C_s	Pre-exponential term for C_e (wt%)
D	Diffusion Coefficient (m^2/s)
D_0	Pre-exponential term for D (m^2/s)
δ_{ij}	Kronecker delta
Δr	Length of control volumes (m)
Δr^*	Factor used in production term (m)
Δt	Time increment (s)
E	Elasticity modulus (N/m^2)
e_{ij}	Strain component i, j
f	Particle volume fraction
$\boldsymbol{f}$	External force on a boundary
ϕ	Particle size distribution function ($\#/m^4$)
Γ_i	Boundary of ith control volume
j	Nucleation rate ($\#/m^3 s$)
j_0	Numerical constant in the expression for j ($\#/m^3 s$)
λ	Bulk modulus (N/m^2)
M	Number of control volumes
μ	Shear modulus (N/m^2)
n	Total number concentration of particles in the system ($\#/m^3$)
$\boldsymbol{n}$	Normal vector on a boundary
N	Particles concentration ($\#/m^3$)
N_0	Initial particle concentration ($\#/m^3$)
N_i	Value of N at r_i ($\#/m^3$)
ν	Poisson ratio

Ω_i	ith control volume
Q_d	Activation energy for diffusion (J/mol)
Q_s	Apparent solvus boundary enthalpy (J/mol)
r	Particle radius (m)
$\bar{r}$	Mean particle radius of the system (m)
r^*	Critical particle radius (m)
R	Universal gas constant (8.314 J/Kmol)
ρ	Standard deviation of radii of the system (m)
ρ_m	Density (kg/m^3)
r_i	Midpoint of ith control volume (m)
$r_{\max}$	Maximum numerical radius (m)
$r_{\min}$	Minimum numerical radius (m)
S	Source term ($\#/m^3 s$)
σ	Particle-matrix interface energy (J/m^2)
σ_{ij}	Normal stress in direction i acting on plane j =constant (N/m^2)
t	Time (s)
T	Temperature (K)
θ	Parameter for time-integration method
u_i	Displacement in i-th coordinate (m)
u_{bi}	Boundary value for u_i (m)
v	Growth rate of particles (m/s)
V_m	Molar volume of precipitates (m^3/mol)
x_i	i-th coordinate (m)